
Electronic Thesis and Dissertation Repository

1-21-2021 12:30 PM

Non-invasive quantification of cerebral oxygen metabolism by hybrid positron emission tomography/magnetic resonance imaging

Lucas Diovani Lopes Narciso, *The University of Western Ontario*

Supervisor: St Lawrence, Keith, *The University of Western Ontario*

A thesis submitted in partial fulfillment of the requirements for the Doctor of Philosophy degree in Medical Biophysics

© Lucas Diovani Lopes Narciso 2021

Follow this and additional works at: <https://ir.lib.uwo.ca/etd>



Part of the [Biophysics Commons](#)

Recommended Citation

Narciso, Lucas Diovani Lopes, "Non-invasive quantification of cerebral oxygen metabolism by hybrid positron emission tomography/magnetic resonance imaging" (2021). *Electronic Thesis and Dissertation Repository*. 8361.

<https://ir.lib.uwo.ca/etd/8361>

This Dissertation/Thesis is brought to you for free and open access by Scholarship@Western. It has been accepted for inclusion in Electronic Thesis and Dissertation Repository by an authorized administrator of Scholarship@Western. For more information, please contact wlsadmin@uwo.ca.

Abstract

Although positron emission tomography (PET) remains the gold standard for quantifying cerebral blood flow (CBF) and cerebral metabolic rate of oxygen (CMRO₂), the procedures are invasive and complex, requiring arterial sampling and accounting for blood-borne activity. Non-invasive methods generally require extracting an image-derived input function (IDIF) from the carotid arteries; however, these methods are sensitive to partial volume errors due to the poor spatial resolution of PET. Hybrid PET/magnetic resonance imaging (MRI) offers an alternative non-invasive approach by using MRI to calibrate PET data. PET/MR imaging of oxidative metabolism (PMRO_x) is a reference-based approach that uses whole-brain (WB) measurements of oxygen extraction fraction and CBF to calibrate [¹⁵O]O₂-PET data. Similarly, PET/MR imaging of CBF (PMRFlow) requires only WB CBF to calibrate dynamic [¹⁵O]H₂O-PET data. Both methods avoid the need for invasive arterial sampling while maintaining the ability to quantify CBF and CMRO₂.

This thesis contains the theoretical framework of PMRO_x, along with error analyses and an assessment on PET data acquired from healthy participants ($n = 10$), followed by its validation in an animal model by comparison to PET-alone measurements ($n = 8$). Additionally, the MRI-perfusion technique arterial spin labeling was used to further simplify PMRO_x by replacing [¹⁵O]H₂O-PET, and PMRO_x was demonstrated to be sensitive to anesthetics-induced changes in metabolism. The accuracy of a PMRFlow approach of obtaining the IDIF (PMRFlow_{IDIF}) from the WB [¹⁵O]H₂O time-activity curve (TAC) was assessed in a porcine model by comparison to PET-only CBF measurements ($n = 12$). The ability of the method to remove blood-borne signal was demonstrated by generating CBF images for healthy individuals ($n = 13$).

In summary, results demonstrated the feasibility of producing quantitative CBF and CMRO₂ images by PET/MRI without the need for invasive blood sampling. PMRO_x circumvents many of the complexities of traditional PET CMRO₂ imaging and has the potential to reduce PET imaging to [¹⁵O]O₂ only. PMRFlow_{IDIF} is an easy-to-implement method that benefits from the high signal-to-noise ratio of the WB TAC and does not require vessel segmentation. Future studies involving human participants are required to fully validate these

approaches, both in the healthy brain and in disorders characterized by disruptions in cerebral hemodynamics and metabolism.

Keywords

[¹⁵O]H₂O, [¹⁵O]O₂, Cerebral Blood Flow (CBF), Cerebral Blood Volume (CBV), Cerebral Metabolic Rate of Oxygen (CMRO₂), Oxygen Extraction Fraction (OEF), Image-Derived Input Function (IDIF), Magnetic Resonance Imaging (MRI), Positron Emission Tomography (PET), Hybrid PET/MRI, Non-Invasive PET, Arterial Spin Labeling (ASL), Phase-Contrast (PC) MRI

Summary for lay audience

The brain is a complex organ that requires constant supply of blood and oxygen. As a consequence, tissue damage can occur within minutes to hours when supply of oxygen is interrupted. Measurements of cerebral blood flow and oxygen consumption with medical imaging modalities play an important role in assessing diseases such as carotid artery stenosis, as well as in understanding a variety of disorders, such as diabetes, drug addiction, and cancer. Over the years, research has also focused on answering questions regarding its role in neurodegenerative diseases, such as Alzheimer's and Parkinson's disease.

Imaging blood flow and oxygen consumption in the human brain is challenging. The gold standard is an imaging modality known as PET; however, the procedure is complex, invasive, and not readily accessible. One alternative is an emerging imaging technology that incorporates PET and MRI into a single hybrid scanner that can simplify the procedure. The aim of this thesis is to present non-invasive and fast alternatives to the PET procedure by using MRI measurements as reference. Here, the theory behind the proposed approaches is presented, together with their validation in an animal model.

In summary, results demonstrate the possibility of imaging cerebral blood flow and oxygen use by PET/MRI. When used in research studies, these approaches have the potential to help us better understand the role of interruptions in energy delivery and production in cerebral disorders. They can also help researchers develop more accessible imaging tools.

Co-authorship statement

This thesis includes co-authored papers in chapters 2 to 4, for which the contribution to such work and the nature and extent of this contribution are described here. The second chapter presents the work previously published in *Physics in Medicine and Biology* on 04 March 2021 (66 065009) and is entitled “A non-invasive reference-based method for imaging the cerebral metabolic rate of oxygen by PET/MR: theory and error analysis” (© IOP Publishing. Reproduced with permission. All rights reserved.) For this work, Lucas Narciso (LN) drafted the article and was responsible for the theory and analyses described in this paper. Tracy Ssali (TS) contributed with MATLAB scripts for the simulations, and data preprocessing and analysis. Hidehiro Iida (HI) provided the human PET datasets and made substantial contributions to the theory and study design. TS, HI and Keith St Lawrence (KStL) revised the manuscript critically for important intellectual content. KStL helped develop the theory and approved the final version to be published.

Chapter 3 has been adapted from the work published in *The Journal of Nuclear Medicine* on 19 March 2021 (jnmed.120.260521) and is entitled “A non-invasive method for quantifying the cerebral metabolic rate of oxygen by hybrid PET/MRI: validation in a porcine model.” LN drafted the article and was responsible for the experiments and analyses described within. TS developed the fitting scripts used to generate the $[^{15}\text{O}]\text{H}_2\text{O}$ images and helped optimize the arterial spin labeling sequence parameters. Linshan Liu (LL) helped with the experiments and was responsible for the arterial sampling system. Heather Biernaski and John Butler were the PET/MR technologists responsible for running the PET/MRI procedures. Laura Morrison and Jennifer Hadway were the animal technicians. Jeffrey Corsaut and Justin W. Hicks (JWH) were responsible for $[^{15}\text{O}]\text{H}_2\text{O}$ and $[^{15}\text{O}]\text{O}_2$ production and delivery. Michael C. Langham and Felix W. Wehrli developed the OxFlow sequence and helped translate it to the Siemens Biograph mMR PET/MR system. HI made substantial contributions to the experimental design. All co-authors revised the manuscript critically for important intellectual content. KStL helped develop the experimental design and approved the final version to be published.

Lastly, Chapter 4 has been adapted from the paper entitled “Non-invasive quantification of cerebral blood flow using PET/MRI to extract the $[^{15}\text{O}]\text{H}_2\text{O}$ image-derived input function free of partial volume errors,” currently under review in the *Journal of Magnetic*

Resonance Imaging [manuscript ID: JMRI-21-1596]. LN drafted the article and was responsible for the experiments and data analysis. TS contributed to conceptualization, methodology, and data acquisition. LL contributed to data acquisition. Sarah Jesso contributed to patient recruitment. JWH was responsible for [^{15}O]H₂O production and delivery. UA contributed to the methodology. Elizabeth Finger and KStL contributed to funding acquisition, project administration, and study design. KStL contributed to conceptualization, methodology, and drafting of the article. All co-authors critically reviewed the manuscript.

Acknowledgements

“When we see the Earth from space, we see ourselves as a whole. We see the unity and not the divisions. It is such a simple image with a compelling message; one planet, one human race.”

Stephen W. Hawking

The work contained in this thesis could only be possible due to a collective effort from several people, whom I wish to acknowledge here.

First, I would like to thank Professor Keith St Lawrence for his support during my doctoral studies. Your invaluable supervision throughout my journey was crucial to get here. Thank you for all the feedback you have provided during these four years. Thank you for all the time you spent steering my thoughts in the right direction. Your patience, motivation and immense knowledge helped in shaping the scientist I have become, and for that I am grateful.

I also wish to thank my advisory committee members, Professors Jonathan Thiessen and Udunna Anazodo, for pointing in the right direction every time I needed guidance, both academically and professionally.

I am grateful to my lab members. Linshan Liu, thank you for your friendship and your help in technical matters. Tracy Ssali, your friendship helped make Canada my home away from home; thank you for your patience, guidance, and all the support during these years. Praveen Dassanayake, thank you for your company and for all the time we vented our frustrations. I will miss the water walks and the long conversations.

I am grateful to Heather Biernaski and John Butler for their support during data collection; to Jennifer Hadway, Laura Morrison and Lise Desjardins for their assistance with the animal experiments; to Jeffrey Corsaut and Justin Hicks for turning perfectly drinkable water and breathable oxygen into radioactive substances.

I would like to acknowledge all the collaborators and friends both from Lawson Health Research Institute and Western University for their contributions, incredible times, and shared suffering through grad school.

I would like to thank all my friends for supporting me during all these years. Here, I list a very special group of friends that have been by my side in the best and worse of times. Friends who were there when I needed to cry, who celebrated (and drank) with me, and scolded me when I needed to learn. Thank you Jislaine, Eduardo, Allan, Samara, Aldrio, Caroline, Phelipi, Gabriel, Jordan, and Ashley. I love you all! ❤️

Por fim, eu sou extremamente grato pelos meus pais, Fátima e João, e irmãos, Artur, Maicon e Júnior, pelo suporte virtual do hemisfério sul do planeta Terra. Muito obrigado, mãe, pelo seu amor incondicional, pelas longas chamadas quando eu estava me sentindo triste, e por todo o tempo que você ouviu minhas reclamações. Muito obrigado, pai, pelo apoio durante todos esses anos, mesmo com a distância entre nós. Muito obrigado, meus irmãos, por apoiarem minha decisão egoísta de desbravar o mundo e procurar por melhores oportunidades de vida. Amo vocês!

I would like to dedicate this thesis to everyone who supported me throughout my journey.

Table of contents

Abstract.....	i
Summary for lay audience	iii
Co-authorship statement	iv
Acknowledgements.....	vi
Table of contents.....	viii
List of tables.....	xii
List of figures	xiii
List of appendices	xv
List of abbreviations	xvi
List of variables.....	xix
Chapter 1	1
1 Introduction.....	1
1.1 Cerebral hemodynamics and metabolism.....	1
1.2 Clinical relevance	2
1.3 Quantification of cerebral hemodynamics and metabolism	5
1.4 Positron emission tomography	7
1.4.1 Cerebral blood flow	8
1.4.2 Oxygen extraction fraction	10
1.4.3 Cerebral metabolic rate of oxygen.....	12
1.5 Magnetic resonance imaging.....	14
1.5.1 Cerebral blood flow	14
1.5.2 Cerebral metabolism.....	17
1.6 Advantages of imaging cerebral metabolism with hybrid PET/MR	22
1.7 Thesis outline	24

1.7.1	Chapter 2: A non-invasive reference-based method for imaging the cerebral metabolic rate of oxygen by PET/MR: theory and error analysis	24
1.7.2	Chapter 3: A non-invasive method for quantifying cerebral metabolic rate of oxygen by hybrid PET/MRI: validation in a porcine model	24
1.7.3	Chapter 4: Quantifying cerebral blood flow by a non-invasive PET/MR method of extracting the [¹⁵ O]H ₂ O image-derived input function free of partial volume errors.....	25
1.7.4	Conclusion and future work	25
	Chapter 2.....	26
2	A non-invasive reference-based method for imaging the cerebral metabolic rate of oxygen by PET/MR: theory and error analysis	26
2.1	Introduction	26
2.2	Theory	28
2.2.1	Simplified reference-based approach	29
2.2.2	Residual functions	30
2.3	Materials and methods.....	31
2.3.1	Simulations.....	31
2.3.2	Application of the reference-based approach to [¹⁵ O]-PET data.....	34
2.4	Results	35
2.5	Discussion	42
2.6	Conclusions	45
	Chapter 3.....	46
3	A non-invasive method for quantifying cerebral metabolic rate of oxygen by hybrid PET/MRI: validation in a porcine model.....	46
3.1	Introduction	46
3.2	Materials and methods.....	47
3.2.1	Study protocol	47
3.2.2	PET imaging and postprocessing	48
3.2.3	MR imaging and postprocessing	49

3.2.4	PET-only imaging: DBFM.....	50
3.2.5	PMRO _x	51
3.2.6	Regional CBF, OEF and CMRO ₂ measurements.....	52
3.2.7	Statistics.....	52
3.3	Results.....	52
3.3.1	Validation.....	54
3.3.2	PMRO _{xASL}	56
3.3.3	Lower metabolic condition.....	56
3.4	Discussion.....	57
3.5	Conclusion.....	59
Chapter 4	60
4	Quantifying cerebral blood flow by a non-invasive PET/MR method of extracting the [¹⁵ O]H ₂ O image-derived input function free of partial volume errors.....	60
4.1	Introduction.....	60
4.2	Theory.....	61
4.2.1	PMRFlow _{IDIF}	61
4.2.2	PMRFlow _{DIM}	62
4.3	Materials and Methods.....	63
4.3.1	Simulations.....	63
4.3.2	Animal experiments.....	64
4.3.3	Human experiments.....	66
4.3.4	CBF estimates.....	68
4.3.5	Statistics.....	68
4.4	Results.....	69
4.4.1	Error analysis.....	69
4.4.2	Validation study.....	70

4.4.3	Assessment with human data.....	73
4.5	Discussion	75
4.6	Conclusion.....	78
Chapter 5	79
5	Conclusions and future work	79
5.1	Summary of findings	79
5.1.1	A non-invasive reference-based method for imaging the cerebral metabolic rate of oxygen by PET/MR: theory and error analysis.....	79
5.1.2	A non-invasive method for quantifying cerebral metabolic rate of oxygen by hybrid PET/MRI: validation in a porcine model	80
5.1.3	Quantifying cerebral blood flow by a non-invasive PET/MR method of extracting the [¹⁵ O]H ₂ O image-derived input function free of partial volume errors	80
5.2	Relevance of findings.....	81
5.3	Future work	82
5.3.1	PMRO _{XIDIF}	82
5.3.2	Tracking absolute CMRO ₂ changes during neuronal activation	85
5.3.3	Non-invasive quantification of aerobic glycolysis	86
References	88
Appendices	105
Curriculum vitae	106

List of tables

Table 1.1. Reproducibility of [^{15}O]-PET measurements.	13
Table 3.1. Summary of arterial blood measurements.	53
Table 3.2. Summary of the regression and correlation analyses.....	54
Table 4.1. Summary results from validation study.	72
Table 4.2. Summary results from assessment with human data.	73

List of figures

Figure 1.1. Cerebral autoregulation.	2
Figure 1.2. CBV, CBF, OEF and CMRO ₂ in stage 2 hemodynamic failure.	3
Figure 1.3. Cerebral metabolism in pediatric patient with Moyamoya disease.....	4
Figure 1.4. Increased OEF in patients with carotid artery occlusion.....	4
Figure 1.5. Aerobic glycolysis reduction in normal aging.....	5
Figure 1.6. One-tissue compartment model for [¹⁵ O]H ₂ O.....	9
Figure 1.7. Typical CBF maps obtained with [¹⁵ O]H ₂ O PET.	9
Figure 1.8. One-tissue compartment model for [¹⁵ O]O ₂	11
Figure 1.9. Typical OEF maps obtained with [¹⁵ O]O ₂ PET.	11
Figure 1.10. Typical CBV maps obtained with [¹⁵ O]CO PET.	12
Figure 1.11. Typical CMRO ₂ maps obtained with [¹⁵ O]O ₂ PET.....	13
Figure 1.12. PC-MRI scheme.	15
Figure 1.13. ASL acquisition scheme.....	16
Figure 1.14. Typical CBF maps obtained with pseudo-continuous ASL.	17
Figure 1.15. SBO steps to obtain global venous oxygen saturation.	20
Figure 1.16. Resulting regional maps obtained with qBOLD.	21
Figure 1.17. CMRO ₂ map obtained with dual-calibrated fMRI.	22
Figure 2.1. Theoretical input functions and tissue TACs.	32
Figure 2.2. Simulations results: error in CMRO ₂ for neglecting RW and CBV.....	36
Figure 2.3. Simulations results: error in CMRO ₂ for changes in CBF.	37
Figure 2.4. Simulations results: error in CMRO ₂ due to inaccuracies in local CBF.	37
Figure 2.5. Simulations results: error in CMRO ₂ due to noise.	38
Figure 2.6. CMRO ₂ images obtained with the reference-based method.....	39
Figure 2.7. OEF images obtained with the reference-based method.	40
Figure 2.8. Comparison between reference-based and DARG methods.	41

Figure 3.1. Protocol diagram.	48
Figure 3.2. MR sequences acquisition and analysis scheme.	50
Figure 3.3. Measured versus population-based AIFs.....	53
Figure 3.4. PMRO _x validation results.	55
Figure 3.5. Group-wise CBF, OEF and CMRO ₂ images.....	55
Figure 3.6. PMRO _{xASL} results.	56
Figure 3.7. LMC results.....	57
Figure 4.1. Simulation results.	70
Figure 4.2. Comparison between AIFs and IDIFs and validation results.	71
Figure 4.3. Group-wise CBF and CBV _a images from validation study.....	72
Figure 4.4. Results from the assessment with human data.	74
Figure 4.5. Group-wise CBF and CBV _a images from human data.....	75
Figure 5.1. [¹⁵ O]O ₂ AIF and IDIF comparison.	84
Figure 5.2. Preliminary PMRO _{xIDIF} to PET-only comparison.	84
Figure 5.3. A representative IDIF extracted with the simultaneous estimation method.....	87
Figure 5.4. CMRGlc maps obtained with the variational Bayesian approach.....	87

List of appendices

Appendix A: Copyright Agreement Information.....	105
--	-----

List of abbreviations

^{11}C	Radioactive carbon isotope
^{15}O	Radioactive oxygen isotope
^{18}F	Radioactive fluorine isotope
$[^{11}\text{C}]\text{CO}$	$[^{11}\text{C}]$ -labelled carbon monoxide
$[^{18}\text{F}]\text{FDG}$	$[^{18}\text{F}]$ -labelled fluorodeoxyglucose
$[^{15}\text{O}]\text{CO}$	$[^{15}\text{O}]$ -labelled carbon monoxide
$[^{15}\text{O}]\text{CO}_2$	$[^{15}\text{O}]$ -labelled carbon dioxide
$[^{15}\text{O}]\text{H}_2\text{O}$	$[^{15}\text{O}]$ -labelled water
$[^{15}\text{O}]\text{O}_2$	$[^{15}\text{O}]$ -labelled oxygen
AIF	Arterial input function
AG	Aerobic glycolysis
ASL	Arterial spin labeling
AUC	Area under the curve
BOLD	Blood-oxygen level-dependent
C_aO_2	Arterial content of oxygen
CBF	Cerebral blood flow
CBV	Cerebral blood volume
CBV_a	Arterial CBV
CMRGlc	Cerebral metabolic rate of glucose
CMRO_2	Cerebral metabolic rate of oxygen
CO	Chemical formula of carbon monoxide
CO_2	Chemical formula of carbon dioxide
COV	Coefficient of variation
CPP	Cerebral perfusion pressure
CT	Computed tomography
DARG	Dual tracer autoradiographic method
DBFM	Dual-basis function method
DIM	Double integration method
DSC	Dynamic susceptibility contrast

FA	Flip angle
fMRI	Functional MRI
FoV	Field-of-view
FWHM	Full width at half-maximum
GM	Gray matter
H ₂ O	Chemical formula of water
Hb	Hemoglobin concentration
ICC	Intraclass correlation coefficient
IDIF	Image-derived input function
LD	Labeling duration
LMC	Lower metabolic condition
M ₀	Proton density-weighted image
MATLAB	Matrix Laboratory
MNI	Montreal Neurological Institute
MPRAGE	Magnetization prepared rapid acquisition gradient-echo sequence
MR	Magnetic resonance
MRI	MR imaging
N ₂ O	Chemical formula of nitrous oxide
O ₂	Chemical formula of oxygen
OEF	Oxygen extraction fraction
OGI	Oxygen-to-glucose index
OSEM	Ordered subset expectation maximization
OxFlow	Oxygenation and flow
P _a O ₂	Arterial partial pressure of oxygen
PC	Phase-contrast
pCASL	Pseudo-continuous ASL
PET	Positron emission tomography
PLD	Post-labeling delay
PMRFlow	PET/MR imaging of CBF
PMROx	PET/MR imaging of oxidative metabolism
PVE	Partial volume effect
qBOLD	Quantitative BOLD

QSM	Quantitative susceptibility mapping
R_2	Transverse relaxation rate
ROI	Region-of-interest
RW	Recirculating water
S_aO_2	Arterial oxygen saturation
S_vO_2	Venous oxygen saturation
SBO	Susceptibility-based oximetry
SD	Standard deviation
SI	Signal intensity
SPM	Statistical parametric mapping
SPSS	Statistical package for the social sciences
SSS	Superior sagittal sinus
T	Tesla, unit of magnetic induction or magnetic flux density
T_1	Longitudinal relaxation time constant
T_2	Transverse relaxation time constant
TAC	Time-activity curve
TE	Echo time
TI	Inversion time
TR	Repetition time
TRUST	T_2 -relaxation under spin tagging
VENC	Velocity encoding
VOI	Volume-of-interest
WB	Whole brain
WNLLS	Weighted non-linear least squares
WM	White matter

List of variables

Variable	Description	Unit
α	Labelling efficiency	
γ	Gyromagnetic ratio for hydrogen	MHz/T
λ	Blood-brain partition coefficient for water	mL/100 g
θ	Angle between SSS and main magnetic field	Radians
ϕ	Phase component of the MRI signal	Radians
ϵ_{RW}	RW residual function	mLO ₂ /100 g/min
ϵ_{V_A}	V_A residual function	mLO ₂ /100 g/min
ϵ_{V_0}	V_0 residual function	mLO ₂ /100 g/min
τ	Dispersion constant	s
$\Delta\chi_{do}$	Difference in magnetic susceptibility between fully oxygenated and fully deoxygenated hemoglobin	p.p.m.
$A_o(t)$	Oxygen-only component of the [¹⁵ O]O ₂ AIF	kBq/g
$A_w(t)$	Recirculating water component of the [¹⁵ O]O ₂ AIF	kBq/g
B_0	Main magnetic field	T
$C_a^o(t)$	[¹⁵ O]O ₂ arterial input function	kBq/g
$C_a^w(t)$	[¹⁵ O]H ₂ O arterial input function	kBq/g
$C_a^{co}(t)$	[¹⁵ O]CO or [¹¹ C]CO arterial input function	kBq/g
C_aO_2	Arterial content of oxygen	mLO ₂ /100 mL
$C_b^w(t)$	[¹⁵ O]H ₂ O brain tissue activity concentration	kBq/mL
$C_b^o(t)$	[¹⁵ O]O ₂ brain tissue activity concentration	kBq/mL
$C_{PET}^w(t)$	PET [¹⁵ O]H ₂ O activity concentration measurement	kBq/mL
$C_{PET}^o(t)$	PET [¹⁵ O]O ₂ activity concentration measurement	kBq/mL
CV	Coefficient of variation	%
$CMRO_2$	Cerebral metabolic rate of oxygen	mLO ₂ /100 g/min
E	Oxygen extraction fraction	
f	Cerebral blood flow	mL/100 g/min
F_v	Effective venous fraction	
Hb	Hemoglobin concentration	g/100 mL
Hct	Hematocrit concentration	%
i	Subscript for local measurements	

k	RW production rate	min^{-1}
k_w	Influx rate constant of RW from blood to whole body	min^{-1}
k_2	Efflux rate constant of RW from blood to whole body	min^{-1}
K_1^w	Influx rate constant of $[^{15}\text{O}]\text{H}_2\text{O}$ from blood to brain tissue	$\text{mL}/100 \text{ g}/\text{min}$
K_1^o	Influx rate constant of $[^{15}\text{O}]\text{O}_2$ from blood to brain tissue	$\text{mLO}_2/100 \text{ g}/\text{min}$
k_2^w	Efflux rate constant of $[^{15}\text{O}]\text{H}_2\text{O}$ from brain tissue to blood	min^{-1}
LD	Labeling duration	ms
M	Calibration constant in calibrated BOLD experiments	
$P_a\text{O}_2$	Partial pressure of oxygen	mmHg
PLD	Post labeling duration	ms
R_{Hct}	Small-to-large-vessel hematocrit ratio	
R_2	Transversal relaxation rate	s^{-1}
R_2^*	Observed transversal relaxation rate	s^{-1}
R_2'	Transversal relaxation rate due to magnetic field inhomogeneities	s^{-1}
$S_a\text{O}_2$	Arterial saturation of oxygen	%
$S_v\text{O}_2$	Venous saturation of oxygen	%
$SI_{control}$	Signal intensity of control images	
SI_{label}	Signal intensity of label images	
SI_{PD}	Signal intensity of proton density-weighted images	
v_{\perp}	Through-plane velocity	cm/s
V_A	Arterial cerebral blood volume	$\text{mL}/100 \text{ g}$
V_B	Total cerebral blood volume	$\text{mL}/100 \text{ g}$
V_0	Combination of arterial and venous cerebral blood volumes	$\text{mL}/100 \text{ g}$
$VENC$	Velocity encoding	cm/s
t	Time	min
T	Integration or PET scan time	min
T_{1_b}	Longitudinal relaxation time of blood	ms
TE	Echo time	ms
wb	Subscript for whole-brain measurements	

Chapter 1

1 Introduction

1.1 Cerebral hemodynamics and metabolism

The brain not only requires a constant supply of energy to maintain normal function, but pound for pound, it uses far more energy than any other organ. Despite only accounting for 2% of body mass, the adult human brain accounts for nearly 15% of total cardiac output, 20% of total oxygen utilization, and 25% of glucose consumption. As it has negligible energy reserves, the brain is also extremely sensitive to disruptions in energy supply, with irreversible damage occurring within minutes following a significant drop in blood flow. Blood is delivered to the brain via the carotid and vertebral arteries. When it reaches the small arterioles and capillaries, oxygen exchange occurs with the surrounding tissue, along with delivery of glucose and nutrients, such as vitamins.¹ The draining blood is collected in the cerebral venous system, which drains into the internal jugular veins. The superior cerebral veins collect blood from the cortex and white matter above the corpus callosum and drains into the superior sagittal sinus. Blood from lower portions of the brain, including the cerebellum, is drained by internal veins that merge with the straight sinus.²

Cerebral blood flow (CBF) is directly proportional to cerebral perfusion pressure (CPP), which is defined as the difference between mean arterial pressure and intracranial pressure (or the cerebral venous pressure, whichever is higher), and is inversely proportional to vascular resistance. The latter is mostly driven by diameter changes in arterioles, which occur in response to changes in CPP. Constancy of CBF is obtained by a mechanism known as cerebral autoregulation, in which a variety of physiological factors are involved in regulating cerebral circulation to maintain a constant supply of blood. In addition, CBF can be altered in response to neuronal activity, i.e., neurovascular coupling.³ Figure 1.1 shows the predicted relationship between CBF and CPP across the normal cerebral autoregulation range, in which changes in cerebral blood volume (CBV) help maintain a constant CBF, as well as in the hypo- and hyperperfusion extremes. More recent models suggest that the limits of the autoregulation plateau vary considerably due to multiple factors, including changes in cardiac output, carbon dioxide blood levels, and cerebrovascular diseases.^{4,5}

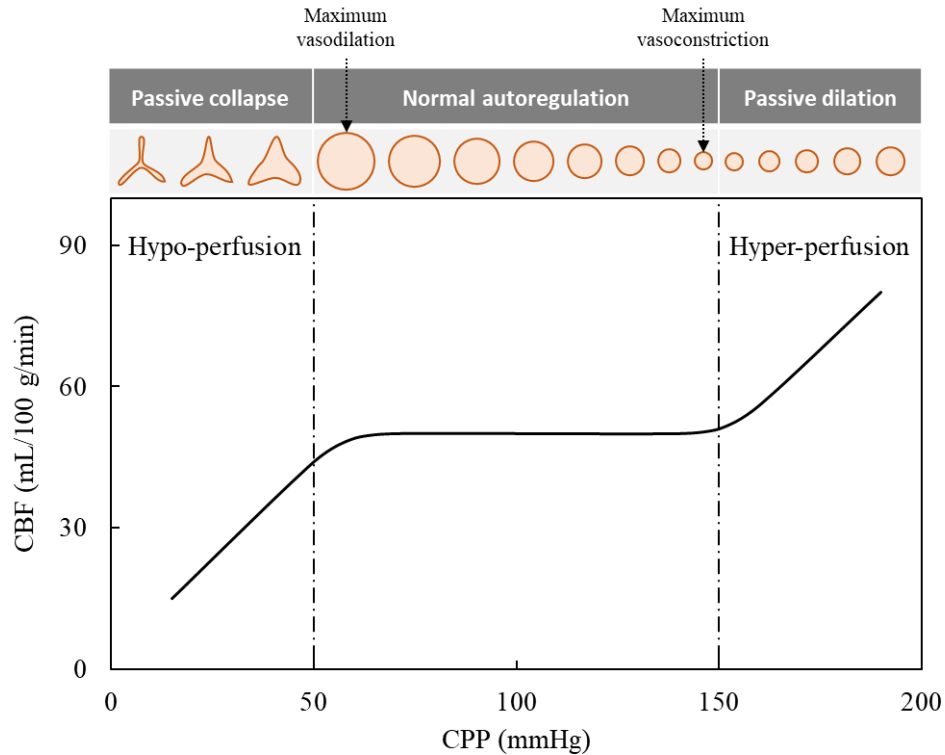


Figure 1.1. Cerebral autoregulation. Graph illustrates the theoretical change in CBF as a function of CPP, where the range of normal cerebral autoregulation is predicted to be between 50 and 150 mmHg. In this range, CBV is adjusted through alterations in vessel diameter to maintain constant CBF. Damage due ischemia may occur in low perfusion condition (hypo-perfusion). The low CPP levels in combination with low CBF leads to vessel passive collapse during hypo-perfusion, while high CPP leads to vessel passive dilation during hyper-perfusion as the vessels reach their vasoconstriction limit.

More than half of the oxygen required by the brain tissue at rest is extracted from the capillaries, and as the demand for energy increases due to neuronal activation, so does perfusion and oxygen utilization due to neurovascular coupling.³ Under normal condition, the oxygen extraction fraction (OEF) is coupled to perfusion in such way that an increase in CBF leads to a reduction in OEF (and vice-versa) to maintain constant O_2 delivery, since energy production is overwhelmingly aerobic. This CBF-metabolism coupling is non-linear such that large increases in CBF are associated with smaller increases in the cerebral metabolic rate of oxygen (CMRO₂).⁶

1.2 Clinical relevance

Estimates of cerebral hemodynamics and metabolism play an important role in understanding cerebrovascular diseases,⁷ such as stroke,^{8,9} carotid stenosis and occlusion,¹⁰ and Moyamoya disease.¹¹ Given the critical function of flow-metabolic coupling to brain health,

hemodynamic and metabolic dysfunction is also relevant to diabetes,¹² drug addiction,¹³ cancer,¹⁴ and neurodegenerative diseases,¹⁵ including mild cognitive impairment,¹⁶ Alzheimer's¹⁷ and Parkinson's disease,¹⁸ frontotemporal dementia,¹⁹ and dementia with Lewy bodies.²⁰

One of the most important applications of CBF, OEF and $CMRO_2$ imaging is to assess cerebral ischemia caused by cerebrovascular diseases such as carotid stenosis and stroke.^{21–23} In these cases, constant oxygen delivery is maintained despite low CBF levels by increasing OEF; however, this compensatory mechanism will fail below a certain CBF threshold (~ 20 mL/100 g/min), resulting in irreversible tissue damage (Figure 1.2).²⁴ Therefore, measuring OEF and $CMRO_2$ can help assess tissue viability^{9,25} and decide if invasive revascularization surgery, such as carotid endarterectomy, would be beneficial (Figure 1.3).^{26–29} Positron emission tomography (PET) imaging of OEF and $CMRO_2$ with [^{15}O]O₂ has proven fundamental in identifying the time window for reperfusion treatment with positive outcomes in acute stroke.³⁰ Furthermore, abnormal increases in OEF are associated with increased risk of stroke in patients with carotid artery occlusion (Figure 1.4).^{31,32}

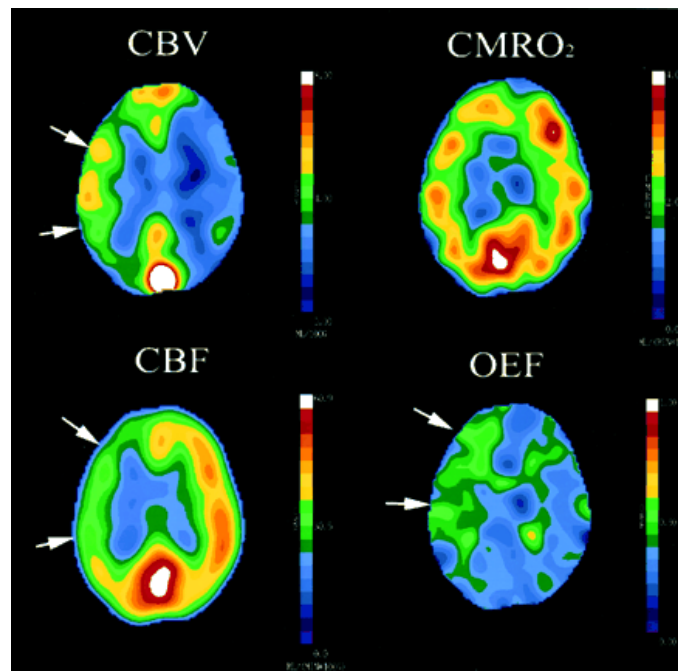


Figure 1.2. CBV, CBF, OEF and $CMRO_2$ in stage 2 hemodynamic failure. In this case, cerebral autoregulation acted by increasing CBV (top-left) to stabilize CBF (bottom-left); however, due to the stage of hemodynamic failure, autoregulatory vasodilation is not enough and ischemic regions can be observed (arrows). Then, the CBF-metabolism coupling acted by increasing OEF (bottom-right) to maintain normal oxidative metabolism ($CMRO_2$, top-right). This figure was reproduced from Derdeyn *et al.* (2002), *Brain*,²⁴ with permission provided by Oxford University Press and Copyright Clearance Center.

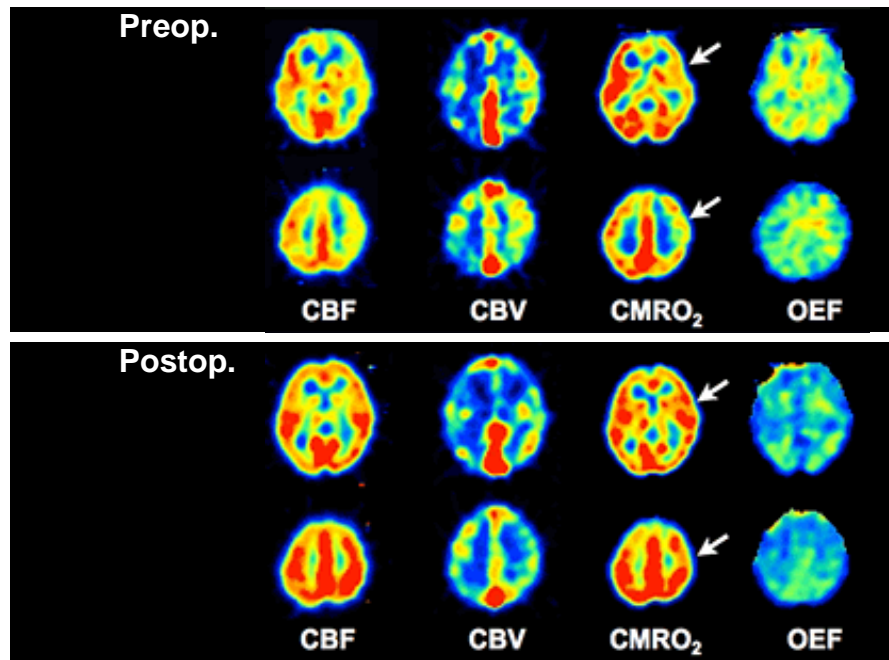


Figure 1.3. Cerebral metabolism in pediatric patient with Moyamoya disease. Pre and post revascularization surgery CBF, CBV, CMRO₂ and OEF maps obtained with [¹⁵O]-PET in which CBF, OEF and CMRO₂ returned to normal levels after revascularization surgery (see arrow). In these images, cold colours (blue) indicate low values, while warm colours (red) indicate high values. This figure was reproduced from Kuroda *et al.* (2014), *Stroke*,²⁸ with permission provided by Wolters Kluwer Health, Inc., and Copyright Clearance Center.

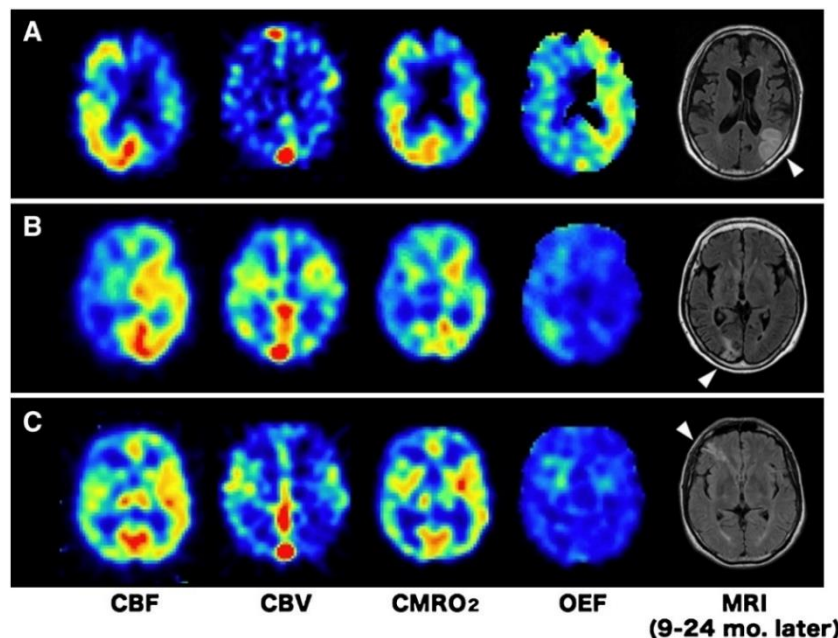


Figure 1.4. Increased OEF in patients with carotid artery occlusion. CBF, CBV, CMRO₂ and OEF measurements with [¹⁵O]-PET from three patients (A-C) with occlusive carotid artery disease in which hypoperfusion led to compensatory increases in OEF. In these examples, ipsilateral infarctions (arrows) were observed in follow-up magnetic resonance images near regions of increased OEF. In these images, cold colours (blue) indicate low values, while warm colours (red) indicate high values. This figure was reproduced from Hokari *et al.* (2009), *Surgical Neurology*,³¹ with permission provided by Elsevier and Copyright Clearance Center.

[^{15}O]O $_2$ -PET has not only significantly contributed to understanding and managing cerebrovascular diseases, but it has also been key to understanding cerebral metabolism regulation in the healthy brain. For example, the seminal study by Fox and Raichle showed that large increases in CBF yielded smaller CMRO $_2$ changes during neuronal activation (visual task),³³ contradicting the initial concept of a one-to-one relationship between these quantities. In contrast, increases in the cerebral metabolic rate of glucose (CMRGlc) were similar in magnitude to CBF, indicating greater anaerobic glycolysis during functional activation (i.e., a shift to using lactate as fuel instead of undergoing phosphorylation). Thus, the total-to-oxidative glycolysis difference was suggested as a metric of aerobic glycolysis (AG),³⁴ which is present in the normal brain during resting state.³⁵ Age-related reductions in regional AG have been observed (Figure 1.5),³⁶ and lower AG is associated with higher tau deposition in early-stage Alzheimer's disease patients.³⁷

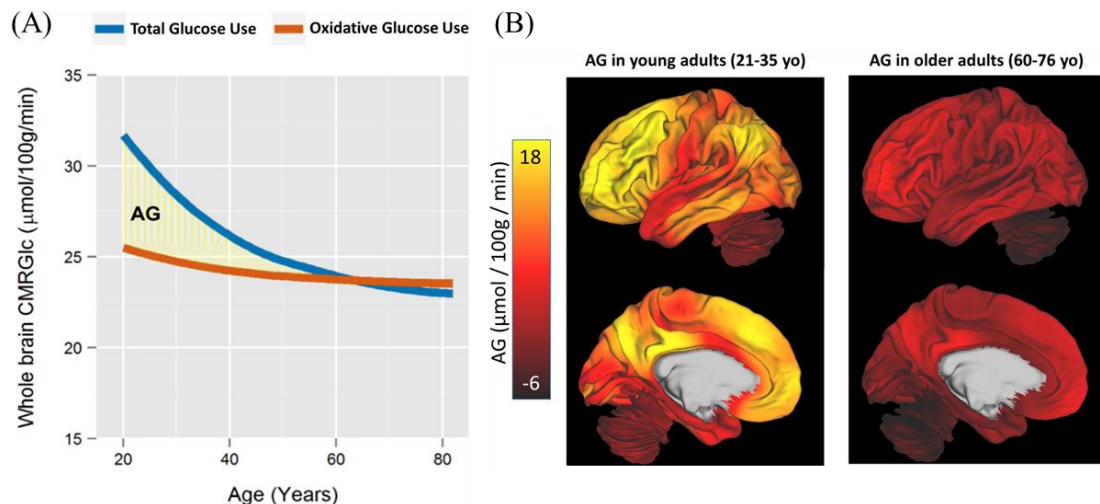


Figure 1.5. Aerobic glycolysis reduction in normal aging. (A) Whole brain CMRGlc as a function of time obtained by performing a meta-analysis of 15 studies, in which AG decreases with age. (B) AG maps showing decreased values in older adults (right) when compared to young individuals (left). As AG measurements did not include other energy sources (e.g., lactate), negative values were observed. These figures were reproduced from Goyal *et al.* (2017), *Cell Metabolism*,³⁶ with permission provided by Elsevier and Copyright Clearance Center.

1.3 Quantification of cerebral hemodynamics and metabolism

In 1944, Kety & Schmidt measured the difference between arterial and venous concentrations of nitrous oxide (N $_2$ O) to estimate global CBF.³⁸ In their seminal study, the authors adapted Fick's principle to characterize the arteriovenous concentration difference of N $_2$ O, which was later modified to include the blood-brain partition coefficient of N $_2$ O.³⁹

Concomitant to measuring CBF, $CMRO_2$ was determined by measuring the arteriovenous O_2 difference, and whole brain (WB) values for healthy young men were reported as 3.3 ± 0.4 mL/100g/min and 54 ± 12 mL/100g/min for $CMRO_2$ and CBF, respectively,³⁹ marking the first record of these quantities in the literature.

Soon after the method was developed, effects of CO_2 on CBF were investigated, and evidence of increased CBF during CO_2 inhalation was reported.^{40–42} However, substantial changes in CBF were not well explained by the small changes in mean transit times induced by increased CO_2 arterial tension,⁴³ which led to the hypothesis of the role of CBV in increasing CBF. Initial measures of CBV using [^{15}O]carbon monoxide (CO) were acquired in monkeys with external scintillator detectors and the authors found that CBV changes were related to concurrent CBF changes by approximately the cube root: $CBV = 0.80 CBF^{0.38}$.^{41,44} However, this CBV-CBF association, also known as the Grubb relationship, fails during pathological conditions.⁴⁵

With the introduction of short-lived radioisotopes in nuclear medicine,⁴⁶ radiolabelled water was used as a CBF tracer in humans.⁴⁷ The first study to measure regional cerebral oxygen utilization in humans used a combination of [^{15}O]-labelled water and oxyhemoglobin injected into the carotid artery, and recorded the signals by scintillation probes;⁴⁸ however, the invasiveness of the method limited its applicability. Later, a method was proposed to image OEF, CBF, and ultimately $CMRO_2$, based on constant inhalation of [^{15}O]O₂ and [^{15}O]CO₂.^{49–51} As [^{15}O]O₂ is inhaled, it binds to hemoglobin and is delivered throughout the body. Once in the tissue, [^{15}O]O₂ dissociates from the hemoglobin and it is quickly metabolized into [^{15}O]H₂O by the cytochrome *c* oxidase enzyme with negligible [^{15}O]O₂ back diffusion: $4 Fe^{2+}$ -cytochrome *c* + $8 H^+$ _{in} + [^{15}O]O₂ → $4 Fe^{3+}$ -cytochrome *c* + $2 [^{15}O]H_2O$ + $4 H^+$ _{out}.⁵² A consequence of the rapid conversion to water is signal contamination from metabolically generated [^{15}O]H₂O, which is referred to as recirculating water (RW).⁴⁹

The constant inhalation method was later implemented using PET,^{53–56} and values of normal CBF, OEF and $CMRO_2$ for grey matter (GM) were 65.3 ± 7.2 mL/100 g/min, 0.49 ± 0.02 , and 5.9 ± 0.6 mL/100 g/min, respectively. The advantage of adapting these methods to PET imaging is clearly the ability to extract estimates of regional blood flow and metabolism.⁵⁷ Limitations with ^{15}O imaging with the constant inhalation method include the

complexity of the inhalation system required to delivery radioactive gases, the long scan time during which the brain is assumed to remain in the same physiological state, tissue heterogeneity,⁵⁸ and the relatively higher radiation dose to the subject compared to the bolus infusion method.

1.4 Positron emission tomography

PET is a medical imaging modality that is widely used to identify changes in energy metabolism associated with pathophysiological processes, such as in cancer staging and treatment planning, as well as cardiac and neurologic diagnosis.^{59,60} Tracers used in PET are labelled with positron-emitting radionuclides (e.g., ^{15}O , ^{11}C and ^{18}F). Emitted positrons will annihilate with a neighbouring electron, emitting two almost anti-parallel photons with 511 keV energy. The simultaneous detection of these photons forms the basis of PET imaging, in which the system identifies the annihilation event based on the line-of-response that connects the two detectors that detected the annihilation pair. The electronic system relates the interaction times in opposed detectors and register an event if it is within the coincidence window (typically < 12 ns).⁶¹ The distance between emission and annihilation is called the positron range, which depends on the positron kinetic energy of emission. The maximum positron kinetic energy for ^{15}O is 1.72 MeV, which yields a spatial resolution, based on the full-width half maximum (FWHM), of approximately 3 mm. For comparison, ^{18}F has a kinetic energy of 0.64 MeV, corresponding to a FWHM closer to 2 mm.⁶²

After emission, photons can partially or completely transfer their energy to electrons, resulting in their angle of trajectory being altered (i.e., Compton scattering) or completely absorbed (i.e., photoelectric absorption). Considering the annihilation photons energy (511 keV) and the atomic number of the atoms that constitute the body ($Z < 20$), Compton scattering is the dominant effect in this case.⁶¹ Besides true events, PET systems also record scattered, random, single and multiple events. A scattered coincidence event happens if at least one of the annihilation pair photons is scattered; thus, the coincidence is assigned to an incorrect line-of-response. If only one of the photons is detected (e.g., the other scattered outside the field-of-view), the PET system registers either a single event, or it can be detected within the coincidence window of a different event (random coincidences).⁶¹

Quantification by PET requires estimating the true activity concentration in the organ of interest. For this, scattering and attenuation corrections are implemented to estimate activity concentrations that are closer to the true distribution. In addition, other corrections for the Poisson-distributed true events are required for quantification, including radioactive decay, random coincidences, detector dead-time (the time interval in which no event can be detected), detector normalization (related to the probability of an event being recorded after a photon interacts with the detector), and data rebinning (the process of converting oblique events into sinograms of parallel projections for image reconstruction).⁶¹

Once a tracer distribution is measured, a mathematical model can be implemented to extract relevant physiological parameters that are typically obtained by characterizing time-varying (i.e., dynamic) data after radiotracer administration.^{63,64} The uptake of the tracer in the tissue of interest depends on the underlying physiology, such as blood flow and metabolism, and its delivery via the circulatory system, which is defined by the time-varying tracer concentration in arterial blood (known as the arterial input function, or AIF). Analysis of dynamic PET data is almost exclusively performed using compartmental models that characterize tracer distributions in terms of simple first order kinetics with rate constants that govern exchange between compartments.^{63,64} These rate constants can be related to specific physiological processes and are generally estimated using optimization routines to fit a compartmental model to PET data.^{63,64} One of the first applications of compartmental modelling, which is central to this thesis, was to estimate CBF and CMRO₂, as described in the following sections.

1.4.1 Cerebral blood flow

Measuring CBF by PET after a bolus injection of [¹⁵O]H₂O is based on the one-tissue compartment model (Figure 1.6). The time rate of change of [¹⁵O]H₂O activity concentration in brain tissue, $C_b^w(t)$, depends on the concentration of labeled water delivered by arterial blood, $C_a^w(t)$ (i.e., the AIF), and the washout from tissue, which is expressed by:^{64,65}

$$\frac{d}{dt}C_b^w(t) = K_1^w \cdot C_a^w(t) - k_2^w \cdot C_b^w(t) \quad (1.1)$$

where K_1^w the influx rate constant of [¹⁵O]H₂O from the arterial blood to brain tissue, and k_2^w the efflux rate constant. K_1^w is defined as the product of the water extraction fraction and CBF

(f); however, the former is usually set equal to one, which is reasonable for CBF values below approximately 60 mL/100 g/min.⁶⁶ k_2^w is defined as the ratio of K_1^w and the blood-brain partition coefficient of water (λ). By solving this differential equation, the tissue activity concentration as a function of time is given by:

$$C_b^w(t) = f \cdot C_a^w(t) * e^{-\frac{f}{\lambda}t} \quad (1.2)$$

where the symbol $*$ represents convolution. The blood-brain partition coefficient, defined as the tissue-to-blood ratio of water content, ranges from 94 to 101 mL/100 g for GM and from 78 to 84 mL/100 g for white matter (WM), depending on the hematocrit level and the water content of blood.⁶⁷ Figure 1.7 presents a typical groupwise CBF image obtained with PET.

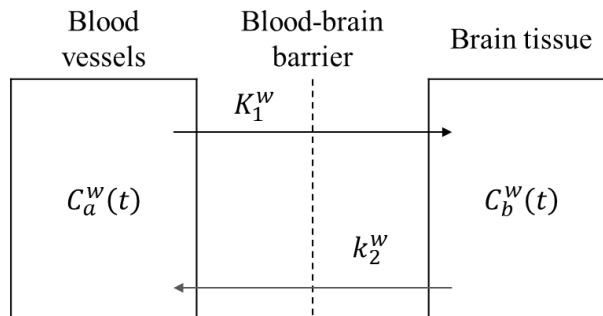


Figure 1.6. One-tissue compartment model for $[^{15}\text{O}]\text{H}_2\text{O}$. The change in $[^{15}\text{O}]\text{H}_2\text{O}$ activity concentration as a function of time, $C_b^w(t)$, due to the influx of radiolabelled water defined by the rate constant K_1^w . The rate constant, k_2^w represents the efflux of $[^{15}\text{O}]\text{H}_2\text{O}$ from tissue.

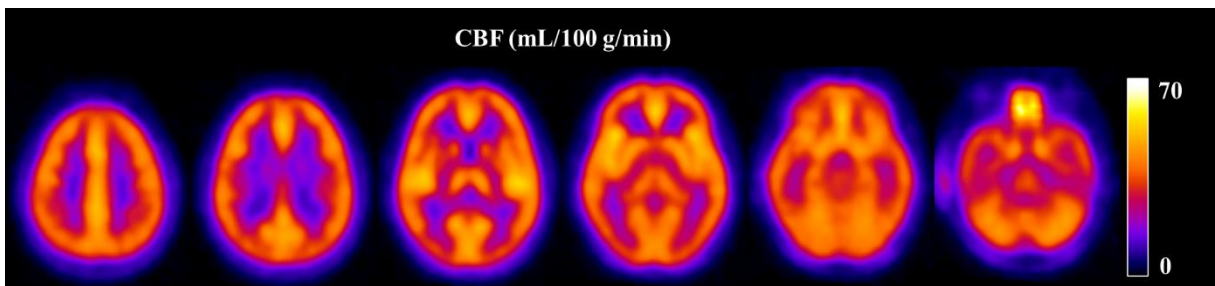


Figure 1.7. Typical CBF maps obtained with $[^{15}\text{O}]\text{H}_2\text{O}$ PET.⁶⁸ Groupwise mean CBF map ($n = 10$ healthy individuals, MNI space) obtained with the dual-tracer autoradiographic method,⁶⁹ which incorporates AIF and a separate CBV measurement (see Figure 1.10 for the corresponding CBV maps).

Common sources of error in estimating CBF include ignoring CBV contributions and neglecting the delay and dispersion of the AIF, which is measured at a peripheral artery.⁷⁰⁻⁷³ Arterial blood-borne activity can be either measured separately or incorporated into the fitting routine by including an additional term in Eq. (1.2):

$$C_{PET}^w(t) = (1 - V_A) \cdot f \cdot C_a^w(t) * e^{-\frac{f}{\lambda}t} + V_A \cdot C_a^w(t) \quad (1.3)$$

where $C_{PET}^w(t)$ is the total measured PET activity and V_A is the arterial component of the total blood volume (CBV_a). Efforts to reduce the invasiveness of the procedure have primarily focused on extracting an image-derived input function (IDIF)^{74–85} and reference region methods.^{86–90}

1.4.2 Oxygen extraction fraction

PET measurements of OEF (E) using $[^{15}\text{O}]\text{O}_2$ are also based on the one-compartment tissue model⁵² (Figure 1.8), in which the rate of change in activity concentration in brain tissue, $C_b^o(t)$, is dependent on the influx rate constant, K_1^o , of $[^{15}\text{O}]\text{O}_2$ (defined by the product of OEF and CBF; see Eq. (1.4)). Due to the rapid conversion of $[^{15}\text{O}]\text{O}_2$ to $[^{15}\text{O}]\text{H}_2\text{O}$ by metabolism, the efflux term, k_2^w , characterizes the washout of $[^{15}\text{O}]\text{H}_2\text{O}$ and efflux of $[^{15}\text{O}]\text{O}_2$ is considered negligible.^{91,92} The model also accounts for the influx of $[^{15}\text{O}]\text{H}_2\text{O}$ generated elsewhere in the body (i.e., K_1^w). The arterial activity concentration, $C_a^o(t)$ is given by the sum of the blood contents of hemoglobin-bound $[^{15}\text{O}]\text{O}_2$, $A_o(t)$, and RW, $A_w(t)$. The solution to Eq. (1.4) is shown in Eq. (1.5).

$$\frac{d}{dt} C_b^o(t) = K_1^o \cdot A_o(t) + K_1^w \cdot A_w(t) - k_2^w \cdot C_b^o(t) \quad (1.4)$$

$$C_b^o(t) = E \cdot f \cdot A_o(t) * e^{-\frac{f}{\lambda}t} + f \cdot A_w(t) * e^{-\frac{f}{\lambda}t} \quad (1.5)$$

The activity measured by the PET scanner will also include CBV contributions due to $[^{15}\text{O}]\text{O}_2$ bound to hemoglobin and $[^{15}\text{O}]\text{H}_2\text{O}$ circulating in blood.⁹³ To account for these contributions, the total PET signal is given by:

$$C_{PET}^o(t) = (1 - V_B) \cdot C_b^o(t) + V_0 \cdot A_o(t) + V_A \cdot A_w(t) \quad (1.6)$$

where V_B is the total CBV (defined as the sum of arterial, capillary and venous blood volumes), and V_0 is the fraction of the total CBV given by $R_{Hct}(1 - E \cdot F_v) V_B$, where R_{Hct} is the small-to-large hematocrit ratio ($R_{Hct} = 0.85$) and F_v the effective venous fraction ($F_v = 0.835$).^{92,94}

The venous fraction appears in V_0 because most of oxygen extraction occurs at capillary level.^{92,95} After including the $[^{15}\text{O}]$ -labeled oxygen and water AIFs, a fitting routine can be incorporated to estimate OEF using Eqs. (1.5) and (1.6). CBF estimates required in Eq 1.5 are acquired by performing a separate $[^{15}\text{O}]\text{H}_2\text{O}$ PET scan (see section 1.4.1). Figure 1.9 presents groupwise OEF maps obtained with $[^{15}\text{O}]\text{O}_2$ -PET.

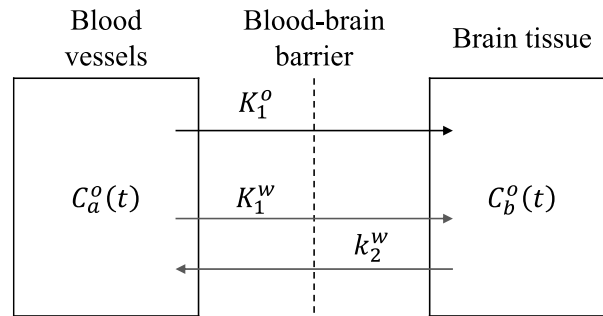


Figure 1.8. One-tissue compartment model for $[^{15}\text{O}]\text{O}_2$. The change in tissue activity as a function of time, $C_b^o(t)$, is due to the influx of radiolabelled oxygen as defined by the rate constant K_1^o . $[^{15}\text{O}]\text{O}_2$ that enters the tissue is quickly metabolized to $[^{15}\text{O}]\text{H}_2\text{O}$, which returns to the blood at a rate defined by k_2^w . The remaining rate constant, K_1^w accounts for the influx of metabolically generated $[^{15}\text{O}]\text{H}_2\text{O}$ (i.e. the RW component).

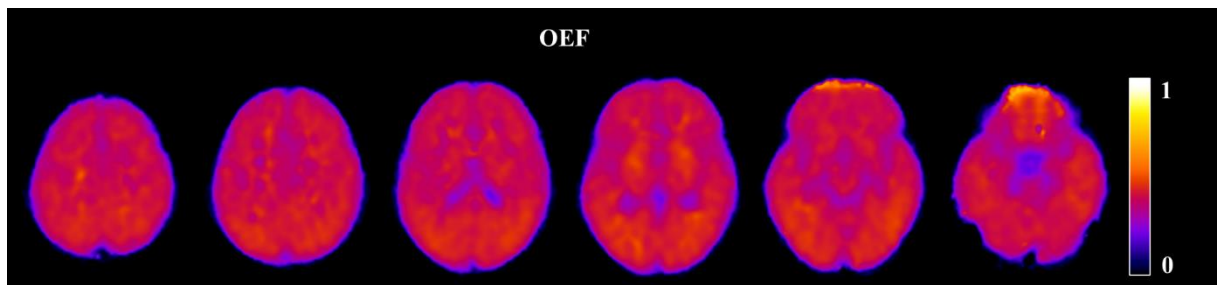


Figure 1.9. Typical OEF maps obtained with $[^{15}\text{O}]\text{O}_2$ PET.⁶⁸ Groupwise mean OEF map ($n = 10$ healthy individuals, MNI space) obtained with the dual-tracer autoradiographic method,⁶⁹ which incorporates AIF and a separate CBV measurement (see Figure 1.10 for the corresponding CBV maps). Corresponding CBF maps are shown in Figure 1.7.

Although it has been argued that RW can be ignored if the acquisition time is short,⁹¹ RW represents approximately 18% of the arterial blood activity by just 40 seconds after $[^{15}\text{O}]\text{O}_2$ administration⁹² and therefore RW correction is strongly encouraged. This correction can be performed by either measuring RW directly or by using a model to characterize whole-body water production. Iida *et al.* (1993) considered a constant RW production rate and used arterial measurements from 200 human subjects to approximate the RW arterial activity concentration as a simplified steady-state model. The production rate obtained was approximately 0.07 min^{-1} by assuming a delay of RW appearance of 20 seconds.⁹⁶ Alternatively, a more

robust two-compartment model was proposed in which the RW production rate was estimated to be around 0.13 min^{-1} .^{97,98} Significant variability in this quantity has been reported, particularly under different physiological conditions.⁹⁸

In addition to RW, CBV corrections are usually implemented, either by direct measurements or by including CBV as a fitting parameter, as described above. PET regional CBV measurements are obtained after a short inhalation of $[^{15}\text{O}]\text{CO}$ or $[^{11}\text{C}]\text{CO}$ and normal values of range from 2 to 6 mL/100 g.^{92,99–104} Figure 1.10 presents typical groupwise CBV images obtained with $[^{11}\text{C}]\text{CO}$ -PET.

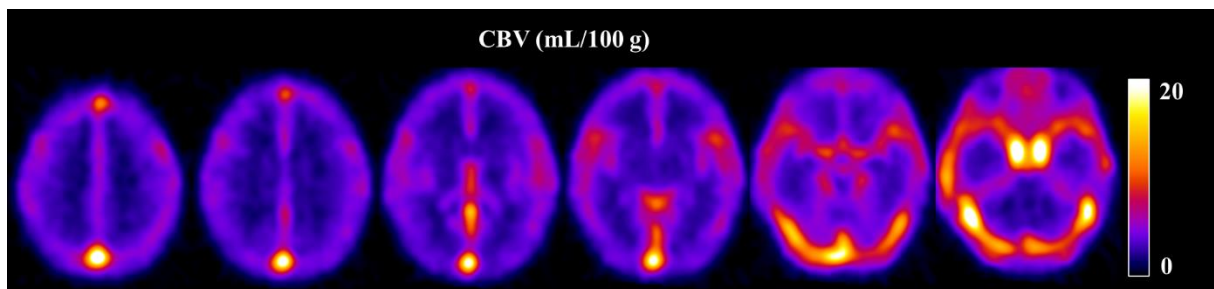


Figure 1.10. Typical CBV maps obtained with $[^{15}\text{O}]\text{CO}$ PET.⁶⁸ Groupwise mean CBV map ($n = 10$ healthy individuals, MNI space). Major vessels are particularly evident in these images.

1.4.3 Cerebral metabolic rate of oxygen

CMRO_2 is defined as the product of CBF, OEF and the arterial content of oxygen ($C_a\text{O}_2$), as given by Eq. (1.7). The arterial content of oxygen can be readily obtained by measuring the hemoglobin concentration (Hb), arterial partial pressure of oxygen ($P_a\text{O}_2$) and the arterial saturation of oxygen ($S_a\text{O}_2$), as given by Eq. (1.8).

$$\text{CMRO}_2 = E \cdot f \cdot C_a\text{O}_2 \quad (1.7)$$

$$C_a\text{O}_2 = 1.34 \cdot \text{Hb} \cdot S_a\text{O}_2 + 3 \times 10^{-3} \cdot P_a\text{O}_2 \quad (1.8)$$

where each gram of hemoglobin can transport 1.34 mL of oxygen, and the blood has 3×10^{-3} milliliters of dissolved oxygen per unit of $P_a\text{O}_2$, per 100 mL of blood.

In summary, PET imaging of CMRO_2 requires three tracers: $[^{15}\text{O}]\text{O}_2$, $[^{15}\text{O}]\text{H}_2\text{O}$ and $[^{15}\text{O}]\text{CO}$, and each requires measuring its own AIF.⁹⁹ Consequently, it is a challenging procedure due to long acquisition times, complexity and invasiveness. In addition, accuracy and

precision of [^{15}O]-PET measurements are sensitivity to partial volume effect (PVE) errors and noise in the measured PET data, as well as inaccuracies in the AIF measurements, to cite a few.⁶³ Despite these disadvantages, this three-tracer method has been successfully applied to a variety of diseases^{30,105,106} (as outlined in section 1.2) and good within- and between-sessions reproducibility has been observed (Table 1.1).^{107–112}

Table 1.1. Reproducibility of [^{15}O]-PET measurements. The coefficient of variation (COV) was reported for within- and between-session, as well as between-subjects in a multi-centre study, for regional CBF, OEF and CMRO_2 estimates in healthy individuals. COV was obtained from volumes-of-interest (see studies for additional details).

[^{15}O]-PET measurement	COV			Studies
	Within-session	Between-sessions	Between-subjects	
CBF	5-10%	9-11%	5-23%	Coles <i>et al.</i> , ¹⁰⁹
OEF	6%	9-10%	2-13%	Bremmer <i>et al.</i> , ¹¹¹
CMRO_2	5%	4-7%	6-25%	and Ito <i>et al.</i> ¹¹²

Simplifications to the gold standard include a dual-tracer autoradiographic method (DARG) that was developed to reduce scan duration (see Figure 1.11 for groupwise CMRO_2 maps obtained with DARG).⁶⁹ DARG enables CMRO_2 measurements under different physiological conditions due to its short acquisition time (approx. 5 min) in which [^{15}O] O_2 and [^{15}O] H_2O (or [^{15}O] CO_2) are administered sequentially (in any order); however, an additional scan to measure CBV is still required and careful attention is needed to separate the activity concentration from each tracer due to the overlap caused by the immediate administration of the second tracer.¹¹³ To remove the need for the CBV scan, a dual-basis function model (DBFM) was developed,¹¹⁴ in which Eq. (1.6) was modeled as two basis function and two terms for blood volumes.

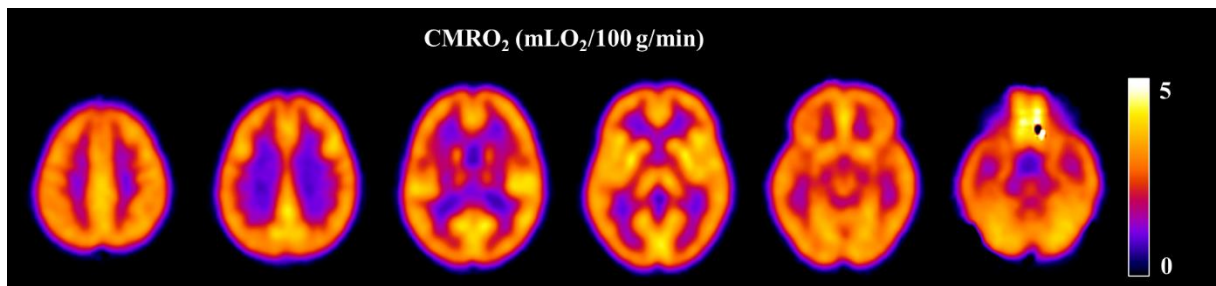


Figure 1.11. Typical CMRO_2 maps obtained with [^{15}O] O_2 PET.⁶⁸ Groupwise mean CMRO_2 map ($n = 10$ healthy individuals, MNI space) obtained with the dual-tracer autoradiographic method,⁶⁹ which incorporates AIF and a separate CBV measurement (see Figure 1.10). Corresponding CBF and OEF maps are shown in Figure 1.7 and Figure 1.9, respectively.

1.5 Magnetic resonance imaging

Non-invasive and radiation-free alternatives to the [^{15}O]-PET approaches have been proposed with magnetic resonance imaging (MRI). The following sections present a brief review of MR sequences that have been developed to image CBF, OEF and CMRO_2 .

1.5.1 Cerebral blood flow

Almost 50 years after the first CBF measurements in humans with nitrous oxide, Detre *et al.* reported CBF measurements with MRI in a rodent model, marking the beginning of arterial spin labelling (ASL).¹¹⁵ ASL is now a widespread MRI technique that uses water in arterial blood as an endogenous contrast agent to image cerebral perfusion.¹¹⁶ Despite ASL being completely non-invasive and quantitative, contrast-enhanced techniques, particularly dynamic susceptibility contrast (DSC) MRI, are used much more frequently in clinical practice.¹¹⁷ DSC MRI provides greater signal-to-noise compared to ASL, the acquisition time is typically shorter, and it can map CBF, CBV and mean transit time by tracking the time-varying signal change following the intravenous injection of a gadolinium-based contrast agent.¹¹⁸ However, these contrast agents are not without risk, particularly for patients with renal insufficiency, and the approach is clearly not well suited for tracking changes in cerebral hemodynamics.¹¹⁹ Consequently, the choice to use either contrast-enhanced MRI or ASL to image CBF depends on the application. ASL is more suited for tracking rapid perfusion changes (i.e., over a few seconds), such as during functional activation, and for longitudinal monitoring since quantification is easier to perform. In addition, avoiding the use of a contrast agent makes ASL easily adapted to MRI protocols.¹²⁰

In terms of global CBF, phase contrast (PC) MRI was proposed as a non-invasive technique that encodes the phase of flowing spins in major vessels (e.g., large arteries feeding the brain) to measure the in-plane velocity of blood.¹²¹ Given its relatively short acquisition time and high reproducibility,^{122,123} PC MRI has been implemented in a variety of studies.^{88,90,124–126} In the next sections, PC MRI and ASL are described in more detail as these sequences were implemented in the work reported in this thesis.

1.5.1.1 Phase contrast MRI

As mentioned above, PC MRI can estimate WB CBF due to its sensitivity to in-plane velocity (v_{\perp}) of blood flowing through a major artery. Thus, by encoding the velocity of spins (VENC, or velocity encoding), arterial blood velocity can be estimated by measuring the phase change within the vessel of interest ($\Delta\phi$):

$$v_{\perp} = VENC \cdot \frac{\Delta\phi}{\pi} \quad (1.9)$$

where $|\Delta\phi| \leq \pi$ radians. WB CBF is determined by multiplying the blood velocity (v_{\perp}) measured in the carotid and vertebral arteries by the vessels cross-sectional area, normalizing the result by the total brain volume, and making proper unit conversions. Limitations with PC MRI include PVE errors due to insufficient spatial resolution to resolve the arterial lumen, variations in flow across the cardiac cycle, and sensitivity to inappropriate positioning of the imaging plane.^{127,128} Differences in parameters between PC sequences reported in the literature can also impose limitations, as suggested by the inconsistencies observed in some studies that reported overestimation of global CBF by PC MRI compared to [^{15}O]H $_2\text{O}$ PET.^{76,126,129} Finally, one must be careful when selecting the appropriate velocity encoding, as aliasing can occur when $|v_{\perp}| > VENC$, while using too large of a VENC will impact the signal-to-noise ratio. The main steps to obtain global CBF are shown in Figure 1.12.

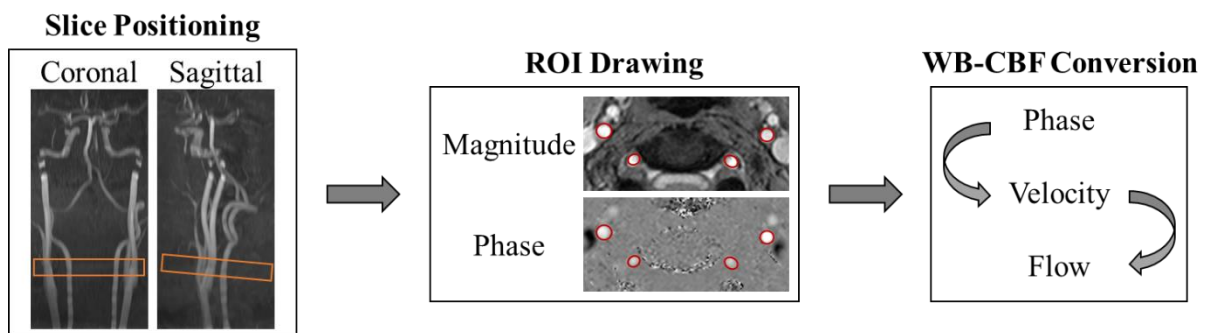


Figure 1.12. PC-MRI scheme. The slice used to acquire PC-MRI data must be positioned above the carotid bifurcation and perpendicular to the internal carotid and vertebral arteries (left, in orange; images are time-of-flight maximum-intensity projections). Then, phase measurements are extracted by transferring semi-automatically drawn regions-of-interest (ROIs) in the magnitude image to the phase image (center, in red). Lastly, phase measurements are converted into velocity with Eq. (1.9), and into CBF by multiplying by the vessel cross-sectional area and by normalizing by WB volume (obtained from the anatomical image).

1.5.1.2 Arterial spin labelling

Quantification of regional CBF by ASL is based on magnetically labelling arterial blood by applying RF pulses. The signal related to perfusion is obtained by taking the difference between images acquired with and without labelling. A post-labelling delay (PLD) is incorporated into the sequence to allow for the labelled arterial blood to reach the brain, prior to image acquisition.¹¹⁶ ASL sequences can be generally classified as either pulsed (i.e. one labelling pulse) or continuous (i.e. a series of labelling pulses). Eq. (1.10) presents the equation used to convert the signal change into CBF for a continuous labelling scheme.

$$CBF = \frac{6000 \cdot \lambda \cdot (SI_{control} - SI_{label}) \cdot e^{PLD/T_{1b}}}{2 \cdot \alpha \cdot T_{1b} \cdot SI_{PD} \cdot (1 - e^{-LD/T_{1b}})} \quad (1.10)$$

where $SI_{control}$ and SI_{label} are the control and label signal intensities, PLD the post-labelling delay ($PLD = 1800$ ms for healthy individuals),¹¹⁶ LD the labelling duration ($LD = 1800$ ms),¹¹⁶ T_{1b} the longitudinal relaxation time of blood ($T_{1b} = 1650$ ms at 3 T),¹³⁰ λ the blood-brain partition coefficient of water ($\lambda = 0.90$ mL/g),⁶⁷ α the labelling efficiency, and SI_{PD} the signal intensity of the proton density-weighted image (M_0). Figure 1.13 shows a scheme of CBF quantification by continuous ASL and a typical group-wise CBF map acquired with ASL from healthy individuals is presented in Figure 1.14.

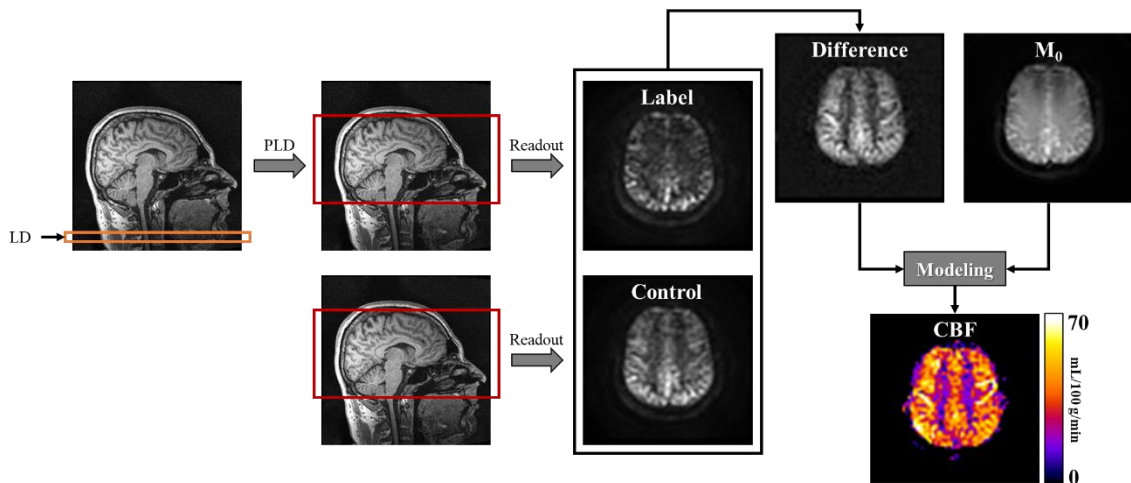


Figure 1.13. ASL acquisition scheme. ASL acquisition (readout) happens after labelling arterial blood for a certain amount of time (labelling duration, or LD) and waiting for it to reach brain tissue (post labeling delay, or PLD), from which label images are obtained. Control images are obtained without any labelling. The difference between control and label images are used in the single compartment

model given by Eq. (1.10), which requires the proton density-weighted image (M_0) and results in CBF maps.

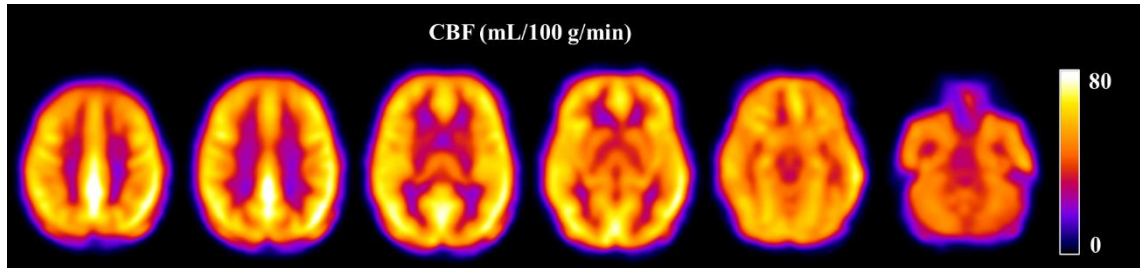


Figure 1.14. Typical CBF maps obtained with pseudo-continuous ASL. Groupwise mean CBF map ($n = 13$, healthy individuals, MNI space).

ASL has been compared to the $[^{15}\text{O}]\text{H}_2\text{O}$ -PET procedure in previous studies, and results indicate reliable and reproducible CBF measurements;^{122,131–136} however, differences between the techniques have also been reported.¹³⁷ Such findings might be explained by some of ASL limitations, such as sensitivity to motion artifacts and PVEs,¹³⁸ differences in arterial transit time between tissues (GM vs. WM) and vascular regions (watershed artifact),¹³⁹ proper labelling plane positioning, and adequate choice of imaging parameters.¹⁴⁰ However, it is important to recall that the technique to obtain voxel-wise CBF measurements with $[^{15}\text{O}]\text{H}_2\text{O}$ -PET is also complex and comes with its own set of limitations, such as sensitivity to water extraction; thus, the general agreement between the two methods is encouraging.¹⁰⁷ Indeed, reproducibility studies observed within-session variability (measured as the GM coefficient of variation, or COV) of approximately 4-9% for ASL when repeated measurements were obtained up to 90 minutes apart,^{122,132,141} while within- and between-subjects reproducibility have been reported for GM as 5.1% and 8.6%, respectively.¹³⁶ Lastly, Heijtel *et al.* obtained similar between-sessions reproducibility when comparing pseudo-continuous ASL (COV of 12.8%) to $[^{15}\text{O}]\text{H}_2\text{O}$ -PET (COV of 14.1%) CBF measurements at rest performed one month apart. These results closely match the gold standard reproducibility, as reported in section 1.4.3 (Table 1.1).

1.5.2 Cerebral metabolism

All MRI methods proposed to map cerebral metabolism are based on the signal dependency to paramagnetic deoxyhemoglobin.¹⁴² Global oxygenation can be estimated with both relaxation- and susceptibility-based approaches by measuring WB venous oxygen saturation ($S_v\text{O}_2$). Relaxation-based techniques are based on the oxygenation dependency of the

transverse relaxation rate (R_2) of blood.¹⁴³ Amongst relaxation-based approaches, TRUST (i.e., T_2 -relaxation under spin tagging) is fast, insensitive to vessel orientation and magnetic field inhomogeneities, and S_vO_2 estimates were in agreement with $[^{15}O]$ -PET results;¹⁴⁴ however, TRUST OEF estimates require a calibration curve to relate oxygen saturation to R_2 .^{145–147} Conversely, susceptibility-based oximetry (SBO) derives OEF from the phase shift difference between the vessel of interest (i.e., superior sagittal sinus, or SSS) and the surrounding tissue.^{148,149} In a reliability study that compared TRUST to SBO, the latter presented a better agreement to the clinical gold standard—i.e., oximetry measurements in the internal jugular vein.¹⁴⁶ After estimating S_vO_2 , OEF (Eq. (1.11)) is obtained by either measuring S_aO_2 with a pulse oximeter, assuming it to be 98%, or estimating it based on P_aO_2 measurements.¹⁵⁰

$$E = \frac{S_aO_2 - S_vO_2}{S_aO_2} \quad (1.11)$$

On a WB level, S_vO_2 measurements can be combined with CBF from PC MRI to determine WB $CMRO_2$ using Eq. (1.7).^{151–154} A fast SBO technique, namely OxFlow (oxygenation and flow), was developed to sequentially estimate WB $CMRO_2$ by measuring global CBF in the feeding arteries with PC and S_vO_2 from the SSS with SBO.^{152–154}

Obtaining local estimates of $CMRO_2$ with MRI typically require a combination of regional perfusion (e.g., ASL) and oxygenation MR (e.g., quantitative susceptibility mapping, or QSM) sequences.¹⁴² QSM is a SBO approach that maps susceptibility by deconvolving the phase signal, which requires assuming that phase shifts are primarily caused by field inhomogeneities due to susceptibility effects.^{155,156} Given the relationship between magnetic susceptibility and oxygen saturation, local metabolism can be mapped.^{157,158} QSM have generated promising OEF maps when compared to $[^{15}O]O_2$ -PET;^{159,160} however, the complexity of the method limits its application due to the sophisticated phase unwrapping, and deconvolution and regularization approaches needed to obtain reliable magnetic susceptibility maps.^{161–163}

Alternatively, $CMRO_2$ can be obtained with functional MRI (fMRI) experiments due to the dependency of the transverse relaxation rate (R_2) to deoxyhemoglobin concentration in blood, which is the base of blood-oxygen level-dependent (BOLD) signal.^{164,165} The next section explains in further details the OxFlow technique, since this SBO approach was

implemented in the experiments described in this thesis. Additionally, quantitative- and calibrated-BOLD methods are briefly introduced as possible alternatives to measure baseline CMRO₂.

1.5.2.1 OxFlow: oxygenation and flow

OxFlow produces global estimates of CMRO₂ by combining CBF (from PC MRI, see section 1.5.1.1) and S_vO₂.¹⁵³ For the latter, ROIs are drawn in and surrounding the SSS on the magnitude image and transferred to the phase image to measure the mean phase difference, $\Delta\phi_{ie}$, between the vessel and the surrounding tissue ($\Delta\phi_{ie} = \Delta\phi_{intra} - \Delta\phi_{extra}$), as shown in Figure 1.15. Determining S_vO₂ also requires measuring the angle between the SSS and the main magnetic field, which is typically determined with time-of-flight images. A correction for the magnetic field inhomogeneities is applied before extracting phase measurements. After all required measurements are obtained, S_vO₂ is determined by:¹⁵⁴

$$S_vO_2 = 1 - \frac{2\Delta\phi_{ie}}{\gamma \cdot B_0 \cdot \Delta TE \cdot \Delta\chi_{do} \cdot Hct \cdot \left(\cos^2\theta - \frac{1}{3}\right)} \quad (1.12)$$

where γ is the gyromagnetic ratio for ¹H, B_0 the main magnetic field strength, ΔTE the inter-echo time, $\Delta\chi_{do}$ the susceptibility difference between fully oxygenated and deoxygenated hemoglobin ($\Delta\chi_{do} = 4\pi \cdot 0.27$ parts per million), Hct the hematocrit level, and θ the angle between the SSS and the main magnetic field.

A comparison between OxFlow measurements from three sessions acquired 5 to 10 minutes apart resulted in low variability (COVs of 2.3%, 3.1% and 3.2% for S_vO₂, CBF and CMRO₂, respectively) and high reliability (intraclass correlation coefficients of 0.98, 0.97 and 0.94 for S_vO₂, CBF and CMRO₂, respectively).¹⁵³ Subsequently, Barhoum *et al.* performed repeated measurements of CMRO₂ with OxFlow and obtained high within-subject reproducibility (COV of 0.4-5.5%, 2.5-11.1% and 1.1-8.2% for S_vO₂, CBF and CMRO₂, respectively). Furthermore, OxFlow presented similar results when compared to a PET technique (DBFM) in animal experiments,¹⁶⁶ and it has the potential to track changes in CMRO₂ due to its fast implementation, with the possibility to collect the data required for S_vO₂ and CBF in 8 seconds.¹⁵²

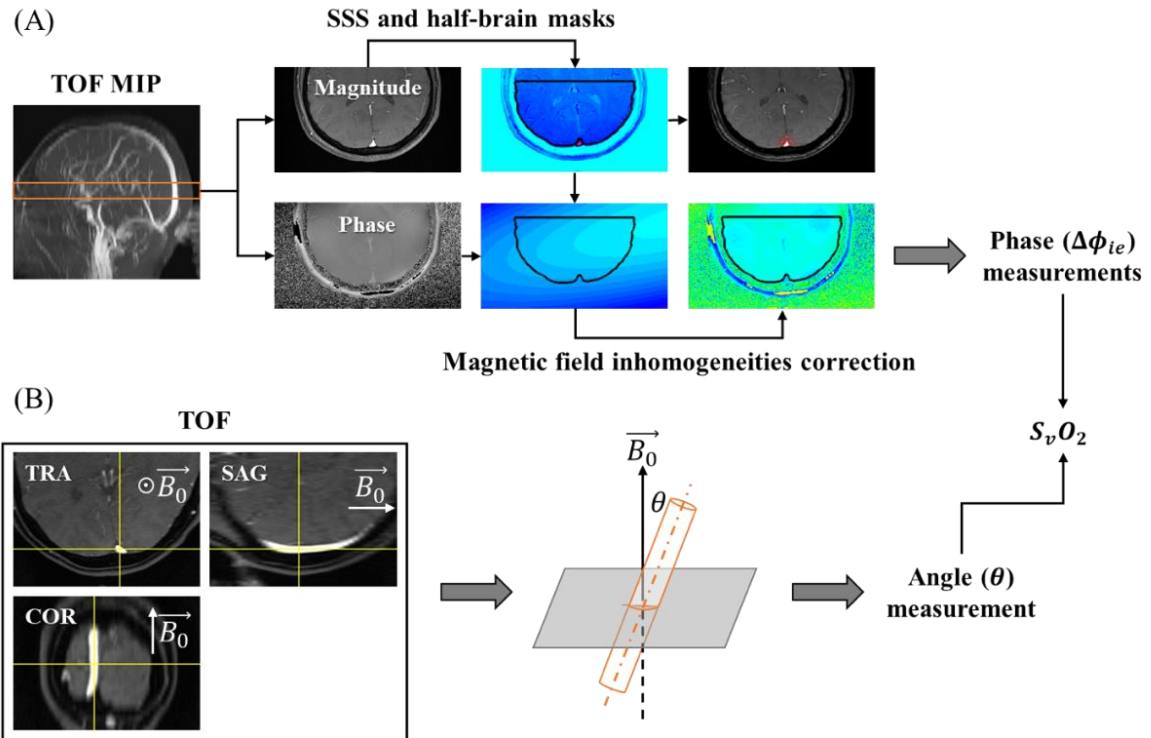


Figure 1.15. SBO steps to obtain global venous oxygen saturation. (A) Based on the time-of-flight (TOF) maximum-intensity projection (MIP), the SBO plane is positioned on the superior sagittal sinus (SSS), as shown in orange. The magnitude component of the acquired MR image is used to generate the brain and SSS masks, as well as the tissue surrounding the SSS (top-right-most image). Additionally, the phase image is used to estimate a correction for the magnetic field inhomogeneities. The last step is to extract intra- and extra-vascular phase measurements. (B) The last quantity needed to estimate the venous oxygen saturation (S_vO_2) with Eq. (1.12) is the angle (θ) between the SSS and the main magnetic field (B_0), as represented on the bottom-middle figure. For this purpose, TOF images are used and the centroid of the SSS is estimated for a few consecutive slices. TRA: transversal plane; COR: coronal plane; SAG: sagittal plane.

1.5.2.2 Blood-oxygen level-dependent

During neuronal activation, the increase in deoxyhemoglobin in the blood induces changes in the observed R_2 signal, which are used to model the BOLD signal to estimate local changes in $CMRO_2$.^{167,168} This signal change is due to the sensitivity of the transverse relaxation rate to magnetic field inhomogeneities induced by the susceptibility difference between the vessels and the surrounding tissue, which are due to increases in paramagnetic deoxyhemoglobin; thus, the observed relaxation rate, R_2^* , is higher than the real R_2 . However, the change in the fMRI signal is characterized by an intricate relationship between CBF, $CMRO_2$, and the baseline state, which, in turn, depends on OEF, CBV, and hematocrit levels. Thus,

relative changes in CMRO_2 can be estimated by combining the BOLD signal with corresponding changes in CBF measured by ASL.

Quantitative BOLD (qBOLD) is able to provide regional measurements of tissue oxygenation by assuming the microcirculation can be model as randomly oriented and uniformly distributed cylinders.^{169–172} The concept is to separate the signal from magnetic field inhomogeneities (given by $R_2' = R_2^* - R_2$) originated by the blood vessels from other sources (e.g., body-air interface and magnetic field imperfections).¹⁷⁰ This separation is performed by fitting multiple parameters that describe different contributions to the measured R_2' -sensitive free-induction-decay signal, which requires measurements with high signal-to-noise ratio.¹⁷³ The fitting routine is performed for each voxel and deoxygenated CBV and OEF can be obtained (Figure 1.16).¹⁷⁰ Improvements to the qBOLD method include its unification to a SBO approach,^{159,174} and the use of priors (i.e., venous CBV and $S_v\text{O}_2$).¹⁷⁵ Despite the results indicating the feasibility of qBOLD as a non-invasive alternative to $[^{15}\text{O}]\text{O}_2$ -PET, the approach is heavily dependent on accurate measurements and the inclusion of complex MR sequences to improve its accuracy might be a hindrance to clinical implementation.^{175,176}

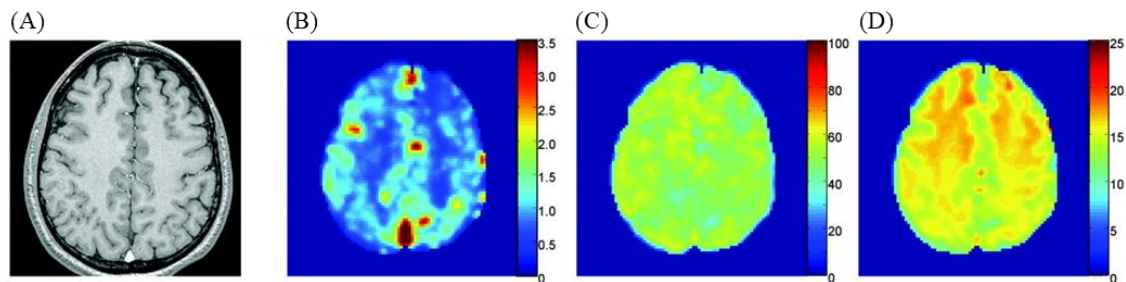


Figure 1.16. Resulting regional maps obtained with qBOLD. (A) Anatomical image presenting the brain slice for reference. (B) Deoxygenated CBV (in %), (C) OEF (in %), and (D) tissue R_2 (in s^{-1}) maps. This figure was reproduced from He & Yablonskiy (2007), *Magnetic Resonance in Medicine*,¹⁷⁰ with permission provided by John Wiley and Sons and Copyright Clearance Center.

Finally, calibrated BOLD experiments aim at estimating a calibration constant (M) that represents the maximum possible BOLD signal increase (i.e., due to completely deoxygenated blood) to obtain relative changes in CMRO_2 during activation,¹⁷⁷ either by implementing a hypercapnia or hyperoxia respiratory challenge.^{178,179} This is possible because the increase in BOLD signal during the respiratory challenge with respect to baseline is assumed isometabolic (i.e., CMRO_2 remains constant).¹⁷⁷ Changes in the fMRI signal are then modelled to estimate M by incorporating changes in CBF due to known physiological responses to hypercapnia and

hyperoxia. By combining both respiratory challenges, dual-calibrated BOLD experiments seek to unveil the baseline physiological state, i.e., obtaining baseline regional CMRO_2 (Figure 1.17).^{181–186} A more recent approach included SBO measurements to estimate the calibration constant, which has the potential to simplify dual-calibrated fMRI experiments.¹⁸⁶ One important limitation of calibrated BOLD is that the isometabolic assumption may not hold, which can overestimate the stimulus-induced changes in CMRO_2 .^{181,184} Further obstacles include subject discomfort due to hypercapnia, which can be particularly relevant for clinical populations, and the experimental design complexity.¹⁸⁰

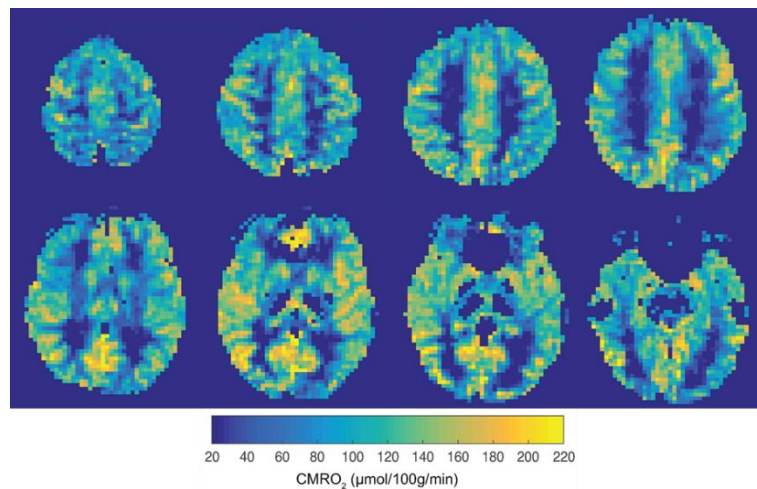


Figure 1.17. CMRO_2 map obtained with dual-calibrated fMRI. Here, a combination of hypercapnia and hyperoxia was implemented to estimate baseline CMRO_2 from changes in the BOLD signal. This figure was reproduced from Germuska & Wise (2019), *NeuroImage*,¹⁸⁰ with permission provided by Elsevier and Copyright Clearance Center.

1.6 Advantages of imaging cerebral metabolism with hybrid PET/MR

As PET has high sensitivity and specificity for imaging molecular targets, and complementary structural and functional MRI data can be acquired simultaneously, hybrid PET/MR imaging has the potential to amplify the range of neuroimaging applications. To this date, a range of review articles describing the challenges and advantages of hybrid PET/MR imaging have been published,^{187–190} including neuroimaging methodologies¹⁹¹ and applications.¹⁹² In this section, hybrid PET/MR imaging advantages are briefly described, specifically with respect to offering non-invasive and more accessible methods for imaging cerebral metabolism.

In some neurodegenerative diseases, such as Alzheimer's disease and frontotemporal dementia, hypoperfusion and hypometabolism precedes brain tissue loss,^{193,194} which indicates the need for implementing more accessible imaging tools to detect these changes in the early stages of the disease. Given the ubiquity of MRI scanners, MR techniques have the potential for significant clinical impact. Thus, hybrid PET/MRI has the unique ability to perform head-to-head comparisons between emerging MR methods and well-established PET measurements for imaging cerebral metabolism. For instance, recent studies showed that ASL can detect hypoperfusion in a range of neurodegenerative diseases¹⁹⁵ and has the potential to track longitudinal CBF changes in dementia.¹⁹ Comparison studies between ASL and [¹⁵O]H₂O PET are facilitated by implementing the non-invasive PET/MR method developed by Ssali *et al.*, in which WB CBF estimates from PC-MRI are used as reference for the [¹⁵O]H₂O-PET data.⁸⁸ Similarly, this thesis explores the possibility to use WB-CMRO₂ as a reference to calibrate [¹⁵O]O₂-PET data to image cerebral metabolism. Compared to the three-tracer PET method, this hybrid PET/MR technique only requires [¹⁵O]O₂ inhalation to image CMRO₂ since CBF imaging can be performed using ASL instead of [¹⁵O]H₂O PET. Furthermore, non-invasive MRI measurements of CBV¹⁹⁶ could improve these PET/MR approaches by including the blood vessel signal contributions.

Another related application of hybrid PET/MR imaging is to improve the acquisition of IDIFs, since MRI angiography enables more robust vessel segmentation.^{82,197} In contrast, stand-alone PET approaches typically require careful measurement of the point-spread-function of the scanner⁷⁵ or calibration factors obtained by acquiring a few blood samples¹⁹⁸ to correct for PVEs.^{76,77,81,95} However, these methods are sensitive to errors in the estimated correction factors and image registration. The latter can be reduced by using hybrid PET/MRI to collect anatomical MRIs for vessel segmentation in the same imaging session as [¹⁵O]H₂O and [¹⁵O]O₂ PET data. Alternatively, regional perfusion can be mapped by using WB CBF estimates from PC MRI to calibrate the IDIF extracted from the WB [¹⁵O]H₂O time-activity curve (TAC), as described in Chapter 4. Similarly, an analogous approach can be implemented to image CMRO₂, as explored in further details in the last chapter of this thesis.¹⁹⁹

1.7 Thesis outline

This thesis summarizes the work associated with developing new hybrid [^{15}O]-PET/MR techniques to reduce the invasiveness of the PET-alone approaches for measuring regional cerebral hemodynamics and metabolism, i.e., CBF, OEF and CMRO_2 .

1.7.1 Chapter 2: A non-invasive reference-based method for imaging the cerebral metabolic rate of oxygen by PET/MR: theory and error analysis

PET remains the gold standard for quantitative imaging of CMRO_2 ; however, it is an invasive and complex procedure that requires accounting for RW and the CBV. We propose a non-invasive reference-based technique for imaging CMRO_2 that was developed for PET/MRI with the goal of simplifying the PET procedure while maintaining its ability to quantify metabolism. The approach is to use WB measurements of OEF and CBF to calibrate [^{15}O] O_2 -PET data, thereby avoiding invasive arterial sampling and reducing the PET procedure to [^{15}O] O_2 inhalation only. Chapter 2 presents the theoretical framework, along with error analyses, sensitivity to PET noise and inaccuracies in input parameters, and initial assessment on PET data acquired from healthy participants.

1.7.2 Chapter 3: A non-invasive method for quantifying cerebral metabolic rate of oxygen by hybrid PET/MRI: validation in a porcine model

Chapter 3 describes the validation of the method described in Chapter 2, hereafter referred to as the PET/MR imaging of oxidative metabolism (PMROx) approach. PMROx was validated in an animal model by comparison to PET-alone measurements. Additionally, we investigated if the MRI-perfusion technique ASL could be used to further simplify PMROx by replacing [^{15}O] H_2O -PET, and if the PMROx was sensitive to anesthetics-induced changes in metabolism. For this, [^{15}O] H_2O and [^{15}O] O_2 PET data from juvenile pigs were acquired in a hybrid PET/MR scanner (3 T Siemens Biograph mMR), together with simultaneous functional MRI (OxFlow and ASL).

1.7.3 Chapter 4: Quantifying cerebral blood flow by a non-invasive PET/MR method of extracting the $[^{15}\text{O}]\text{H}_2\text{O}$ image-derived input function free of partial volume errors

Methods for imaging CBF by PET without invasive arterial sampling generally require extracting an IDIF from the carotid arteries. However, these methods are sensitive to PVEs due to the poor spatial resolution of PET, which is even worse for $[^{15}\text{O}]$ -tracers when compared to $[^{18}\text{F}]$ -tracers. Hybrid PET/MRI offers an alternative non-invasive approach by using MRI measurements of WB CBF to calibrate $[^{15}\text{O}]\text{H}_2\text{O}$ -PET data, hereafter referred to as PET/MR imaging of CBF (PMRFlow). Chapter 4 presents a PMRFlow method of obtaining the IDIF from the WB $[^{15}\text{O}]\text{H}_2\text{O}$ TAC. Its accuracy was assessed in a porcine model by comparison to PET-only CBF measurements, and regional CBF estimates were obtained from PET/MR data acquired from healthy individuals.

1.7.4 Conclusion and future work

Finally, a summary of significant findings is presented, alongside with the exploration of continuation studies, both in terms of the technical aspects of the approaches described in this thesis, as well as their possible implementation in neuroimaging studies.

Chapter 2

2 A non-invasive reference-based method for imaging the cerebral metabolic rate of oxygen by PET/MR: theory and error analysis

Narciso L, Ssali T, Iida H, et al. A non-invasive reference-based method for imaging the cerebral metabolic rate of oxygen by PET/MR: theory and error analysis. *Phys Med Biol* 2021; 66: 065009. © IOP Publishing. Reproduced with permission. All rights reserved.

2.1 Introduction

One of the first applications of PET was to measure $CMRO_2$ using [^{15}O]-labelled tracers,²⁰⁰ driven by the recognition of the brain's high energy demands and continual adjustments to CBF to ensure sufficient supply of oxygen and glucose.²⁰¹ A three-tracer method was developed using [^{15}O]oxygen to image the cerebral oxygen extraction fraction (OEF), [^{15}O]water to image CBF, and [^{15}O]carbon monoxide to correct for the activity originating from the CBV.⁹² In its autoradiographic form, this three-tracer method has been applied to many neurological diseases including cerebrovascular pathologies and neurodegenerative diseases.³⁰ However, quantitative imaging $CMRO_2$ is a complex procedure requiring stable cerebral physiology for fairly long durations (30 to 60 min) due to the use of multiple tracers. Arterial blood sampling is required to measure the AIF for each tracer, and plasma and red blood activity must be measured separately for [^{15}O]O₂ imaging to account for metabolically produced [^{15}O]H₂O.⁹⁶ Both RW and blood-borne activity can cause substantial errors in the OEF and $CMRO_2$ estimates.⁹² Delay and dispersion of the measured AIFs can also contribute to inaccurate measurements.⁷⁰⁻⁷³

In an effort to reduce the length and complexity of the three-tracer method, Ohta *et al.* proposed a single [^{15}O]O₂ inhalation approach in which the imaging duration is restricted to less than 3 min to avoid substantial signal contributions from RW.⁹¹ The limitation with this method is the short imaging times can lead to poor counting statistics, although it performs just as accurately as the steady-state approach.²⁰² Alternatively, Kudomi *et al.* proposed a rapid autoradiographic method based on sequential inhalation of [^{15}O]CO₂, [^{15}O]O₂, preceded by [^{15}O]CO.⁶⁹ In a more recent study, the total scan time was reduced to less than 10 min by introducing a novel approach for pixel-by-pixel calculation of four sets of kinetic parameters

of CMRO₂, CBF, and functional vascular volumes for [¹⁵O]H₂O and [¹⁵O]O₂, by means of a basis-function method in which the need for [¹⁵O]CO inhalation can be eliminated.¹¹⁴ Although separating the AIFs for the different [¹⁵O]tracers¹¹³ and correcting for RW can be incorporated into the mathematical model,⁹⁸ this method still requires arterial sampling for determining the whole blood AIF.

MRI techniques based on the oxygen-dependent magnetic property of hemoglobin—i.e., BOLD contrast—have been proposed for imaging CMRO₂.²⁰³ One approach is to combine estimates of local oxygen saturation obtained by qBOLD with CBF data from ASL.^{157,170,204} Alternatively, calibrated BOLD, which was originally developed to measure activation-induced changes in oxidative metabolism, has been extended to estimate absolute CMRO₂ by using multiple calibration stimuli.^{185,205,206} Despite the advantages of an MRI-only method (i.e., non-invasive and no ionizing radiation), these approaches only provide indirect measures of tissue oxygenation since the BOLD signal must be isolated from other factors that affect signal decay.¹⁸¹

This study presents a reference-based technique for imaging CMRO₂ that was developed specifically for hybrid PET/MRI to overcome some of the complexities associated with quantitative imaging of CMRO₂. The concept is to retain the fundamental advantage of [¹⁵O]O₂ PET in terms of directly measuring oxygen utilization, while incorporating complementary functional MRI techniques to provide a reference measurement for quantification. That is, WB CBF can be measured by PC MRI and S_vO₂ in the SSS measured by either susceptibility- or relaxation-based MRI oximetry—the combination of the two provides an estimate of WB CMRO₂.^{145,153,154} These MR methods are fast, easy to implement, and most importantly can be acquired while collecting [¹⁵O]O₂ PET data.¹⁵² The primary advantage of this hybrid imaging approach is it avoids invasive arterial blood sampling since WB CMRO₂ acts as a reference region. This is analogous to a previously published PET/MR approach for quantitative imaging of CBF by combining [¹⁵O]water PET imaging with phase-contrast MRI.⁸⁸ For imaging OEF and CMRO₂, a reference-region approach should also reduce the influence of RW and blood-borne activity, which are major sources of error with PET methods. Finally, the proposed approach retains the ability to quantify OEF and CMRO₂, in contrast to previously proposed semi-quantitative PET methods that result in relative measurements only.^{207,208}

In this study, we present the theoretical framework for the proposed reference-based technique, as well as error analyses conducted to investigate the effects of neglecting RW and CBV contributions and inaccuracies in input parameters. The sensitivity of the reference-based method to statistical noise in the WB and local $[^{15}\text{O}]\text{O}_2$ -PET TACs was also investigated. Finally, the feasibility of the reference-based method was evaluated by applying it to a human PET dataset consisting of $[^{15}\text{O}]\text{O}_2$, $[^{15}\text{O}]\text{H}_2\text{O}$ and $[^{15}\text{O}]\text{CO}$ images. While this analysis precluded evaluating the accuracy of WB CMRO_2 from MR oximetry, it did provide the opportunity to evaluate the accuracy of the reference-based theory for imaging regional CMRO_2 .

2.2 Theory

CMRO_2 is defined as the product of CBF (f), OEF (E) and the arterial content of oxygen ($C_a\text{O}_2$):

$$\text{CMRO}_2 = E \cdot f \cdot C_a\text{O}_2 \quad (2.1)$$

where $C_a\text{O}_2 = 1.34 \cdot Hb \cdot S_a\text{O}_2 + 0.003 \cdot P_a\text{O}_2$. Each gram of hemoglobin can transport 1.34 mL of oxygen and the blood has 3×10^{-3} mL of dissolved oxygen per unit of $P_a\text{O}_2$ per 100 ml of blood. $C_a\text{O}_2$ is determined by measuring the hemoglobin concentration, $P_a\text{O}_2$ and $S_a\text{O}_2$.

PET measurements of OEF are based on the one-tissue compartment model shown in Figure 1.8,⁵² in which the rate of change in activity concentration for a given brain tissue ($C_b^o(t)$; Eq. (2.2)) is defined by the influx rate constant of $[^{15}\text{O}]\text{O}_2$ (K_1^o) across the blood-brain barrier, the influx rate constant of metabolically generated $[^{15}\text{O}]\text{H}_2\text{O}$ (K_1^w), and the efflux rate constant of metabolically generated $[^{15}\text{O}]\text{H}_2\text{O}$ (k_2^w). A key assumption of the one-compartment model is that once $[^{15}\text{O}]\text{O}_2$ enters the brain it is immediately converted into $[^{15}\text{O}]\text{H}_2\text{O}$, and thus the efflux of $[^{15}\text{O}]\text{O}_2$ is negligible.⁹¹ The arterial activity concentration ($C_a^o(t)$) is given by the sum of the arterial activity concentration of $[^{15}\text{O}]\text{O}_2$ ($A_o(t)$) and RW ($A_w(t)$). The latter is generated by whole-body oxygen metabolism through the conversion of $[^{15}\text{O}]\text{O}_2$ to $[^{15}\text{O}]\text{H}_2\text{O}$.

$$\frac{d}{dt}C_b^o(t) = K_1^o \cdot A_o(t) + K_1^w \cdot A_w(t) - k_2^w \cdot C_b^o(t) \quad (2.2)$$

2.2.1 Simplified reference-based approach

The reference-based imaging method is based on a simplified version of the one-tissue compartment model in which the RW contribution is neglected (i.e., $K_1^w \cdot A_w(t) \cong 0$).⁹¹ The following differential equations are used to describe the time activity in the i^{th} brain region/voxel ($C_i(t)$) and the whole brain ($C_{wb}(t)$):

$$\frac{d}{dt} C_i^o(t) = E_i \cdot f_i \cdot A_o(t) - \frac{f_i}{\lambda} \cdot C_i^o(t) \quad (2.3)$$

$$\frac{d}{dt} C_{wb}^o(t) = E_{wb} \cdot f_{wb} \cdot A_o(t) - \frac{f_{wb}}{\lambda} \cdot C_{wb}^o(t) \quad (2.4)$$

In these equations, the influx rate constant for [¹⁵O]O₂ (K_1^o) is defined by $E \cdot f$ and efflux rate constant for metabolically generated [¹⁵O]H₂O (k_2^w) is f/λ , where λ is the partition coefficient of water. By considering $A_o(t)$ to be the same for both WB and the i^{th} brain region, the following expressions can be derived by integration:

$$\int_0^T \int_0^t A_o(u) du dt = \frac{\int_0^T C_{wb}^o(t) dt + \frac{f_{wb}}{\lambda} \int_0^T \int_0^t C_{wb}^o(u) du dt}{E_{wb} \cdot f_{wb}} \quad (2.5)$$

$$\int_0^T \int_0^t A_o(u) du dt = \frac{\int_0^T C_i^o(t) dt + \frac{f_i}{\lambda} \int_0^T \int_0^t C_i^o(u) du dt}{E_i \cdot f_i} \quad (2.6)$$

$$\frac{\int_0^T C_i^o(t) dt + \frac{f_i}{\lambda} \int_0^T \int_0^t C_i(u) du dt}{E_i \cdot f_i} = \frac{\int_0^T C_{wb}^o(t) dt + \frac{f_{wb}}{\lambda} \int_0^T \int_0^t C_{wb}^o(u) du dt}{E_{wb} \cdot f_{wb}} \quad (2.7)$$

Based on Eq. (2.1), CMRO₂ in i^{th} region can be defined by rearranging the terms:

$$CMRO_{2_i} = CMRO_{2_{wb}} \left[\frac{\int_0^T C_i^o(t) dt + \frac{f_i}{\lambda} \int_0^T \int_0^t C_i^o(s) ds dt}{\int_0^T C_{wb}^o(t) dt + \frac{f_{wb}}{\lambda} \int_0^T \int_0^t C_{wb}^o(s) ds dt} \right] \quad (2.8)$$

where T is the PET scan time. Unlike standalone PET methods, calibration to a reference region also makes this approach less sensitive to RW and blood-borne activity since the method is only dependent on signal changes relative to WB TAC.⁹¹

In a PET/MR experiment, the quantities f_i , f_{wb} and $CMRO_{2_{wb}}$ can be measured by MRI: f_i and f_{wb} by ASL, and $CMRO_{2_{wb}}$ by combining f_{wb} with an estimate of global venous oxygen saturation measured by MRI oximetry.¹⁵⁴

2.2.2 Residual functions

The magnitude of error in $CMRO_{2_i}$ caused by neglecting RW and blood-borne activity can be estimated by deriving versions of Eq. (2.8) that account for these signal contributions.

2.2.2.1 Recirculating water

The differential equations governing the time activity in brain tissue ($C_i^o(t)$; Eq. (2.2)) for both the i^{th} region and WB can be modified to account for the influx of $[^{15}\text{O}]\text{H}_2\text{O}$. Following the same approach outlined through Eqs. (2.5) to (2.7), the solution for $CMRO_{2_i}$ including the RW contribution is given by:

$$CMRO_{2_i} = CMRO_{2_{wb}} \left[\frac{\int_0^T C_i^o(t) dt + \frac{f_i}{\lambda} \int_0^T \int_0^t C_i^o(u) du dt}{\int_0^T C_{wb}^o(t) dt + \frac{f_{wb}}{\lambda} \int_0^T \int_0^t C_{wb}^o(u) du dt} \right] + \varepsilon_{RW} \quad (2.9)$$

where ε_{RW} is the RW residual function given by:

$$\varepsilon_{RW} = \frac{(E_i - E_{wb}) \cdot f_i \cdot f_{wb} \cdot C_a O_2}{\int_0^T C_{wb}^o(t) dt + \frac{f_{wb}}{\lambda} \int_0^T \int_0^t C_{wb}^o(u) du dt} \int_0^T \int_0^t A_w(u) du dt \quad (2.10)$$

2.2.2.2 Cerebral blood volume

The influence of blood-borne activity, which can cause significant overestimation of $CMRO_2$ in PET-only experiments,⁹³ can be accounted for by including vascular terms in the definition of the total measured activity:

$$C_{PET}(t) = (1 - CBV) \cdot C_b^o(t) + V_0 \cdot A_o(t) + V_A \cdot A_w(t) \quad (2.11)$$

where $V_0 \cdot A_o(t)$ accounts for $[^{15}\text{O}]\text{O}_2$ bound to hemoglobin and $V_A \cdot A_w(t)$ accounts for arterial $[^{15}\text{O}]\text{H}_2\text{O}$. V_A is the arterial blood volume, and $V_0 = R_{Hct}(1 - EF_v) \cdot CBV$; R_{Hct} is the small-to-large hematocrit ratio ($R_{Hct} = 0.85$)⁹⁴ and F_v the venous-to-total blood volume ratio ($F_v = 0.835$)⁹². The definition of V_0 reflects the fact that oxygen extraction primarily occurs at the capillary level.⁹² The expression for $CMRO_{2i}$ including additional residue terms to account for the $[^{15}\text{O}]\text{O}_2$ and $[^{15}\text{O}]\text{H}_2\text{O}$ vascular contributions is given by:

$$CMRO_{2i} = CMRO_{2wb} \left[\frac{\int_0^T C_i^o(t) dt + \frac{f_i}{\lambda} \int_0^T \int_0^t C_i^o(u) du dt}{\int_0^T C_{wb}^o(t) dt + \frac{f_{wb}}{\lambda} \int_0^T \int_0^t C_{wb}^o(u) du dt} \right] + \varepsilon_{V_0} + \varepsilon_{V_A} \quad (2.12)$$

$$\begin{aligned} \varepsilon_{V_0} = (1 - CBV_i) \frac{CMRO_{2i}}{\alpha_{wb}} & \left[\frac{CBV_i}{(1 - CBV_i)} \alpha_{wb} + V_{0wb} \cdot \beta_{wb} \right] \\ & - (1 - CBV_{wb}) \frac{CMRO_{2wb}}{\alpha_{wb}} \left[\frac{CBV_{wb}}{(1 - CBV_{wb})} \alpha_i + V_{0i} \cdot \beta_i \right] \end{aligned} \quad (2.13)$$

$$\begin{aligned} \varepsilon_{V_A} = (1 - CBV_i)(1 - CBV_{wb}) & \left[\varepsilon_{RW} + \frac{V_{Awb}}{1 - CBV_{wb}} \frac{CMRO_{2i}}{\alpha_{wb}} \delta_{wb} \right. \\ & \left. - \frac{V_{Ai}}{1 - CBV_i} \frac{CMRO_{2wb}}{\alpha_{wb}} \delta_i \right] \end{aligned} \quad (2.14)$$

where $\alpha = \int_0^T C_b^o(t) dt + \frac{f}{\lambda} \int_0^T \int_0^t C_b^o(u) du dt$, $\beta = \int_0^T A_o(t) dt + \frac{f}{\lambda} \int_0^T \int_0^t A_o(u) du dt$, and $\delta = \int_0^T A_w(t) dt + \frac{f}{\lambda} \int_0^T \int_0^t A_w(u) du dt$.

2.3 Materials and methods

2.3.1 Simulations

Simulations were conducted by generating theoretical versions of the total arterial input function, $C_a^o(t)$, and the recirculating water component, $A_w(t)$:^{65,98}

$$C_a^o(t) = \sum_{i=1}^2 a_i \cdot t \cdot e^{-\frac{t}{b_i}} \quad (2.15)$$

where $a_1 = 100$, $a_2 = 1.2$, $b_1 = 0.3$ and $b_2 = 3$. Using the model proposed by Kudomi *et al.*,⁹⁸ $A_w(t)$ was derived from the total arterial curve:

$$A_w(t + \Delta t) = k(\alpha_1 \cdot A_t(t) * e^{-\beta_1 t} + \alpha_2 \cdot A_t(t) * e^{-\beta_2 t}) \quad (2.16)$$

where Δt is the average delay of RW appearance for humans ($\Delta t = 20$ s),⁹⁶ and $\alpha_{1,2}$ and $\beta_{1,2}$ are defined by three compartmental rate constants, k , k_w and k_2 . Average values from human studies for k , k_w and k_2 were selected: 0.13, 0.38 and 0.29 min^{-1} , respectively.⁹⁸ The AIF for $[^{15}\text{O}]\text{O}_2$ was given by $A_o(t) = A_t(t) - A_w(t)$. Simulated arterial input functions are presented in Figure 2.1A. For illustration purposes, Figure 2.1B presents the corresponding simulated brain TACs generated for the three AIFs: $[^{15}\text{O}]\text{O}_2$ -only ($C_{O_2}(t)$, Eq. (2.3)), including RW ($C_{RW}(t)$, Eq. (2.2)), including V_0 ($C_{CBV}(t)$, Eq. (2.11)), and finally including RW, V_0 and V_A ($C_{PET}(t)$, Eq. (2.11)).

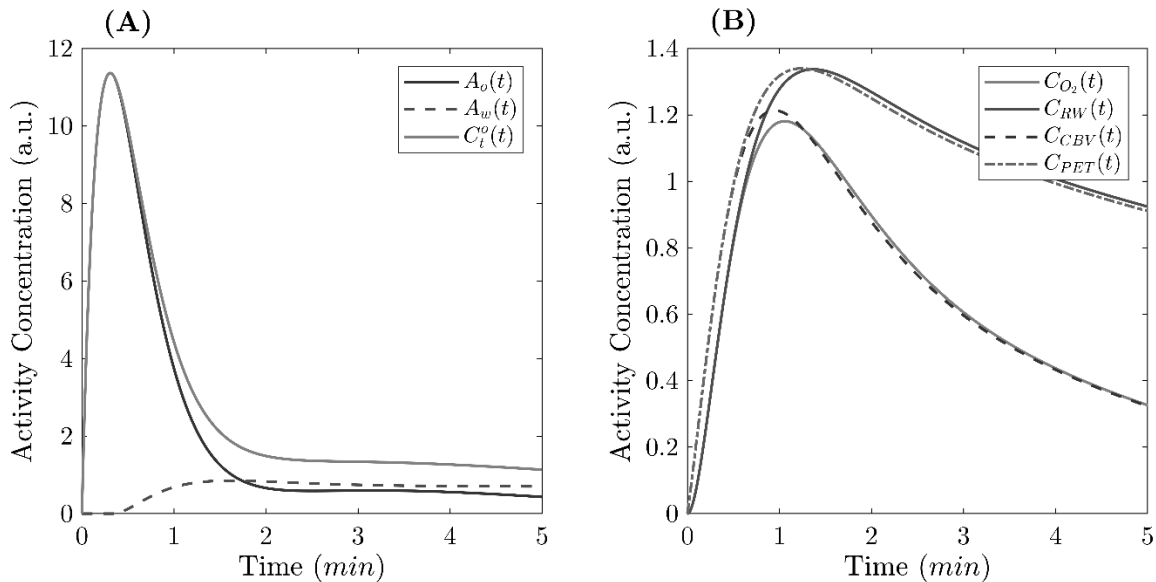


Figure 2.1. Theoretical input functions and tissue TACs. (A) Theoretical arterial input functions for $[^{15}\text{O}]\text{O}_2$ ($A_o(t)$, dark-grey line), metabolically generated $[^{15}\text{O}]\text{H}_2\text{O}$ ($A_w(t)$, dashed line), and their sum ($C_a^o(t)$, light-grey line). (B) Corresponding theoretical brain TACs for the three AIFs: $[^{15}\text{O}]\text{O}_2$ -only (solid light-grey line), RW (solid dark-grey line), CBV (V_0 , dashed dark-grey line), and both RW and CBV (V_0 and V_A , dash-dotted light-grey line). In all cases, CBF = 50 mL/100 g/min, $\lambda = 90$ mL/100 g, OEF = 0.40, CBV = 3.5 mL/100 g, and $V_A = 1.5$ mL/100 g.

2.3.1.1 Error analysis

The error analysis focused on differences in hemodynamic and metabolic parameters between a given brain region and the WB as the influences of RW and blood-borne activity are only dependent on relative differences (i.e., between local and WB parameters as given by Eqs. (2.10), (2.13) and (2.14)). The residue contributions from RW, Eq. (2.10), and blood-borne activity, Eqs. (2.13) and (2.14), were used to predict the magnitude of error in $CMRO_{2i}$ when estimated from the simplified solution, Eq. (2.8). Relative error, RE, was given by:

$$RE(\%) = 100 \frac{\widehat{CMRO}_{2i} - CMRO_{2i}}{CMRO_{2i}} = 100 \frac{-\varepsilon_i}{CMRO_{2i}} \quad (2.17)$$

where \widehat{CMRO}_{2i} and $CMRO_{2i}$ are the predicted and true values, respectively. For all simulations, WB-CBF and WB-OEF were fixed to 50 mL/100 g/min and 0.40, respectively. Likewise, local and WB $\lambda = 90$ mL/100 g, and WB-CBV = 3.5 mL/100 g and WB $V_A = 1.5$ mL/100 g. Changes in blood volume were modelled using the Grubb relationship: $CBV_i = CBV_{wb} (f_i / f_{wb})^{0.38}$.^{41,209} Finally, $CMRO_2$ was calculated using Eq. (2.1) with $C_aO_2 = 0.175$ mL O_2 /mL ($Hb = 13$ g/mL, $S_aO_2 = 98\%$ and $P_aO_2 = 90$ mmHg).

Simulations were performed for three possible scenarios. First, assuming that OEF was uniform across the brain, as expected at rest in the healthy brain (i.e. $E_i = E_{wb} = 0.4$). The residues were calculated over a range of regional CBF (i.e., f_i from 20 to 90 mL/100 g/min) and for integration time (T) ranging from 2 to 5 min. Next, E_i was varied by $\pm 25\%$ of WB-OEF (i.e., from 0.30 to 0.50), while constraining the corresponding f_i using the relationship: $E_i = 1 - e^{-PS/f_i}$. PS is the permeability-surface product for oxygen, which was fixed to 25 mL/100 g/min based on normal values of OEF and CBF of 0.40 and 50 mL/100 g/min, respectively. Again, simulations were performed for values of T ranging from 2 to 5 min.

The final set of simulations were performed by assuming a linear relationship between a change in regional CBF (Δf_i) and the corresponding change in $CMRO_2$ ($\Delta CMRO_{2i}$):

$$n = \left(\frac{\Delta f_i}{f_{wb}} \right) \left(\frac{\Delta CMRO_{2i}}{CMRO_{2wb}} \right)^{-1} \quad (2.18)$$

Values of n equal to 1.3, 2 and 3 were considered in these simulations with a fixed integration time of 5 min.^{210–212}

2.3.1.2 Errors in the input parameters

The impact of errors in the input parameter f_i on local $CMRO_2$ was evaluated by generating simulated TACs for local CBF values of 20, 40, 60 and 80 mL/100 g/min with whole-brain CBF fixed to 50 mL/100 g/min. These TACs were subsequently analyzed using Eq. (2.8) with incorrect values of f_i ranging from $\pm 20\%$. Given a PET/MRI experiment, these simulations are related to errors in the MRI measurements of local CBF. Note, a similar error analysis was not conducted for the other two input parameters, namely f_{wb} and E_{wb} , since any error in either parameter will have an equivalent effect on both local and WB $CMRO_2$.

2.3.1.3 Noise contributions

Simulations were conducted to evaluate how noisy TACs impact the precision and accuracy of $CMRO_{2i}$ estimates. Simulated TACs ($C_{O_2}(t)$) were generated using Eq. (2.3) with Gaussian noise added to each time point as $C_{noisy}(t) = C_{O_2}(t) \cdot [1 + CV \cdot G(0,1)]$, where CV is the coefficient of variation and $G(0,1)$ is a randomly generated number based on a Gaussian distribution of zero mean and standard deviation (SD) of one.^{213,214} Since the magnitude of noise will be greater for local TACs, the CV for the WB-TAC was fixed to 2%. This was based on comparing simulated noisy TACs to actual PET data, which are described in the next section. Simulations were performed (i) for a range of flows from 10 to 100 mL/100 g/min, while local TACs were generated with CV of 10%; and (ii) for local TACs generated with CV ranging from 0 to 20%, while fixing true $CMRO_2$ to 3.5 mL O_2 /100 g/min ($f_i = f_{wb} = 50$ mL/100 g/min and $E_i = E_{wb} = 0.40$). The former was performed to evaluate how local $CMRO_2$ is affected by the noise, while the latter to investigate the error in local $CMRO_2$ for different levels of noise in the local TACs. Simulations were repeated twenty thousand times to obtain a distribution of $CMRO_2$ estimates.

2.3.2 Application of the reference-based approach to [^{15}O]-PET data

To demonstrate the feasibility of the reference-based method, it was applied to a dataset of [^{15}O]-PET images. This analysis required using WB- $CMRO_2$ estimates from PET instead of from MR oximetry. Consequently, the accuracy of MR oximetry could not be evaluated;

however, the accuracy of regional CMRO_2 derived from Eq. (2.8) was evaluated by comparison to CMRO_2 images obtained from the DARG technique.⁶⁹

Retrospective data from healthy volunteers ($n = 10$, 23.2 ± 1.3 years, 64.3 ± 5.3 kg, 1 female) were acquired at the National Cerebral and Cardiovascular Center (Osaka, Japan; ethics approval M22-089-2). The imaging protocol used to generate the CMRO_2 , CBF and OEF images from the DARG technique is described elsewhere.¹¹⁴ Briefly, $[^{15}\text{O}]\text{H}_2\text{O}$ and $[^{15}\text{O}]\text{O}_2$ PET images were acquired with an ECAT-47 scanner (Siemens-CTI; 2D mode). Sequential $[^{15}\text{O}]\text{O}_2$ inhalation and $[^{15}\text{O}]\text{H}_2\text{O}$ injection lasted 8.5 min (~ 5 min $[^{15}\text{O}]\text{O}_2$ acquisition), while arterial blood was collected continuously with an AIF monitoring system.²¹⁵ A preceding $[^{15}\text{O}]\text{CO}$ acquisition was used to correct for CBV. AIFs were delay and dispersion corrected, and RW was modeled by the method described by Kudomi *et al.*⁹⁸ Images of OEF obtained from $[^{15}\text{O}]\text{O}_2$ PET data included corrections for RW and CBV contributions.⁶⁹

Reference-based CMRO_2 images were generated from the TAC data by applying Eq. (2.8) using an in-house MATLAB (2017b) script for integration times of 2, 3, 4, and 5 min. This analysis incorporated the CBF images acquired with $[^{15}\text{O}]\text{H}_2\text{O}$ and WB CMRO_2 was calculated from GM and WM regions defined by segmenting T_1 -weighted MRI images after removal of cerebrospinal voxels (SPM v.12, www.fil.ion.ucl.ac.uk/spm; 80% threshold).

All CMRO_2 images from the DARG and reference-based approaches were normalized to the MNI space. To compare the CMRO_2 images from the two methods, mean values were extracted for GM and WM regions, as well as volumes-of-interest (VOIs) for frontal, occipital and temporal lobes, insula, hippocampus, precuneus, dorsal striatum and cerebellum. Correlation was evaluated in terms of the Pearson correlation coefficient (ρ). Statistical tests were performed using SPSS Statistics (v. 26, International Business Machines Corporation, <https://www.ibm.com/analytics/spss-statistics-software>).

2.4 Results

Figure 2.2A shows the predicted error in regional CMRO_2 under the case of uniform OEF across the brain. In this scenario, the error is entirely due to regional variations in CBV (Eqs. (2.13) and (2.14)) since the influence of RW is the same throughout the brain when $E_i = E_{wb}$ (see Eq. (2.10)). Figure 2.2C-D show the predicted error in CMRO_2 when regional

OEF was constrained to be inversely proportional to CBF. In this case, the error in $CMRO_2$ as a function of E_i is presented for RW and CBV separately. The values of E_i and $CMRO_{2_i}$ for a given f_i are shown in Figure 2.2B. Next, Figure 2.3B shows the results of the simulations in which the value of E_i was defined by Eq. (2.18) (Figure 2.3A); both RW and CBV were included and the integration time was fixed to 5 min.

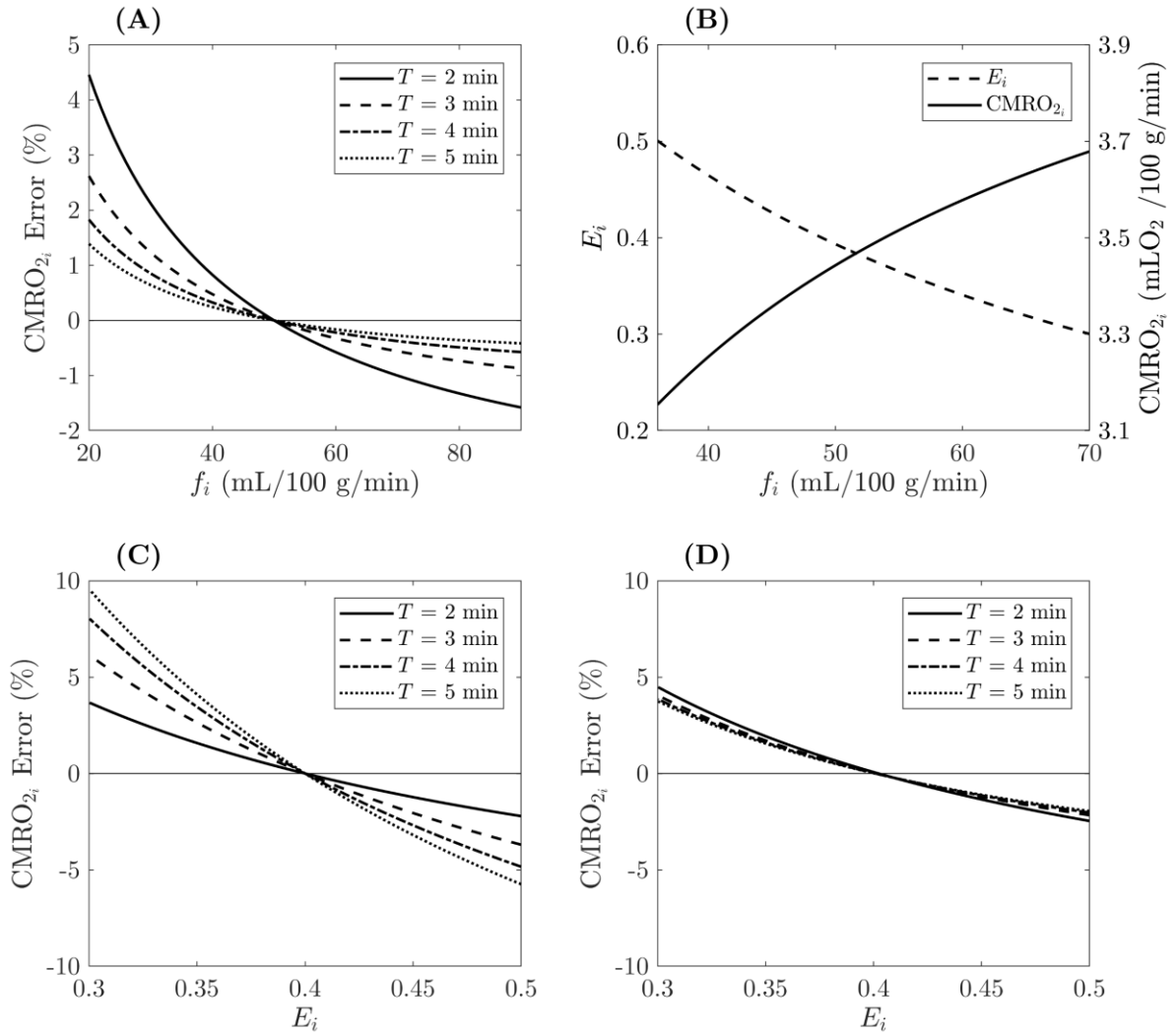


Figure 2.2. Simulations results: error in $CMRO_2$ for neglecting RW and CBV. (A) Predicted error in local $CMRO_2$ from the reference-based approach as a function of local CBF when OEF is uniform across the brain. Simulations were generated for a fixed local OEF of 0.40 and for different acquisition times (T) ranging from 2 to 5 min. (B) Relationship between local CBF, OEF and $CMRO_2$ when $E_i = 1 - e^{-PS/f_i}$. Corresponding error in $CMRO_2$ as a function of E_i is shown for neglecting (C) RW and (D) CBV. These errors were calculated using the residue functions given by Eqs. (2.10), (2.13) and (2.14). WB values of CBF, OEF, CBV, and V_A were fixed to 50 mL/100 g/min, 0.40, 3.5 mL/100 g, and 1.5 mL/100 g, respectively. Changes in blood volume were modelled using the Grubb relationship: $CBV_i = CBV_{wb}(f_i/f_{wb})^{0.38}$.

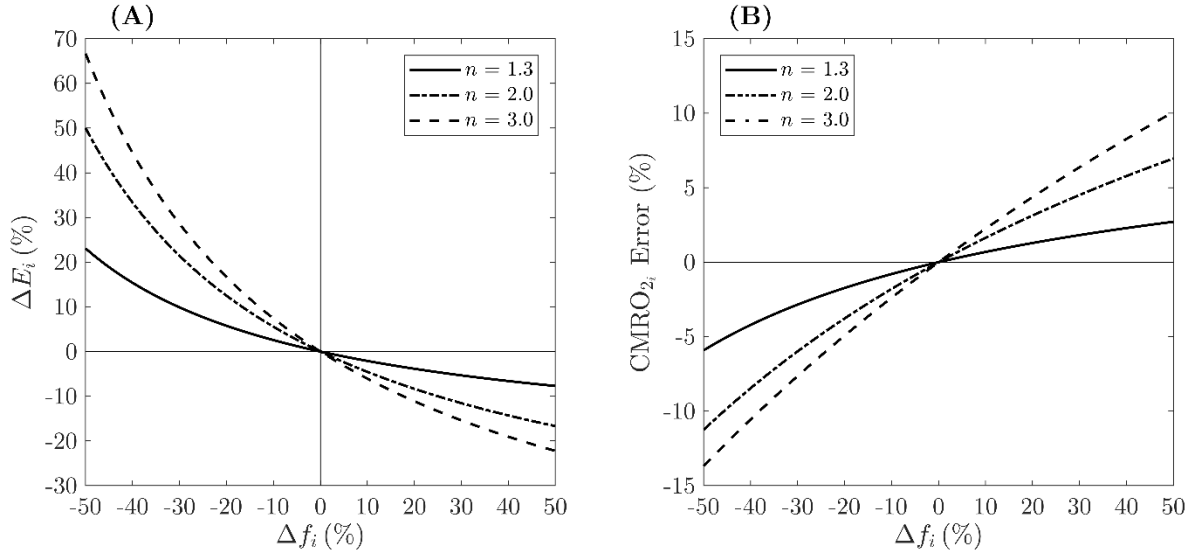


Figure 2.3. Simulations results: error in CMRO₂ for changes in CBF. (A) Relative change in OEF (ΔE_i) as a function of changes in CBF (Δf_i) for different values of n (1.3, 2 and 3), which defines the relationship between Δf_i and the corresponding change in CMRO₂ (Eq. (2.18)). (B) Predicted error in CMRO₂ for changes in CBF from -50 to 50%. For all simulations: (i) Local CMRO₂ was determined by the reference-based approach (Eq. (2.8)) and error obtained by residue functions (Eqs. (2.10), (2.13) and (2.14)) with a 5 min integration; (ii) WB values of CBF, OEF, CBV, and V_A were fixed to 50 mL/100 g/min, 0.40, 3.5 mL/100 g, and 1.5 mL/100 g, respectively; and (iii) Changes in blood volume were modelled using the Grubb relationship: $CBV_i = CBV_{wb}(f_i/f_{wb})^{0.38}$.

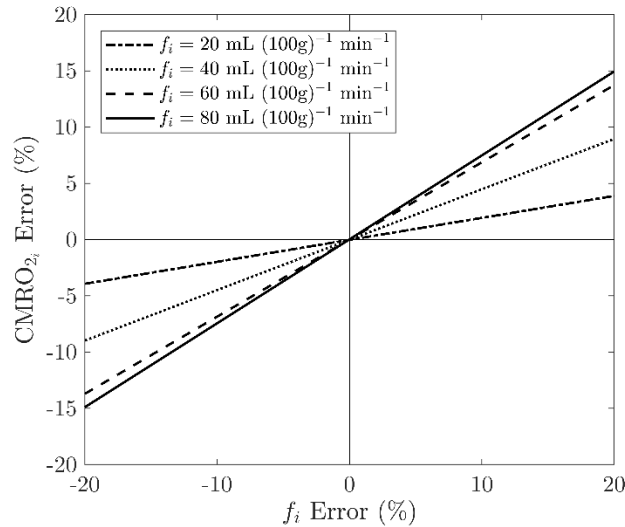


Figure 2.4. Simulations results: error in CMRO₂ due to inaccuracies in local CBF. Error in the estimated CMRO₂ due to incorrectly measuring local CBF (f_i). Simulations were conducted for f_i values ranging from 20 to 80 mL/100 g/min. For all simulations: (i) Local CMRO₂ was determined by the reference-based approach (Eq. (2.8)) and error obtained by residue functions (Eqs. (2.10), (2.13) and (2.14)), with a 5 min integration; (ii) WB values of CBF, OEF, CBV, and V_A were fixed to 50 mL/100 g/min, 0.40, 3.5 mL/100 g, and 1.5 mL/100 g, respectively; and (iii) Changes in blood volume were modelled using the Grubb relationship: $CBV_i = CBV_{wb}(f_i/f_{wb})^{0.38}$.

In terms of errors in the input parameters, Figure 2.4 presents the predicted error in CMRO_2 when regional CBF was varied by $\pm 20\%$ from its true value. The results for the different f_i values demonstrated that the error in CMRO_2 increased with CBF, which was expected given that f_i is a scaler in the numerator of Eq. (2.8).

The Monte Carlo simulations of noisy TACs indicated no bias in the CMRO_2 estimates across the different noise levels. Figure 2.5A shows the predicted versus true CMRO_2 estimates when WB and local CV were 2% and 10%, respectively. Figure 2.5B presents the error in CMRO_2 as a function of local CV. These results indicate that relatively small errors in the CMRO_2 estimates from the reference-based method (i.e., SD of $\pm 1\%$) are expected for TAC noise levels up to a CV of 20%.

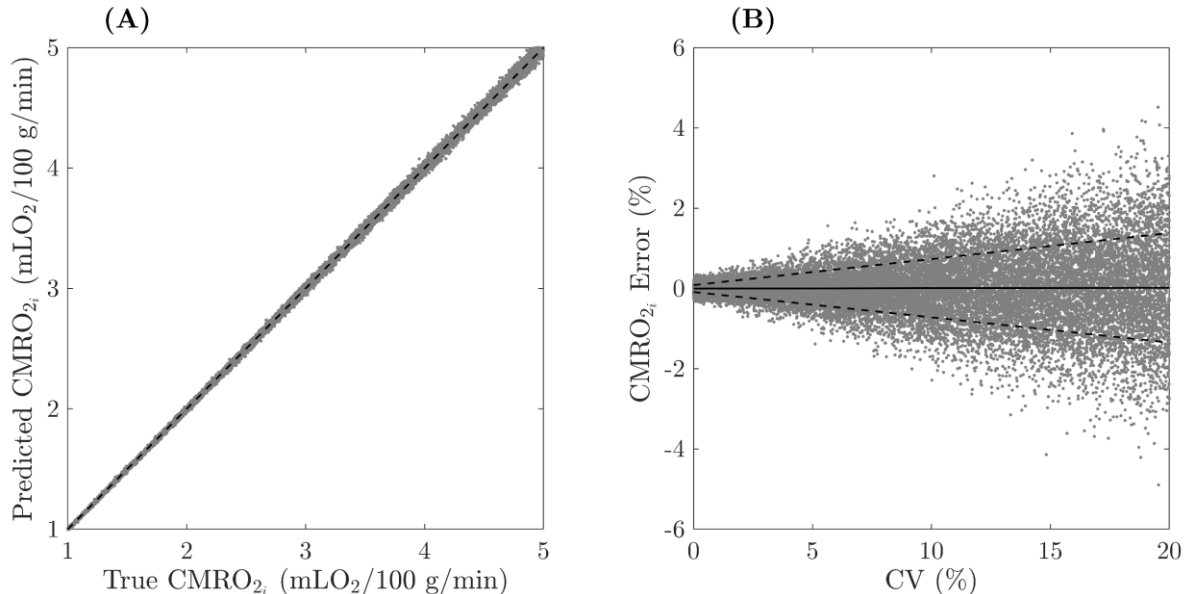


Figure 2.5. Simulations results: error in CMRO_2 due to noise. (A) Predicted versus true CMRO_2 after noise was added to WB (CV of 2%) and local (CV of 10%) TACs. The dashed black line is the identity line. (B) Error in CMRO_2 estimates after adding noise to local TACs (ranging from 0 to 20%, WB-TAC CV of 2%). True CMRO_2 was 3.5 mL O_2 /100 g/min ($f_i = f_{wb} = 50$ mL/100 g/min and $E_i = E_{wb} = 0.40$). Mean error is represented by the black solid line (± 1 SD, dashed black lines). For all simulations: (i) Local CMRO_2 was determined by the reference-based approach (Eq. (2.8)) and error obtained by residue functions (Eqs. (2.10), (2.13) and (2.14)), with a 5 min integration; (ii) WB values of CBF, OEF, CBV, and V_A were fixed to 50 mL/100 g/min, 0.40, 3.5 mL/100 g, and 1.5 mL/100 g, respectively; and (iii) Changes in blood volume were modelled using the Grubb relationship: $CBV_i = CBV_{wb}(f_i/f_{wb})^{0.38}$.

The reference-based method produced similar CMRO_2 images (Figure 2.6A-B; $T = 3$ and 5 min, respectively) compared to those obtained with the DARG method (Figure 2.6C). Mean CMRO_2 averaged across all brain voxels was 2.52 ± 0.85 mL O_2 /100 g/min for the

reference-based ($T = 5$ min) and 2.51 ± 0.87 mLO₂/100 g/min for the DARG method ($p = 0.02$). Figure 2.7A-B show OEF images from the reference-based approach ($T = 3$ and 5 min, respectively), while Figure 2.7C the DARG OEF images; OEF estimates were fairly uniform, as expected for the healthy brain. Voxel-wise average OEF was 0.39 ± 0.08 for the reference-based ($T = 5$ min) and 0.40 ± 0.09 for the DARG method ($p < 0.001$; 95% of the voxel-wise OEF values from the DARG technique were between 0.27 and 0.52). Figure 2.6D and Figure 2.7D present images of the relative CMRO₂ and OEF differences between the two methods, which were $1.7 \pm 14.5\%$ and $-1.3 \pm 11.7\%$ for GM and WM CMRO₂, respectively; and $-0.6 \pm 10.1\%$ and $-2.9 \pm 10.8\%$ for GM and WM OEF, respectively.

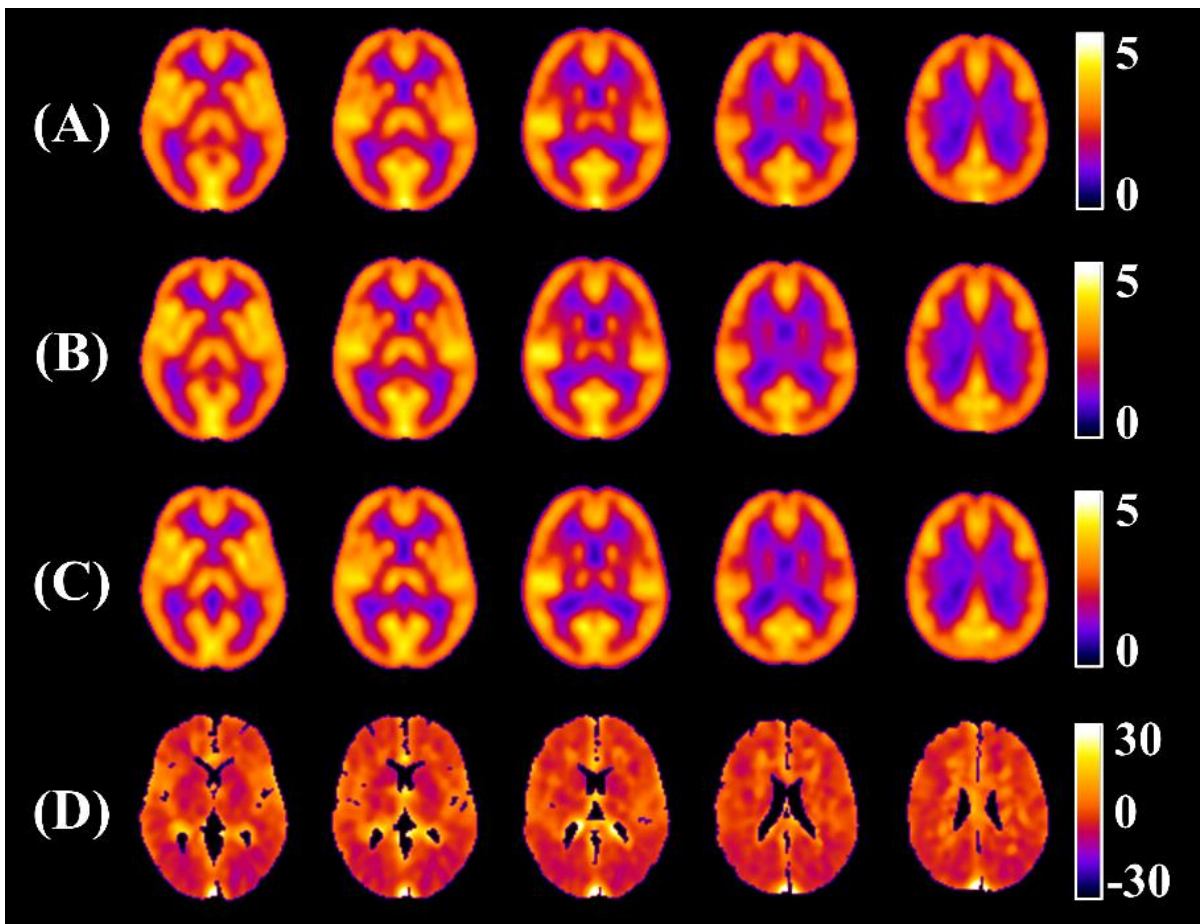


Figure 2.6. CMRO₂ images obtained with the reference-based method. CMRO₂ images (mLO₂/100 g/min) obtained with the reference-based method applied to [¹⁵O]₂-PET data from healthy volunteers ($n = 10$) for integration times of 3 (A) and 5 min (B), compared to DARG images (C). (D) Images of the relative difference (%) between the 5-min reference-based and DARG CMRO₂ images. Non-brain regions were removed by masking the corresponding anatomical T₁-weighted MR images. All images were normalized to the MNI space.

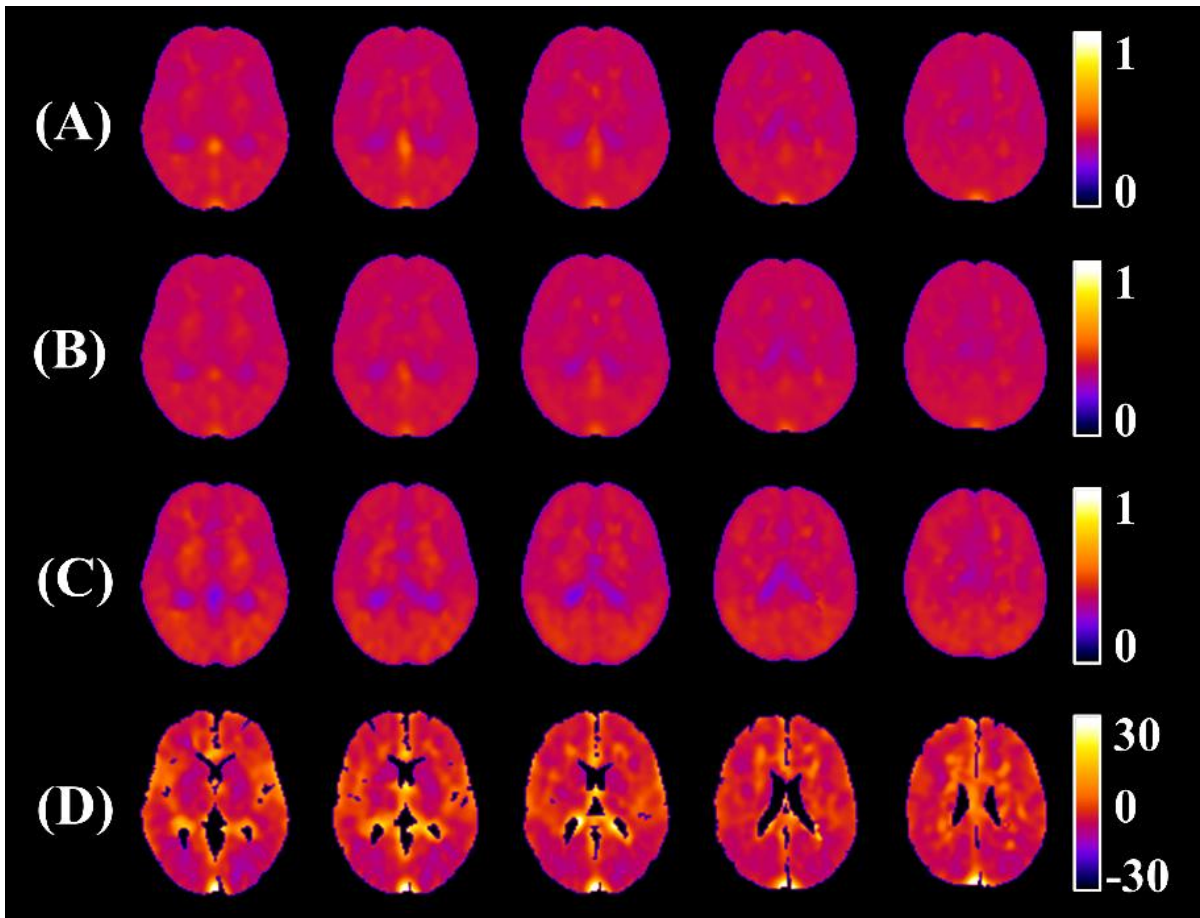


Figure 2.7. OEF images obtained with the reference-based method. OEF images obtained with the reference-based method for integration times of 3 (A) and 5 min (B), compared to DARG images (C). (D) Images of the relative difference (%) between the 5-min reference-based and DARG OEF images. Non-brain regions were removed by masking the corresponding anatomical T₁-weighted MR images. All images were normalized to the MNI space.

Significant correlation was found between regional CMRO₂ (Figure 2.8A) and OEF (Figure 2.8B) values from the reference-based and DARG methods for every VOI ($p < 0.001$; $R^2 > 0.98$; integration time of 5 min). Relative difference in CMRO₂ between the two methods plotted as a function of OEF is shown in Figure 2.8C. To generate this figure, each subject's OEF values were normalized to WB-OEF and scaled to a mean value of 0.40. Mean CMRO₂ differences between reference-based (5 min integration time) and DARG measurements were 0.05 mL O₂/100 g/min for GM (1.7% higher, $p < 0.01$) and -0.04 mL O₂/100 g/min for WM (1.3% lower, $p < 0.01$).

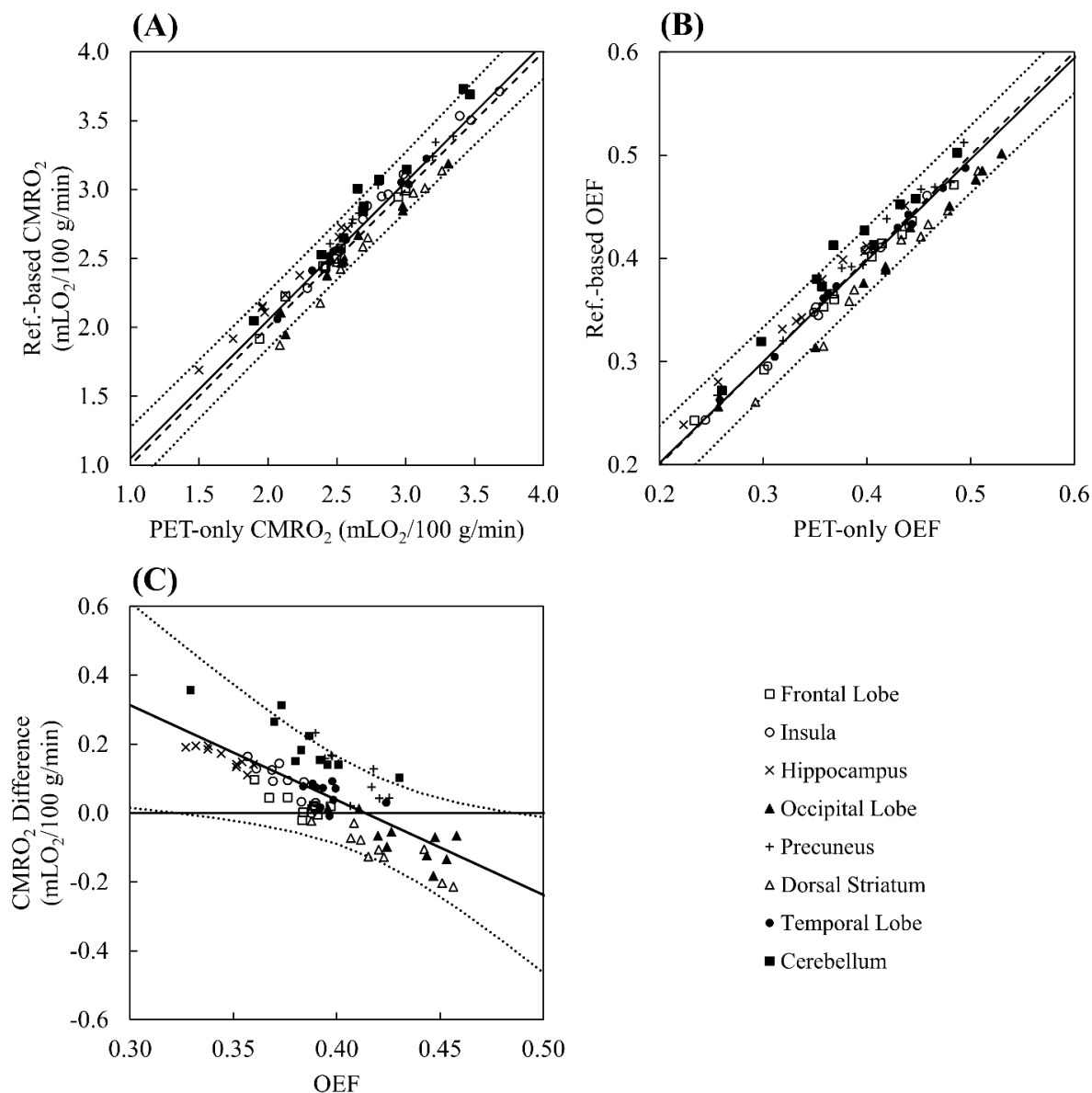


Figure 2.8. Comparison between reference-based and DARG methods. CMRO₂ (A) and OEF (B) estimates from DARG and reference-based methods ($n = 10$; integration time of 5 min). Selected VOIs were frontal, occipital and temporal lobes, insula, hippocampus, precuneus, dorsal striatum, and cerebellum. The dashed line represents the identity line, while the solid black line is the average regression (average slope of 1.00 ± 0.04 and 0.98 ± 0.04 for CMRO₂ and OEF, respectively; average intercept of 0.04 ± 0.14 mLO₂/100 g/min and 0.01 ± 0.02 for CMRO₂ and OEF, respectively; $R^2 > 0.98$; 95% CIs are represented by the dotted lines). Significant correlation ($p < 0.001$) was observed for all VOIs, for both CMRO₂ and OEF. (C) Relative difference in CMRO₂ for the two methods plotted as a function of OEF. Each subject's OEF values were normalized to the WB extraction and scaled to OEF = 0.40. The solid black line is the average regression ($y = -2.75x + 1.14$; $R^2 = 0.63 \pm 0.23$; 95% CIs are represented by the dotted lines).

2.5 Discussion

This study presents the derivation of a reference-based approach for imaging CMRO_2 developed to take advantage of simultaneous PET/MR imaging. The central concept is to use MRI to provide an independent estimate of WB CMRO_2 that can act as a reference in order to avoid invasive arterial sampling. The value of a reference region to simplify $[^{15}\text{O}]\text{-PET}$ imaging was investigated by Ibaraki *et al.*, although assumed values of WB CBF and OEF were required.²⁰⁷ Reference regions are also frequently used in PET studies of misery perfusion, although only to measure relative OEF.²⁰⁸ In addition to the model solution for the reference-based approach, this study also presents derivations of error terms that predict the effects of RW and blood-borne activity (i.e., CBV). The sensitivity of the method to errors in the input parameters and to statistical noise was investigated, the latter by Monte Carlo simulations; and an initial assessment of the approach was conducted using human PET data.

The value of the residual terms given in Eqs. (2.10), (2.13) and (2.14) is they indicate which factors will contribute to errors due to neglecting signal contributions from RW and CBV. Eq. (2.10) shows that the magnitude of RW errors is proportional to the difference between regional and WB OEF, while Eqs. (2.13) and (2.14) indicate that blood volume errors depend on regional differences in CBV and CMRO_2 . Since ε_{RW} depends on $A_w(t)$, its contribution will increase with integration time as the concentration of metabolically generated $[^{15}\text{O}]\text{H}_2\text{O}$ builds. The time dependency of the CBV error is not as straightforward as ε_{V_0} depends on $A_o(t)$ and ε_{V_A} on $A_w(t)$. These differences are illustrated in Figure 2.2 and Figure 2.3. When $E_i = E_{wb}$, the error is primarily due to ε_{V_0} , which is heavily weighted towards the first pass of radiolabelled oxygen. Consequently, its signal contribution diminishes with integration time, reaching a minimum of $\pm 1\%$ for $T = 5$ min (Figure 2.2A). When regional OEF differs from the WB value, ε_{RW} becomes the dominant residue and the error in regional CMRO_2 increases with integration time due to the greater contribution from RW. Figure 2.3 and Figure 2.4 predict that the magnitude of the error will vary by approximately $\pm 10\%$ when regional OEF varies from WB OEF by $\pm 25\%$ (i.e., $0.3 \leq E_i \leq 0.5$ when $E_{wb} = 0.4$) depending on the integration time. To put this in context, 95% of the voxel-wise OEF values from the PET dataset were within the range from 0.27 to 0.52 (Figure 2.7), which agrees with the general observation that OEF is fairly homogeneous in the healthy brain.^{114,202,216} The accuracy of the reference-based method is predicted to be worse for larger changes in regional OEF; for

example, ischemic stroke can lead to compensatory increases in OEF as large as 50%.²¹⁷ Figure 2.3 predicts an error of 15% for a 50% decrease in blood flow and a concomitant rise in OEF defined by $n = 3$; however, as the flow-to-metabolism ratio increases (i.e., $n \rightarrow \infty$), so will the error in CMRO_2 .

Shorter integration times would be the simplest approach for mitigating RW effects.⁹¹ An advantage of the reference-based method is that the procedure does not involve nonlinear optimization with multiple fitting parameters since CMRO_2 is determined directly from Eq. (2.8). Integration times less than 5 min are feasible considering the noise simulations demonstrated that CMRO_2 estimates had an error $\leq 2\%$ for TAC noise levels of up to 20% (Figure 2.5). Alternatively, the accuracy of the reference-based approach could be improved by including the RW residual term (Eq. (2.10)) into the model (Eq. (2.9)). The required AIF ($A_w(t)$) could be obtained with an IDIF approach.^{82,95} We are currently investigating this approach using the known WB CBF and OEF measurements to scale the IDIF derived from the measured WB [^{15}O]O₂-PET TAC.

As an initial investigation of the reference-based method, it was applied to an existing PET dataset. While this application cannot address potential issues with the MR techniques, it did provide the opportunity to evaluate the influences of RW and the CBV. Figure 2.6 and Figure 2.7 illustrate the similarity between CMRO_2 and OEF images generated from the reference-based approach for integration times of 3 and 5 min when compared to those from the previously validated DARG method. There were spatial differences, which are easier to identify in the difference images (Figure 2.6D and Figure 2.7D). The largest errors occurred near tissue boundaries, such as the ventricles, or coincided with large vessels, including the major cerebral arteries and the superior sagittal sinus. These artefacts are a consequence of neglecting CBV in the reference-based model; however, they represent less than 3% of the total number of voxels in the brain. Similar to the discussion regarding RW, a CBV correction could be applied by incorporating Eqs. (2.13) and (2.14) into the model (Eq. (2.12)). This correction would require measuring the oxygen AIF ($A_o(t)$) and imaging CBV. The former could be derived non-invasively by extracting an IDIF, while the latter could be performed either by [^{15}O]CO-PET²¹⁸ or by an MRI-based method.¹⁹⁶ Another approach that is currently under investigation is to estimate CBV by fitting Eq. (2.11) to [^{15}O]O₂-PET data using image-derived

estimates of $A_o(t)$ and $A_w(t)$. This correction would be valuable when CBV contributions could become more significant, such as in cerebrovascular diseases.

In terms of regional $CMRO_2$ and OEF, strong correlations ($p < 0.01$) were found between the two methods for all VOIs with an average regression slope of 1.00 ± 0.04 $mLO_2/100$ g/min for $CMRO_2$ and 0.98 ± 0.04 for OEF (Figure 2.8A-B). $CMRO_2$ exhibited a dependency on integration time for the reference-based method. For the four regions (frontal and temporal lobes, precuneus and dorsal striatum), the $CMRO_2$ estimate converged to the corresponding value from DARG as T increased from 2 to 5 min; while the opposite was observed in the other four VOIs. Based on the predictions of the residual terms, these patterns suggest the error was related to CBV for the first four VOIs and to RW for the remaining regions. To further investigate the agreement between the model predictions and the experimental results, the relative difference between the $CMRO_2$ estimates from the two methods was plotted as a function of OEF (integration time of 5 min; Figure 2.8C). The deviation between the two methods was significantly correlated with the difference between the OEF for a given VOI and the WB value ($\rho = -0.80$, $p < 0.001$). The magnitude of this difference as estimated from the regression analysis was similar to that predicted by the residuals (Figure 2.2).

In addition to [^{15}O]-related errors, the sensitivity of the $CMRO_2$ measurements to the input parameters was investigated. As evident by Eq. (2.8), inaccurate WB $CMRO_2$ measurements will have an equal effect on regional $CMRO_2$ estimates. The results presented in Figure 2.4 demonstrate that the approach also relies on accurately imaging CBF since the error in $CMRO_2$ is proportional to the error in the corresponding regional or voxel-wise CBF estimate. On a PET/MR scanner, non-invasive imaging of CBF with [^{15}O]H $_2$ O can be implemented by the approach recently proposed by Ssali *et al.*⁸⁸ Alternatively, the ability to acquire MR perfusion images simultaneously would reduce the PET procedure to just [^{15}O]O $_2$ inhalation, reducing the acquisition time to about five minutes. Since both MRI oximetry and ASL are non-invasive and rapid methods, repeat measurements can be easily acquired to improve precision.

In evaluating the potential sources of error with the proposed reference-based method, it is useful to compare it with other approaches developed to reduce the complexity of PET imaging of $CMRO_2$. These have included eliminating the need for measuring RW and CBV

directly through modelling approaches.^{91,96,98,114} However, they still require arterial sampling, which is technically complex, and the AIFs are inherently noisy. In an effort to circumvent this issue, newer methods have been developed based on measuring the IDIF, either by PET alone^{79,95} or by incorporating structural MRI for guidance.^{81,82} However, reliably extracting the IDIF is challenging due to the sensitivity to partial volume errors. Consequently, the accuracy of these methods relies on carefully measuring empirical scaling factors needed to quantify the IDIF.

2.6 Conclusions

This study presents an alternative approach that avoids the complications of measuring the input function altogether by calibrating the PET data with WB measurements, which can be accomplished by incorporating MRI measurements of OEF and CBF. When the method was applied to PET [¹⁵O]H₂O and [¹⁵O]O₂ data from healthy individuals, the strong agreement with results derived with the DARG approach demonstrated the feasibility of the reference-based method in this population. Further studies are required to validate the reference-based approach in a PET/MR scanner and to investigate its feasibility in clinical studies, especially when local OEF varies significantly from WB extraction.

Chapter 3

3 A non-invasive method for quantifying cerebral metabolic rate of oxygen by hybrid PET/MRI: validation in a porcine model

Narciso L, Ssali T, Liu L, et al. A Noninvasive Method for Quantifying Cerebral Metabolic Rate of Oxygen by Hybrid PET/MRI: Validation in a Porcine Model. *J Nucl Med* 2021; jnumed.120.260521. Copyright © 2021 by the Society of Nuclear Medicine and Molecular Imaging, Inc. Reproduced with permission. All rights reserved.

3.1 Introduction

Positron emission tomography imaging of cerebral oxidative metabolism was developed over thirty years ago and continues to prove a vital tool for understanding brain energetics and the role of altered metabolism in disease processes.^{9,30,35} PET remains the gold standard for imaging CMRO₂; however, the original procedure is complex and long.⁹² In addition to radiolabelled oxygen, [¹⁵O]H₂O is needed to measure CBF and [¹⁵O]CO to measure the CBV. Arterial blood sampling is required for each tracer, along with separating plasma and red blood cell activity for [¹⁵O]O₂ to account for the increasing signal contribution from metabolically generated [¹⁵O]H₂O (RW). Efforts to reduce its complexity and duration have led to modelling approaches that eliminate the need for separate CBV imaging and estimating RW without separating blood samples.⁶⁹ Alternately, the effects of RW can be minimized by short scan times following a single inhalation of [¹⁵O]O₂.⁹¹ More recently, approaches incorporating image-derived input functions have been proposed to avoid measuring the AIF, which is an invasive and inherently noisy procedure.^{82,95} However, the accuracy of these approaches depends on either an empirical factor relating the total AIF and its RW component, or careful measurement of a coefficient to scale the arterial TAC.

We propose an alternative method to reduce the complexity, invasiveness, and duration of CMRO₂ imaging.⁶⁸ Similar to Su *et al.*,⁸² this method takes advantage of simultaneous PET/MRI. However, rather than attempting to use MRI to help extract the AIF, the proposed hybrid approach incorporates complementary MRI techniques to measure WB CMRO₂ to serve as a reference to calibrate dynamic [¹⁵O]-oxygen PET data. Analogous to a similar PET/MR technique for imaging CBF,⁸⁸ this hybrid approach eliminates the need for arterial

sampling. Here, we implemented this reference-based approach, hereafter referred as PMROx (PET/MR imaging of oxidative metabolism), on a 3 T PET/MR scanner. The aim of this study is to validate PMROx in a large animal model by comparing to a previously validated DBFM.¹¹⁴ In addition, we investigated if PMROx could be further simplified by incorporating CBF images from the MRI-based technique ASL. This modification reduces PET imaging to only [¹⁵O]O₂ and imaging duration to approximately 5 min since the MRI sequences can be run during the PET acquisition.¹¹⁶ In addition to validating PMROx, its sensitivity to changes in metabolism was investigated by altering the anesthetics administered to the animals.

3.2 Materials and methods

Animal experiments were conducted according to the regulations of the Canadian Council of Animal Care and approved by the Animal Care Committee at Western University. Prior to imaging, juvenile Duroc pigs were tracheotomized, and catheters inserted into the cephalic veins and femoral arteries. During imaging, animals were mechanically ventilated, immobilized on a custom platform, and anesthetized with 3% isoflurane and 6 mL/kg/h propofol. Blood samples were collected to measure the partial pressures of oxygen and carbon dioxide, plasma glucose concentration, hematocrit, and hemoglobin concentration. Throughout the experiment, end-tidal O₂ and CO₂, temperature, heart rate, and oxygen saturation were monitored to ensure normal levels.

3.2.1 Study protocol

PET and MRI data were obtained on a 3 T Siemens Biograph mMR system using a 12-channel PET-compatible receiver head coil (Siemens GmbH). Each experiment was divided into two parts. First, the accuracy of PMROx was evaluated by comparing to the DBFM, which required measuring the AIFs of [¹⁵O]H₂O and [¹⁵O]O₂. Next, the sensitivity of PMROx to the expected reduction in cerebral metabolism was assessed by increasing the infusion rate of propofol to 20 mL/kg/h to induce a lower metabolic condition (LMC).

In both parts, PET imaging involved injecting [¹⁵O]H₂O to measure CBF, followed by inhalation of [¹⁵O]O₂ to measure OEF. Concurrently, WB CMRO₂ was obtained by the MRI-sequence OxFlow,¹⁵⁴ which combines phase-contrast MRI measurements of CBF from the internal carotid and basilar arteries, with venous oxygen saturation (S_vO₂) measurements from

the superior sagittal sinus acquired with susceptibility-based oximetry.¹⁵³ CBF images were collected using pseudo-continuous ASL (pCASL). At the end of experiment, the animal was euthanized according to the animal care guidelines and transported to a computed tomography (CT) scanner to obtain a post-mortem CT-based attenuation correction map.

3.2.2 PET imaging and postprocessing

The PET protocol (Figure 3.1) began with injecting [^{15}O]H $_2$ O (460 ± 80 MBq; cephalic vein), followed by inhaling 2,200 MBq of [^{15}O]O $_2$. All acquisitions involved 5 min of list-mode acquisition. For DBFM, AIFs from [^{15}O]H $_2$ O ($C_a^w(t)$) and [^{15}O]O $_2$ ($C_a^o(t)$) were determined by withdrawing blood from a femoral artery and measuring the activity using an MR-compatible system (Swisstrace GmbH). [^{15}O]O $_2$ -PET data acquisition during the LMC started approximately 1 hour after the first [^{15}O]O $_2$ acquisition to allow the animal to stabilize after changing the anaesthetics.

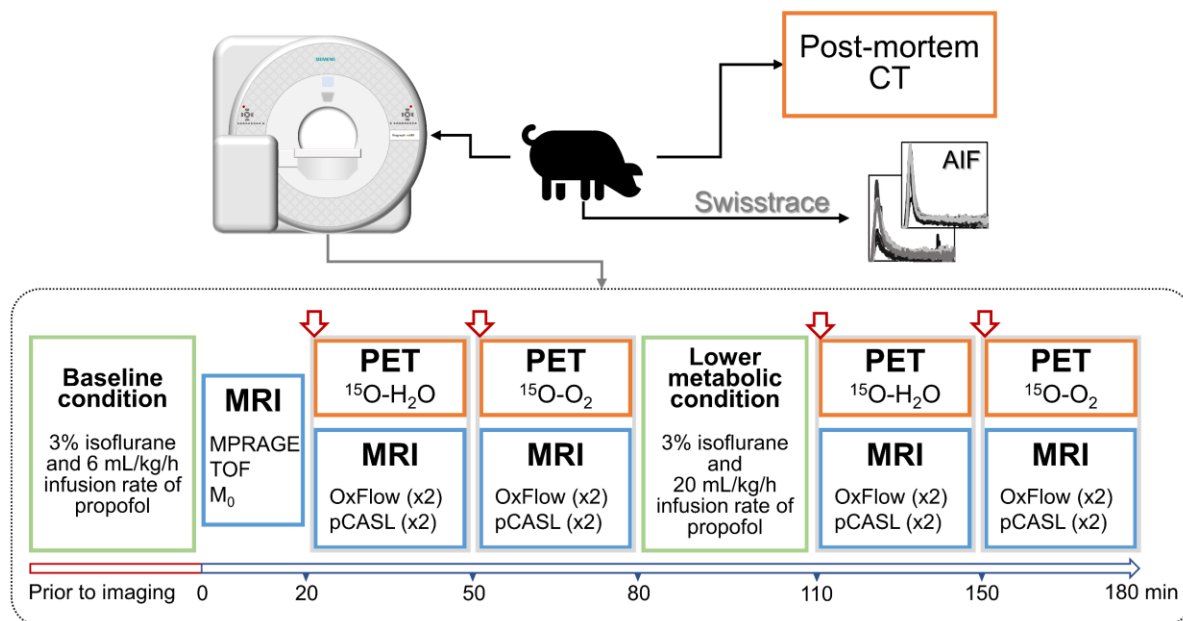


Figure 3.1. Protocol diagram. Protocol diagram showing the imaging blocks acquired at baseline and under the lower metabolic condition. Prior to imaging, the animal was positioned in the scanner and the anaesthetics was applied. At time zero, MR imaging was started, and the onsite cyclotron was contacted to produce the [^{15}O]H $_2$ O dose, which was injected at the 20 min mark. There was a delay of approximately 20 min prior to [^{15}O]O $_2$ delivery. Following the first [^{15}O]O $_2$ imaging block, the propofol infusion rate was increased to 20 mL/kg/h. The second [^{15}O]H $_2$ O run was performed at 110 min.

[^{15}O]H $_2$ O and [^{15}O]O $_2$ were produced by ^{14}N (d,n) ^{15}O reaction in an onsite cyclotron (PETtrace 800, 16.5 MeV; GE Healthcare).²¹⁹ For [^{15}O]O $_2$ imaging, the radioactive gas was filtered prior to being transferred to the PET/MR suite via a stainless-steel line (202-m long,

3-mm diameter). The line was connected to polyethylene tubing that directly fed into the inhalation tube of the animal (delivery rate of 1.5 L/min for 30 s). Expired gas was collected in a 200-L tank to hold it for seven half-lives.²²⁰

Dynamic PET images were reconstructed into 48 time-frames (30×3 s, 6×5 s, 6×10 s and 6×20 s) using the Siemens e7-tools suite with a 3D-ordered-subset expectation-optimization (OSEM) method (iterations/subsets, 4/21; matrix size, 344×344×127 voxels; field of view [FoV], 359×359×258 mm³; voxel size, 1×1×2 mm³; zoom factor, 2). Raw data were corrected for decay, random incidences, dead-time, detector normalization, data rebinning, and scatter. Absolute scatter correction was used for the [¹⁵O]O₂ images, as recommended for 3D scanning.²²¹ Reconstructed images were smoothed by a 4-mm Gaussian filter.

AIFs were decay corrected, and denoised using a wavelet signal denoising function (MATLAB R2017b, Block James-Stein method). The RW ($A_w(t)$) component of the measured [¹⁵O]O₂ AIF was estimated using species-specific values after interpolating to the differences in weight.⁹⁸

3.2.3 MR imaging and postprocessing

MR acquisition (Figure 3.2) began with T₁-weighted images (magnetization-prepared rapid gradient-echo sequence, MPRAGE; repetition/echo/inversion times [TR/TE/TI], 2,000/2.98/900 ms; flip angle [FA], 9°; FoV, 256×256 mm²; 176 slices; isotropic voxel size, 1 mm³), followed by time-of-flight images to identify the feeding arteries for phase-contrast imaging (TR/TE, 22/3.75 ms; FA, 18°; FoV, 200×181 mm²; 102 slices; voxel size, 0.3×0.3×1.5 mm³; 40 mm saturation band) and the sagittal sinus for oximetry imaging (no saturation band).

MR images acquired during PET acquisitions were OxFlow and pCASL. The former alternates between the two slice locations to measure WB CBF and S_vO₂ (TR/TE/ΔTE, 35/7.025/2.5 ms; FA, 25°; FoV, 208×208 mm²; voxel size, 1.6×1.6×5.0 mm³; velocity encoding [VENC], 60 cm/s; acquisition time, 1 min).¹⁵⁴ The acquisition of the OxFlow sequence was timed to coincide with the [¹⁵O]O₂ imaging and the resultant images represent an average over the 1-min scan to provide a stable reference measurement. Immediately following, a 3-dimensional pCASL sequence was run²²² (TR/TE, 3,720/22.9 ms; FoV, 208×208 mm²; 16 slices;

voxel size, $3.3 \times 3.3 \times 5.0 \text{ mm}^3$; post-labelling delay/labelling duration, 1500/1800 ms; label plane offset, 60 mm; 16 measurements). Lastly, proton density-weighted images were acquired by turning off the labelling or background suppression pulses (M_0 ; TR, 7,000 ms).

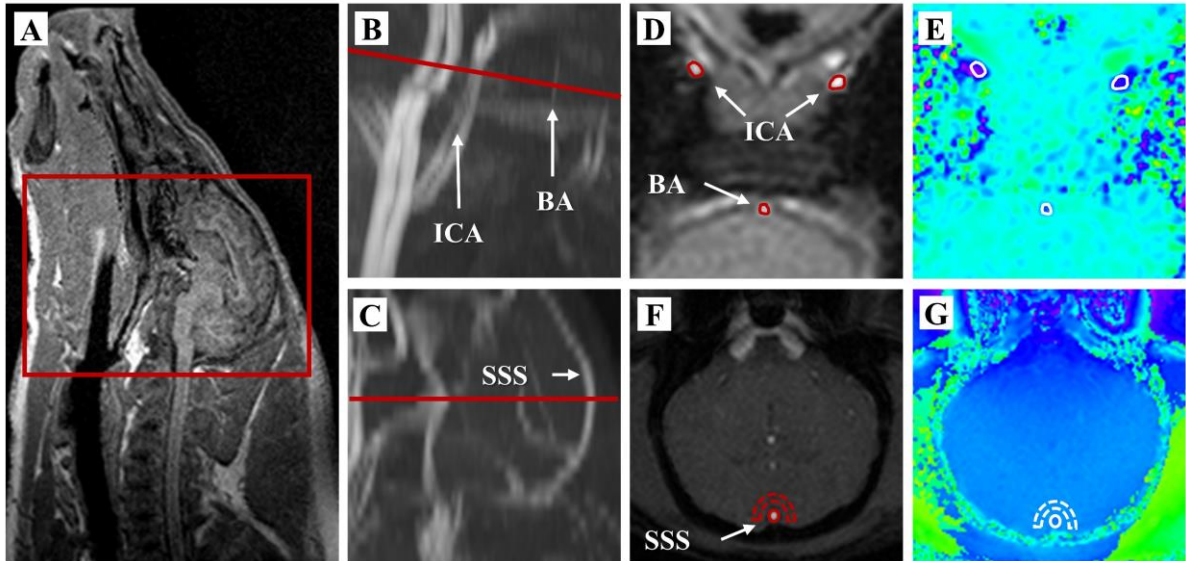


Figure 3.2. MR sequences acquisition and analysis scheme. (A) Sagittal MPRAGE image showing imaging region. MR angiography showing (B) the internal carotid arteries (ICA) and basilar artery (BA), and (C) the superior sagittal sinus (SSS). The red lines represent the slices used to measure WB CBF and S_vO_2 . Magnitude and phase images from the slices used to estimate (D)-(E) WB CBF and (F)-(G) S_vO_2 . The red regions-of-interest were transferred from the magnitude to the phase image (in white). All images are from one representative animal.

OxFlow images were analyzed following the approach outlined by Jain *et al.*¹⁵³ Briefly, regions-of-interest were semi-automatically drawn in and surrounding the vessels on the magnitude image, then transferred to the phase image to measure the mean phase difference in the feeding arteries, and between the sagittal sinus and the surrounding tissue. The pCASL images were motion corrected, coregistered to M_0 , and smoothed with a 4-mm Gaussian filter. CBF images were generated using the standard one-compartment model.¹¹⁶ For this analysis, the blood-brain partition coefficient of water was 0.90 mL/g, the longitudinal relaxation time of blood was 1.65 s, and the labelling efficiency was assumed to be 0.86. Images were coregistered to the PET space using SPM12 (<https://www.fil.ion.ucl.ac.uk/spm/>).

3.2.4 PET-only imaging: DBFM

CBF (f_i) maps were generated from $[^{15}\text{O}]\text{H}_2\text{O}$ -PET by fitting the following equation to the local TACs ($C_i(t)$):

$$C_i^w(t) = f_i \cdot C_a^w(t) * e^{-k_{2i}t} + V_{A_i} \cdot C_a^w(t) \quad (3.1)$$

where $*$ represents convolution. The fitting parameters were k_{2i} (clearance rate constant), f_i , and V_{A_i} (arterial blood volume). OEF (E_i) and $CMRO_2$ measurements were obtained by fitting [^{15}O]O₂ PET data to Eq. (3.2).¹¹⁴

$$C_i^o(t) = E_i \cdot f_i \cdot A_o(t) * e^{-k_{2i}t} + f_i \cdot A_w(t) * e^{-k_{2i}t} + V_{0_i} \cdot A_o(t) + V_{A_i} \cdot A_w(t) \quad (3.2)$$

where $A_o(t)$ is the [^{15}O]O₂ component of the AIF. The fitting parameters were E_i , V_{0_i} and V_{A_i} ([^{15}O]O₂ and [^{15}O]H₂O blood volumes, respectively). All fitting was performed in MATLAB using the optimization routine *fmincon*. $CMRO_2$ was calculated from Fick's principle as $CMRO_{2i} = E_i \cdot f_i \cdot C_aO_2$, where $C_aO_2 = 1.34 \cdot Hb \cdot S_aO_2 + 0.003 \cdot P_aO_2$, Hb is the hemoglobin concentration, and S_aO_2 (arterial saturation of oxygen) was estimated using the P_aO_2 (partial pressure of oxygen) measurements.¹⁵⁰

3.2.5 PMROx

PMROx $CMRO_2$ images were generated from [^{15}O]O₂-PET data using Eq. (3.3), which was derived from the one-tissue compartment model.⁶⁸

$$CMRO_{2i} = CMRO_{2wb} \left[\frac{\int_0^T C_i^o(t) dt + \frac{f_i}{p} \int_0^T \int_0^t C_i^o(u) du dt}{\int_0^T C_{wb}^o(t) dt + \frac{f_{wb}}{p} \int_0^T \int_0^t C_{wb}^o(u) du dt} \right] \quad (3.3)$$

where T is scan time. Local OEF was calculated by $E_i = CMRO_{2i} / (f_i \cdot C_aO_2)$. Both f_{wb} and $CMRO_{2wb}$ were obtained from OxFlow, the latter by:

$$CMRO_{2wb} = C_aO_2 \cdot f_{wb} \left(\frac{S_aO_2 - S_vO_2}{S_aO_2} \right) \quad (3.4)$$

CBF (Eq. (3.5)) was obtained using the noninvasive PET/MR approach described by Ssali *et al.*,⁸⁸ in which WB CBF is used to calibrate [^{15}O]H₂O-PET data. In both Eqs. (3.3) and

(3.5), WB CMRO₂, CBF, and TAC are used as scalers to obtain the corresponding local values. Alternatively for CBF, a direct scaling approach could be implemented.⁹⁰

$$f_i = f_{wb} \left[\frac{\int_0^T C_i^w(t) dt}{\int_0^T C_{wb}^w(t) dt + \frac{f_{wb}}{\lambda} \left(\int_0^T \int_0^t C_{wb}^w(u) du dt - \int_0^T \int_0^t C_i^w(u) du dt \right)} \right] \quad (3.5)$$

The feasibility of implementing pCASL into the PMRO_x approach (PMRO_{xASL}) was also evaluated. In this case, f_i in Eq. (3.3) was obtained from the CBF images generated by pCASL.

3.2.6 Regional CBF, OEF and CMRO₂ measurements

Volumes-of-interest (VOIs) were semi-automatically drawn on the MPRAGE images for each animal and then transferred to the corresponding CBF, OEF and CMRO₂ images. Measurements were made for cerebellum ($4.2 \pm 0.7 \text{ cm}^3$), diencephalon ($4.7 \pm 0.6 \text{ cm}^3$), and frontal ($2.4 \pm 0.6 \text{ cm}^3$), occipital ($7.9 \pm 1.5 \text{ cm}^3$), parietal ($9.1 \pm 1.6 \text{ cm}^3$) and temporal ($6.0 \pm 0.6 \text{ cm}^3$) lobes. All images were registered to the anatomical image of one animal to generate group-wise maps using SPM12 (<https://www.fil.ion.ucl.ac.uk/spm/>).

3.2.7 Statistics

Local measurements were compared using linear regression to obtain the Pearson correlation coefficient (ρ). Any potential bias was assessed using a one-sample t -test. Paired t -tests were performed to evaluate differences between measurements. Statistical significance was defined by $\alpha = 0.05$ and Bonferroni correction was performed when necessary. Measurements are expressed in terms of mean \pm standard deviation. Statistical tests were performed using SPSS (v. 26, International Business Machines Corporation, <https://www.ibm.com/analytics/spss-statistics-software>).

3.3 Results

Data from nine juvenile pigs were collected (age range 8-10 weeks; weight, $19 \pm 2 \text{ kg}$; 5 female). In one experiment, only [¹⁵O]H₂O data were acquired due to a technical issue with the [¹⁵O]oxygen line. The LMC was successfully induced in six animals. Table 3.1 provides a summary of arterial blood measurements during baseline and LMC.

Table 3.1. Summary of arterial blood measurements.

Measurement	Baseline	LMC
Hematocrit (%)	25.9 ± 3.4	25.7 ± 2.1
Hemoglobin (g/dL)	8.3 ± 1.1	8.3 ± 0.7
Partial pressure of oxygen (mmHg)	230 ± 100	239 ± 102
Partial pressure of carbon dioxide (mmHg)	40.3 ± 4.3	41.0 ± 3.4
S _a O ₂ (%)	99.5 ± 0.5	99.5 ± 0.4
Glucose concentration (mmol/L)	5.5 ± 0.8	5.5 ± 0.4

No statistical differences were identified in any of the parameters across the acquisitions.

AIFs could not be acquired in three cases (one [¹⁵O]H₂O and two [¹⁵O]O₂) due to clotting of the sampling line. In these cases, population-based AIFs were used after using a scaling factor for each animal individually. For the [¹⁵O]H₂O case, the AIF was scaled by the injected dose (MBq). Since the administered activity was unknown for [¹⁵O]O₂, the AIF was scaled to the mean jaw muscle activity (C_m) measured from a 50-mm² ROI. The appropriate scaling factor was determined by a combination of principal component and multiple linear regression analyses involving the remaining 6 measured AIFs. The factors included body weight (kg), endotracheal tube peak activity (kBq/mL), mean jaw muscle activity concentration (kBq/mL), and partial pressure of carbon dioxide (mmHg). The resulting model equation was subsequently used to scale the population-based AIF for each animal. Principal component analysis and multiple linear regression identified mean jaw muscle activity concentration (C_m) as significant component for estimating the scaling factor of [¹⁵O]O₂ ($= 43.5 \cdot C_m$; $R^2 = 0.998$). Figure 3.3 presents a comparison between [¹⁵O]O₂ measured AIFs with their respective scaled population-based curves; the blue curves represent the population-based AIFs used for the two animals that arterial sampling failed.

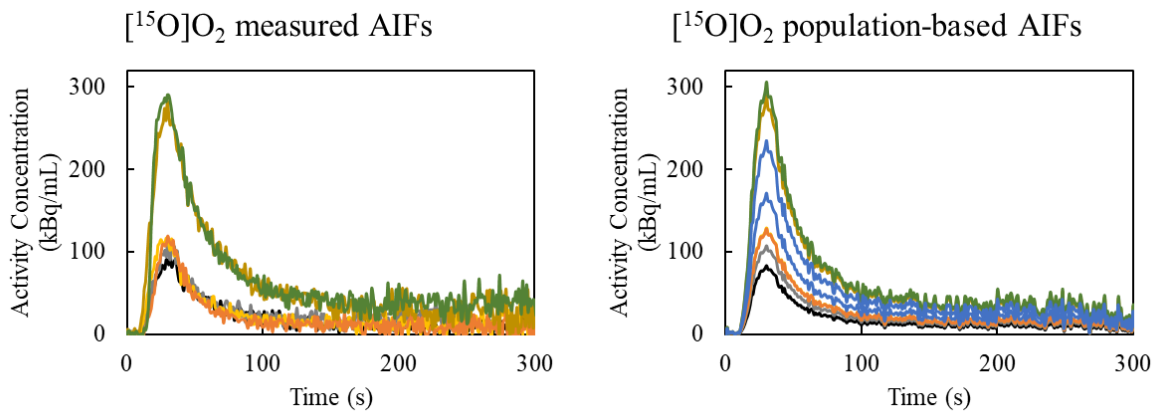


Figure 3.3. Measured versus population-based AIFs. Measured [¹⁵O]O₂ AIFs (left) and their respective scaled population-based curves (right). The blue curves represent the population-based AIFs used for the two animals that arterial sampling failed.

3.3.1 Validation

Average WB estimates of CBF, OEF and CMRO₂ from PET and PET/MR were in good agreement with no significant differences between techniques: 56.6 ± 21.0 mL/100 g/min, 0.31 ± 0.09 , and 1.81 ± 0.10 mL O₂/100 g/min from DBFM and 54.1 ± 16.7 mL/100 g/min, 0.30 ± 0.09 and 1.89 ± 0.16 mL O₂/100 g/min from OxFlow/PMROx, respectively. Average WB V_A from [¹⁵O]H₂O-PET was 9.5 ± 4.0 mL/100 g, and WB V_0 and V_A values from [¹⁵O]O₂-PET were 7.0 ± 1.0 mL/100 g and 2.6 ± 6.7 mL/100 g, respectively. WB [¹⁵O]O₂ V_A was small (< 2 mL/100 g) for 7 of 8 animals; however, in one outlier it was 19.1 mL/100 g.

Regional results of regression and correlation (Figure 3.4) analyses from CBF, OEF and CMRO₂ measurements are summarized in Table 3.2. Significant correlations between regional CBF estimates from noninvasive PET/MR and DBFM were observed in all VOIs. The Bland-Altman plot indicated a bias in local CBF measurements by noninvasive PET/MR for the parietal lobe (7.7 mL/100 g/min, $p = 0.02$) and diencephalon (14.8 mL/100 g/min, $p = 0.02$). Strong correlations between regional OEF estimates from PMROx and DBFM were observed (Figure 3.4B and Figure 3.5). Finally, regression between CMRO₂ estimates from the two techniques revealed good agreement with a moderate correlation and a small bias in the PMROx measurements for the cerebellum (0.16 mL O₂/100 g/min, $p = 0.03$) and diencephalon (0.30 mL O₂/100 g/min, $p < 0.01$).

Table 3.2. Summary of the regression and correlation analyses.

Technique	Measurement	Slope	Intercept	ρ
PMROx	CBF	0.98 ± 0.20	7.3 ± 9.8	0.91 ± 0.10
	OEF	$0.92 \pm 0.03^*$	$0.02 \pm 0.01^\dagger$	0.95 ± 0.04
	CMRO ₂	1.06 ± 0.35	-0.02 ± 0.63	0.67 ± 0.20
PMROx _{ASL}	CBF	0.85 ± 0.15	10.9 ± 11.7	0.80 ± 0.18
	OEF	$0.83 \pm 0.13^*$	$0.05 \pm 0.03^\dagger$	0.87 ± 0.09
	CMRO ₂	1.15 ± 0.41	-0.16 ± 0.70	0.53 ± 0.14

Summary of the regression and correlation analyses performed on the local baseline measurements ($n = 8$) of CBF (mL/100 g/min), OEF and CMRO₂ (mL O₂/100 g/min).

*Significantly different than one.

†Significantly different than zero.

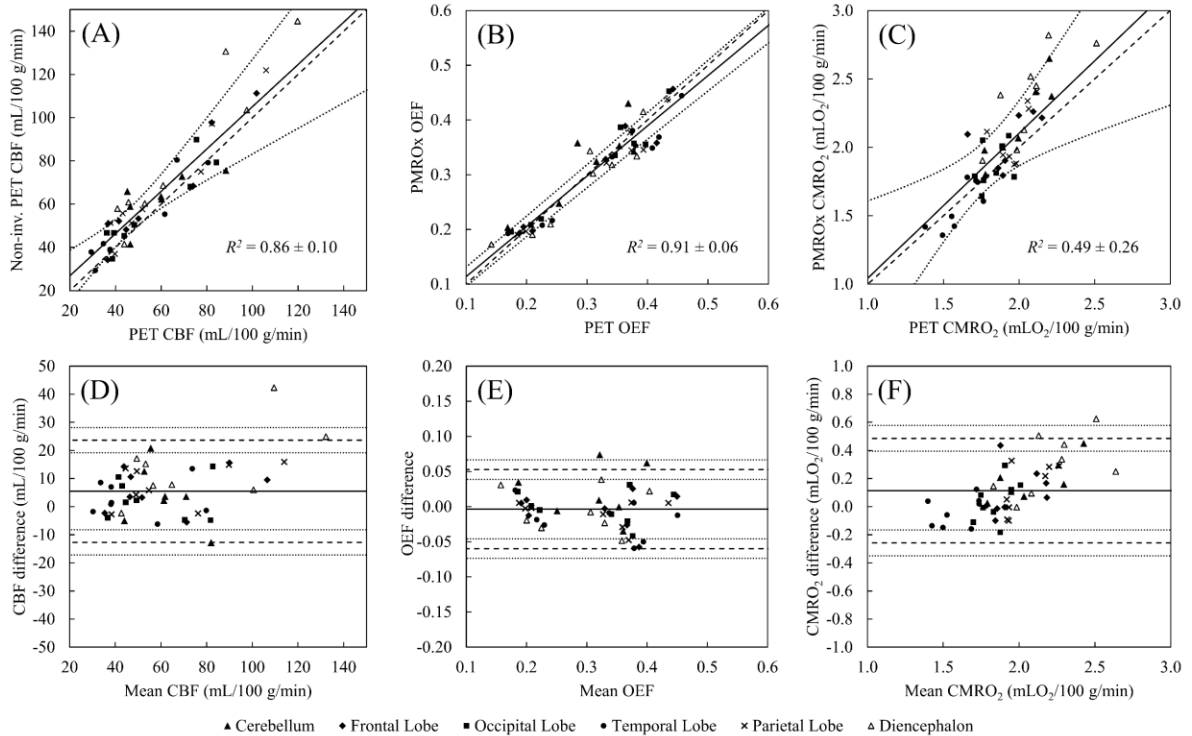


Figure 3.4. PMROx validation results. (A) Local baseline CBF from noninvasive PET/MR and DBFM. Average regression line is represented by the solid line ($y = 0.98x + 7.29$; 95% confidence interval (CI) is represented by the dotted lines). The dashed line is the identity line. Corresponding (B) OEF and (C) $CMRO_2$ results presented average regression line of $y = 0.92x + 0.02$ and $y = 1.06x - 0.02$, respectively. Bland-Altman plots from the corresponding data are presented in (D)-(F), where the mean is represented by the solid line. The dashed lines represent the limits of agreement (± 2 standard deviations), each with its 95% CI (dotted lines). Mean difference for all VOIs was 6.2 mL/100 g/min for CBF, -0.004 for OEF and 0.12 mL O_2 /100 g/min for $CMRO_2$.

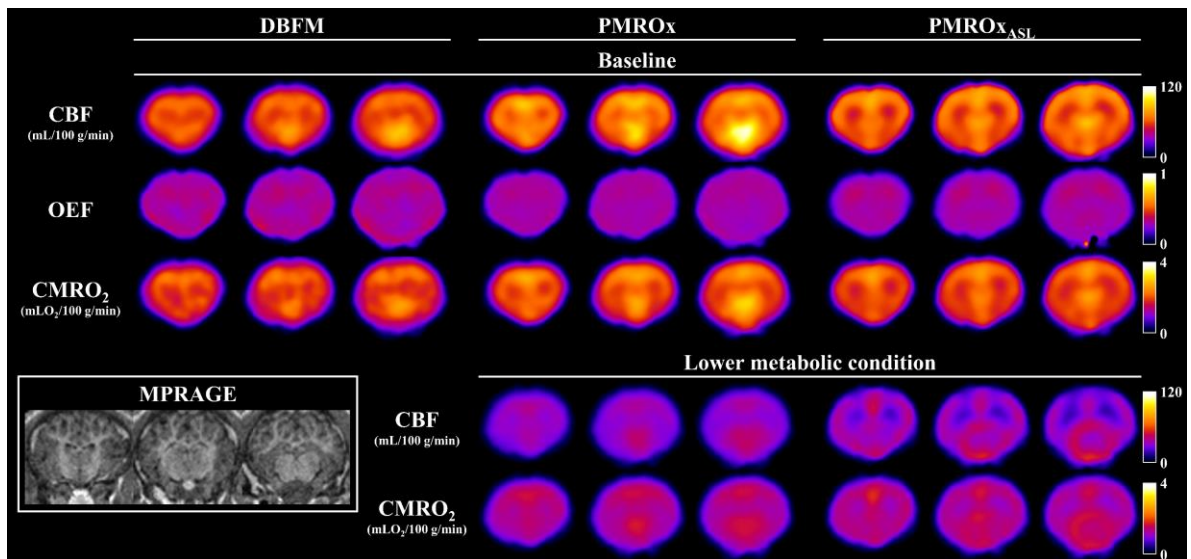


Figure 3.5. Group-wise CBF, OEF and $CMRO_2$ images. Group-wise CBF, OEF and $CMRO_2$ images obtained with DBFM, PMROx and PMROxASL techniques for baseline ($n = 8$, top three rows). CBF and $CMRO_2$ results from PMROx and PMROxASL for the lower metabolic condition ($n = 6$) are presented on the bottom two rows. MPRAGE from one animal was included for anatomical reference.

3.3.2 PMRO_{XASL}

Average WB estimates of CBF and CMRO₂ from pCASL and PMRO_{XASL} were 58.6 ± 20.4 mL/100 g/min and 1.88 ± 0.24 mL O₂/100 g/min, respectively, which were not significantly different from the PET-only results. Regional measurements were successfully extracted from all VOIs (Table 3.2, Figure 3.5 and Figure 3.6), except for the cerebellum from one animal because this region was missing in the pCASL FoV. Strong correlations between DBFM and pCASL CBF estimates were observed, as well as between DBFM and PMRO_{XASL} OEF estimates with a small bias in the temporal lobe (-0.048 , $p = 0.02$). CMRO₂ values from PMRO_{XASL} and DBFM showed a moderate correlation.

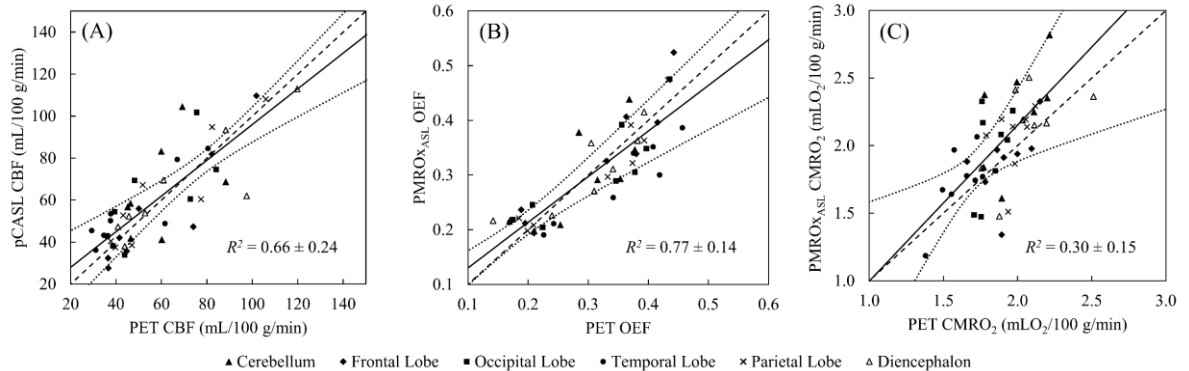


Figure 3.6. PMRO_{XASL} results. (A) Local baseline CBF from pCASL and DBFM. Average regression line is represented by the solid line ($y = 0.85x + 10.91$; 95% confidence interval is represented by the dotted lines). The dashed line is the identity line. Corresponding (B) OEF and (C) CMRO₂ results presented average regression line of $y = 0.83x + 0.05$ and $y = 1.15x - 0.16$, respectively.

3.3.3 Lower metabolic condition

For the six animals in which measurements were acquired under both conditions, propofol caused WB CBF to decrease to 27.3 ± 7.0 and 29.9 ± 6.4 mL/100 g/min for OxFlow and pCASL, respectively (50% reduction; Figure 3.5 and Figure 3.7A). There was a corresponding significant increase in OEF of 0.11 ± 0.06 (Figure 3.7B) measured by OxFlow, and a significant reduction in WB-CMRO₂ measured by PMRO_X and PMRO_{XASL} of 0.68 ± 0.36 and 0.67 ± 0.36 mL O₂/100 g/min, respectively; (Figure 3.5 and Figure 3.7C).

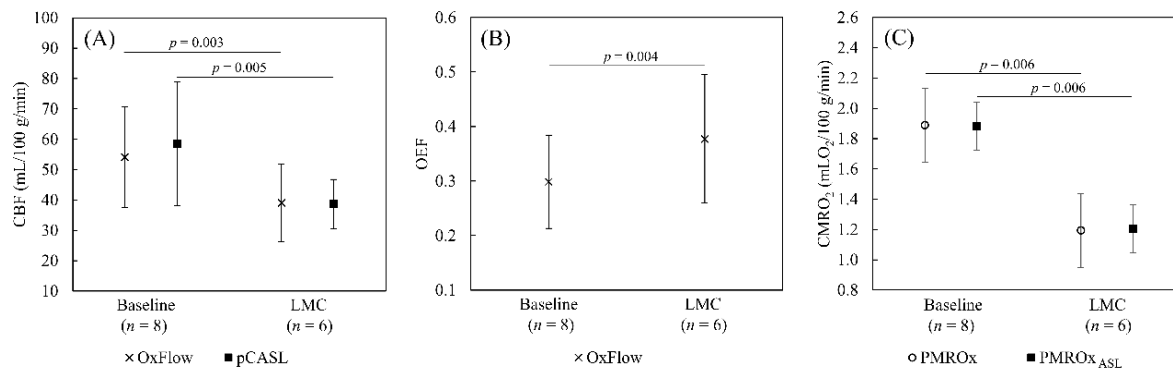


Figure 3.7. LMC results. (A) WB CBF, (B) OEF and (C) CMRO₂ values for baseline and LMC. Significant reductions in WB-CBF and WB-CMRO₂ were observed for both techniques, while a significant increase was observed for WB-OEF.

3.4 Discussion

[¹⁵O]O₂-PET has been used extensively to assess disruptions in cerebral energy metabolism, such as following stroke, predicting its risk of recurrence, and understanding energy regulation during functional activation.²²³ Despite the proven value of [¹⁵O]O₂-PET, the procedure is complex and invasive, which has led to a diminishing number of sites with the necessary expertise to conduct [¹⁵O]O₂ studies. This trend highlights the value to develop simpler [¹⁵O]O₂ imaging protocols that retain the inherent quantitative capabilities of PET. This study focused on validating a hybrid PET/MR technique developed specifically to address this issue. The possibility of using PET/MR to update [¹⁵O]O₂ imaging was investigated by Su *et al.*, who used MRI to extract image-derived AIFs.⁸² The current study explored an alternative approach using WB MRI measurements as a reference, which avoids potential registration and partial volume errors. PMROx is also less sensitive to errors caused by RW and the CBV since regional CMRO₂ is determined from the ratio of TACs.

Validation experiments were conducted using a porcine model and involved imaging CMRO₂ independently using the previously validated DBFM.¹¹⁴ For this method, an MR-compatible arterial sampling system was used to measure the AIF for both tracers. Good agreement between PMROx and DBFM was found across VOIs with respect to both OEF and CMRO₂, although a small bias was observed in the PMROx CMRO₂ estimates (Figure 3.4F). Regression analysis also demonstrated strong and moderate correlations between techniques for OEF and CMRO₂, respectively. The lower correlation for the latter is explained by its dependency on both OEF and CBF. In addition to the agreement with DBFM, PMROx was shown to be

sensitive to reduced energy metabolism caused by increasing the propofol infusion. The CMRO_2 reduction was driven by the propofol-induced decrease in CBF, since propofol caused an increase in OEF. These findings are in agreement with Oshima *et al.* who reported that propofol caused proportional decreases in CBF and CMRO_2 , but had no effect on the arterio-venous oxygen difference.²²⁴

Since the PMROx approach scales the $^{15}\text{O}]_2$ images by an MRI estimate of WB CMRO_2 , its accuracy and precision will be directly affected by the MRI methods used to calculate WB OEF and CBF. In this study, WB OEF and CMRO_2 were measured by OxFlow, which can be acquired with scan times as short as 8 s with reproducibility of 2% for S_vO_2 and 6% for WB CMRO_2 .¹⁵² The accuracy of OxFlow depends on positioning the slices orthogonal to the main magnetic field, correcting for magnetic field inhomogeneities, and using sufficient image resolution to avoid partial volume effects.¹⁵⁴ The current study presents the first simultaneous comparison of OxFlow to $^{15}\text{O}]\text{H}_2\text{O}$ and $^{15}\text{O}]_2$ PET, and no significant differences were found between techniques. This agreement is in accordance with two recent studies comparing MR measurements of S_vO_2 to either PET or direct measures from the jugular bulb.^{144,146}

PET/MR also provides the possibility of reducing the PET procedure to just $^{15}\text{O}]_2$ inhalation by replacing $^{15}\text{O}]\text{H}_2\text{O}$ -PET with ASL ($\text{PMRO}_{\text{XASL}}$). WB CBF estimates from pCASL were in good agreement to those obtained by $^{15}\text{O}]\text{H}_2\text{O}$ -PET, similar to previous ASL/PET comparisons conducted using a swine model.^{88,225} Strong correlations between regional CBF measurements were found for all VOIs except the cerebellum, which was attributed to limited spatial coverage for the pCASL sequence. Recent studies comparing ASL to PET involving human participants indicate that ASL can provide accurate CBF measurements with careful attention to common sources of error,¹³⁶ including low signal-to-noise ratio and sensitivity to transit times.¹⁴⁰ Consequently, translation to clinical studies remains an active area of research as factors such as cerebrovascular disease and ageing can impact its accuracy.¹⁰⁷

A challenge with PET-only imaging is correcting for signal contamination from the CBV.⁹² Blood volume terms were incorporated into the fitting procedure for both tracers. Although the average $^{15}\text{O}]\text{H}_2\text{O}$ V_A was larger than reported in human studies, it is in accordance with Olsen *et al.* who reported values from 9 to 18 mL/100 g in pigs, depending on partial pressures of carbon dioxide levels.²²⁶ The V_0 values were smaller since they are scaled by OEF

and the venous fraction. WB ^{15}O V_A estimates were very small for most animals, as expected, as it only becomes significant in highly vascularized regions.¹¹⁴ In one animal, V_A^w reached a non-physiological value, which was likely a result of estimating $A_w(t)$ using a physiologic model.

Although this study demonstrated the advantages of PET/MRI for imaging CMRO_2 ,¹⁰⁸ this modality is not widely accessible and requires an onsite cyclotron for ^{15}O O_2 production. A potential limitation with the current study was the indirect methods used to account for RW and CBV in the DBFM, rather than direct measurements; however, this approach has been previously validated.¹¹⁴ Lastly, Figure 3.4F indicates that the discrepancy between PMROx and DBFM increased as the difference between local and WB OEF values increased, which is attributed to neglecting RW by PMROx. It should be possible to reduce this error by incorporating a RW term in the model equation.⁶⁸

3.5 Conclusion

This study presents the validation of a noninvasive hybrid PET/MR technique to image CMRO_2 that requires a short inhalation of ^{15}O O_2 , followed by 5 min of PET and simultaneous MR imaging. Good agreement between CMRO_2 values from PMROx and the DBFM was found, and the proposed method was shown to be sensitive to reduced cerebral metabolism induced by increasing the anaesthetic level.

Chapter 4

4 Quantifying cerebral blood flow by a non-invasive PET/MR method of extracting the $[^{15}\text{O}]\text{H}_2\text{O}$ image-derived input function free of partial volume errors

Narciso L, Ssali T, Liu L, et al. Non-invasive quantification of cerebral blood flow using PET/MRI to extract the $[^{15}\text{O}]\text{H}_2\text{O}$ image-derived input function free of partial volume errors. Submitted to the *Journal of Magnetic Resonance Imaging* on December 3, 2021.

4.1 Introduction

PET remains the gold standard for imaging cerebral hemodynamics and metabolism.^{107,227} Regional measurements of CBF are obtained by collecting dynamic PET data after the administration of $[^{15}\text{O}]\text{H}_2\text{O}$ (or $[^{15}\text{O}]\text{CO}_2$) and have proven essential in understanding the impact of cerebrovascular⁷ and neurodegenerative diseases¹⁵ on brain function. However, quantifying CBF requires measuring the AIF, an invasive procedure that often limits $[^{15}\text{O}]\text{H}_2\text{O}$ PET to imaging relative CBF. Efforts to avoid arterial blood sampling have primarily focused on methods of obtaining an IDIF.^{74–77,80–85} In general, the accuracy of these methods requires careful correction of PVEs (i.e., correcting for spill-in and spill-out activity), which are typically performed by measuring the point-spread-function of the PET scanner⁷⁵ and/or using calibration factors, such as obtained by acquiring a few blood samples.¹⁹⁸ MRI angiography enables more robust vessel segmentation;^{80,83,85} however, these methods are sensitive to errors in the estimated correction factors and image registration. The latter can be reduced by using hybrid PET/MRI to collect anatomical MRIs for vessel segmentation in the same imaging session as $[^{15}\text{O}]\text{H}_2\text{O}$ PET.^{76,78,81,82}

An alternative to IDIF approaches is the double integration method (DIM) in which the TAC from a chosen reference region (e.g., whole-brain) is used to eliminate the need to measure the AIF.⁸⁶ The limitation with this approach is the inability to produce reliable absolute CBF estimates because CBF in the reference region must be assumed.⁸⁹ PET/MRI offers a solution to this limitation by incorporating an MRI measurement of WB CBF to calibrate $[^{15}\text{O}]\text{H}_2\text{O}$ -PET dynamic data.⁸⁸ This MRI-reference approach, termed PMRFlow (PET/MR imaging of CBF), can either calibrate PET data explicitly by incorporating the WB CBF measurement into the single-tissue compartment tracer kinetic model,⁸⁸ or by scaling $[^{15}\text{O}]\text{H}_2\text{O}$ -PET

images by WB CBF after intensity normalization.⁹⁰ A potential limitation is that neither of these approaches account for signal contributions from the CBV. It was originally predicted that neglecting blood-borne activity was reasonable for the typical range of regional CBF found in the healthy brain;⁸⁸ however, this assumption may not be valid when there are greater extremes in CBF or CBV, such as caused by cerebrovascular disease. An additional limitation with the method described by Ishii *et al.* is the non-linear relationship between CBF and the integral counts, which results in diminished perfusion contrast.⁸⁹

In this study, we present $\text{PMRFlow}_{\text{IDIF}}$, a modification to PMRFlow that accounts for CBV signal contributions by obtaining the IDIF from the WB $[^{15}\text{O}]\text{H}_2\text{O}$ TAC. This approach is similar to the original PMRFlow proposed by Ssali *et al.* (herein referred to as $\text{PMRFlow}_{\text{DIM}}$) in the sense that WB CBF measured by MRI is used to calibrate $[^{15}\text{O}]\text{H}_2\text{O}$ -PET data. However, by extracting the IDIF, $\text{PMRFlow}_{\text{IDIF}}$ is not a reference-based approach since CBF images are generated by fitting the standard one-tissue compartment kinetic model to dynamic PET data. The advantage of $\text{PMRFlow}_{\text{IDIF}}$ compared to IDIF methods based on vessel segmentation is that it avoids errors related to partial volume corrections. Here the accuracy of $\text{PMRFlow}_{\text{IDIF}}$ was assessed in a large animal model by comparison to CBF measurements obtained using measured AIFs. Additionally, $\text{PMRFlow}_{\text{DIM}}$ and $\text{PMRFlow}_{\text{IDIF}}$ were used to generate CBF maps from dynamic $[^{15}\text{O}]\text{H}_2\text{O}$ -PET data acquired from healthy humans. It was expected that the two methods would produce similar CBF maps in the healthy brain, except in highly vascularized tissue regions.

4.2 Theory

4.2.1 $\text{PMRFlow}_{\text{IDIF}}$

Measurements of CBF by $[^{15}\text{O}]\text{H}_2\text{O}$ -PET are based on the one-tissue compartment model, as defined by:

$$\frac{d}{dt}C_b^w(t) = f \cdot C_a^w(t) - \frac{f}{\lambda}C_b^w(t) \quad (4.1)$$

where $C_b^w(t)$ and f are the local TAC and CBF, respectively, $C_a(t)$ is the AIF, and λ is the blood-brain partition coefficient of water. The solution to Eq. (4.1), including blood-borne activity, is given by:

$$C_b^w(t) = (1 - V_A)f \cdot C_a^w(t) * e^{-\frac{f}{\lambda}t} + V_A \cdot C_a^w(t) \quad (4.2)$$

where V_A is the arterial component of the total blood volume (CBV_a), and the symbol $*$ represents the convolution operator. This equation can be rearranged to determine $C_a^w(t)$. First, the Laplace transform was applied and both sides multiplied by $\left(s + \frac{f}{\lambda}\right)$ (Eq. (4.3)). Next, the input function was isolated (Eq. (4.4)) and the inverse Laplace transform was applied to obtain the [^{15}O]H $_2\text{O}$ IDIF ($C_a^{IDIF}(t)$) in terms of the WB TAC ($C_{wb}^w(t)$), as shown in Eq. (4.5).

$$\overline{C_b^w}(s) \left(s + \frac{f}{\lambda}\right) = (1 - V_A)f_i \cdot \overline{C_a^w}(s) + V_A \overline{C_a^w}(s) \left(s + \frac{f}{\lambda}\right) \quad (4.3)$$

$$\overline{C_a^w}(s) = \frac{1}{V_A} \frac{\overline{C_b^w}(s) \left(s + \frac{f}{\lambda}\right)}{s + \left(\frac{1}{V_A} + \frac{1}{\lambda} - 1\right) f} \quad (4.4)$$

$$C_a^{IDIF}(t) = \frac{f_{wb}}{V_{Awb}} \left(\frac{1}{f_{wb}} \frac{d}{dt} C_{wb}^w(t) + \frac{1}{\lambda} C_{wb}^w(t) \right) * e^{-a_{wb}t} \quad (4.5)$$

where $a_{wb} = f_{wb}(V_{Awb}^{-1} + \lambda^{-1} - 1)$.

A similar version of Eq. (4.5) was presented by Kudomi *et al.*, but CBV_a contributions were not considered and their approach for extracting the IDIF required minimizing a cost function involving multiple tissue TACs to estimate f_{wb} and a_{wb} .⁷⁹ Hybrid PET/MR offers a simpler alternative since f_{wb} can be measured noninvasively by either phase-contrast (PC) MRI^{127,153} or ASL,¹¹⁶ while simultaneously collecting [^{15}O]H $_2\text{O}$ -PET data. Without directly measuring V_{Awb} , it can be approximated by the Grubb relationship.²²⁸

4.2.2 PMRFlow_{DIM}

The simplified PMRFlow_{DIM} approach proposed by Ssali *et al.* is described by Eq. (4.6), which can be obtained by considering WB as the reference region, recognizing that $C_a^w(t)$ is the same for all brain regions, and finally performing a double integration of Eq. (4.1):

$$f_i = f_{wb} \left[\frac{\int_0^T C_i^w(t) dt}{\int_0^T C_{wb}^w(t) dt + \frac{f_{wb}}{\lambda} \left(\int_0^T \int_0^t C_{wb}^w(u) du dt - \int_0^T \int_0^t C_i^w(u) du dt \right)} \right] \quad (4.6)$$

The derivation of PMRFlow_{DIM} including the CBV_a component is given by Eq. (4.7), which was obtained following the same procedure except using Eq. (4.2).

$$f_i = f_{wb} \cdot \mathbf{R}_{V_A} \left[\frac{\int_0^T C_i^w(t) dt - \mathbf{V}_{A_i} \int_0^T \mathbf{C}_a^w(t) dt}{\int_0^T C_{wb}^w(t) dt + \frac{f_{wb}}{\lambda} \left(\int_0^T \int_0^t C_{wb}^w(u) du dt - \mathbf{R}_{V_A} \int_0^T \int_0^t C_i^w(u) du dt \right) - \mathbf{V}_{wb}} \right] \quad (4.7)$$

where $V_{wb} = V_{A_{wb}} \int_0^T C_a^w(t) dt + \frac{f_{wb}}{\lambda} (V_{A_{wb}} - V_{A_i} \cdot R_{V_A}) \int_0^T \int_0^t C_a(u) du dt$, and R_{V_A} is the ratio $(1 - V_{A_{wb}})/(1 - V_{A_i})$. The bold quantities represent CBV-related terms, which demonstrate that correcting for CBV_a contributions require measuring $C_a^w(t)$.

4.3 Materials and Methods

4.3.1 Simulations

To assess the magnitude of error in local CBF (f_i) caused by incorrectly measuring f_{wb} by MRI, a series of $C_a^{IDIF}(t)$ curves were generated from Eq. (4.5) by varying the input f_{wb} value by $\pm 25\%$ from its true value of 50 mL/100 g/min. Each C_a^{IDIF} was subsequently included in a fitting routine with the tissue TAC generated with the true $C_a^w(t)$ that was defined by Eq. (4.8).⁶⁵

$$C_a^w(t) = t \sum_{i=1}^2 a_i e^{-\frac{t}{b_i}} \quad (4.8)$$

where $a_1 = 100$, $a_2 = 1.2$, $b_1 = 0.3$ and $b_2 = 3$. The corresponding tissue TACs were generated using the one-tissue compartment model (Eq. (4.2)) for a range of local CBF values ($f_i = 20$ to 100 mL/100 g/min), while WB and local CBV_a were fixed (i.e., $V_{A_{wb}} = V_{A_i} = 2.0$ mL/100 g). For all TACs, $\lambda = 90$ mL/100 g.⁶⁷ Similarly, the sensitivity of the method to errors in $V_{A_{wb}}$ was investigated by generating $C_a^{IDIF}(t)$ curves using $V_{A_{wb}}$ values

ranging from $\pm 25\%$ from the true value of 2.0 mL/100 g. For both sets of simulations, the derived f_i and V_{A_i} estimates were compared to the corresponding true input values.

To investigate potential truncation errors caused by numerically solving the derivative term in Eq. (4.5), $C_a^{IDIF}(t)$ curves were generated by increasing the temporal resolution from 1 s to 1 ms, and the resulting CBF estimates were compared to the input values. This analysis indicated that the optimal temporal resolution required to minimize truncation errors was 1 ms, which was implemented in the subsequent analysis of the animal and human data. Note, the derived IDIFs were subsequently interpolated to a temporal resolution of 1 s in the analysis of dynamic [^{15}O]H₂O-PET data to reduce computational time.

To evaluate the sensitivity of PMRFlow_{DIM} to local CBV_a, simulations were performed by generating TACs from Eq. (4.2) for local CBF ranging from 20 to 100 mL/100 g/min and local CBV_a ranging from 1 to 5 mL/100 g ($f_{wb} = 50$ mL/100 g/min and $V_{A_{wb}} = 2.0$ mL/100 g). Estimates of f_i were obtained with Eq. (4.6) and compared to the input values.

4.3.2 Animal experiments

The accuracy of PMRFlow_{IDIF} was assessed using retrospective data collected at Lawson Health Research Institute from animal experiments performed on a 3 T Siemens Biograph mMR system (Siemens Healthineers, Erlangen, Germany) using a 12-channel PET-compatible receiver head coil (Siemens GmbH). All experiments were conducted according to the regulations of the Canadian Council of Animal Care and approved by the Animal Care Committee at Western University and are described in detail elsewhere.^{88,229} Briefly, animals were anesthetized with 1-3% isoflurane and 6-25 mL/kg/h infusion of propofol. Study 1 consisted of data from eight animals, and CBF was measured under two of three possible P_aCO₂ levels in each experiment (i.e., hyper-, normo- and hypocapnia; see Ssali *et al.* for additional details).⁸⁸ Study 2 consisted of nine animals, and CBF was only measured at normocapnia (see section 3).²²⁹ Retrospective data from twelve animals were combined from the two studies, and only CBF measured under normocapnia was considered.

4.3.2.1 PET/MR Imaging and Postprocessing

The PET protocol involved injecting approximately 500 MBq of [^{15}O]H₂O, followed by 5 min list-mode data acquisition. Arterial blood was continuously withdrawn from a femoral

artery and the activity measured at a temporal resolution of 1 s using an MR-compatible sampling system (Swisstrace GmbH). Blood withdraw started 15 s prior to [^{15}O]H $_2\text{O}$ administration and lasted 5 min. A 15-cm long tubing (1.27 mm inner diameter) connected the femoral artery to the detector, and blood was withdrawn at a rate of 5 mL/min. At the end of the experiment, the animal was euthanized and transported to a CT scanner to obtain a post-mortem CT-based attenuation correction map.

Each measured AIF, $g(t)$, was corrected for internal dispersion and delay by first fitting the WB TAC, $C_{wb}(t)$, by Eq. (4.9) to obtain the dispersion (τ) and delay (Δt) constants.^{70,73} The corrected AIF, $C_a(t)$, which was used in the subsequent analyses, was obtained from Eq. (4.10).

$$C_{wb}^w(t) = A \tau g(t + \Delta t) + (1 - B \tau) A g(t + \Delta t) * e^{-Bt} \quad (4.9)$$

$$C_a^w(t) = \tau \frac{d}{dt} g(t + \Delta t) + g(t + \Delta t) \quad (4.10)$$

where A and B are arbitrary variables.

Using the Siemens e7-tools suite, dynamic PET images were reconstructed into time frames using a 3D-ordinary Poisson-OSEM method with 4 iterations and 21 subsets (matrix size, 344×344×127 voxels; FoV, 359×359×258 mm; voxel size, 1×1×2 mm; zoom factor, 2). Raw PET data were corrected for decay, random incidences, dead-time, detector normalization, data rebinning, and scatter. Finally, reconstructed PET images were spatially smoothed by a 4-mm Gaussian filter.

MR acquisition began by acquiring T $_1$ -weighted images (magnetization-prepared rapid gradient-echo sequence, MPRAGE; repetition/echo/inversion times [TR/TE/TI], 2,000/2.98/900 ms; flip angle [FA], 9°; FoV, 256×256 mm 2 ; 176 slices; isotropic voxel size, 1 mm 3), followed by time-of-flight images to identify the feeding arteries for PC imaging (TR/TE, 22/3.75 ms; FA, 18°; FoV, 200×181 mm 2 ; 102 slices; voxel size, 0.3×0.3×1.5 mm 3 ; 40 mm saturation band). During PET acquisition, PC MRI data were acquired to measure total CBF through the internal carotid and basilar arteries. For study 1, gated PC images were acquired (TR/TE, 34.4/2.87 ms; matrix, 320×320; voxel size, 0.625×0.625×5 mm; velocity

encoding, 80 cm/s).¹²¹ For study 2, a non-gated PC MRI sequence was implemented (TR/TE/ Δ TE, 35/7.025/2.5 ms; FA, 25°; FoV, 208×208 mm²; voxel size, 1.6×1.6×5.0 mm³; velocity encoding, 60 cm/s).^{153,154} PC data were converted into WB CBF measurements using in-house MATLAB (MathWorks) scripts.

To derive an IDIF from Eq. (4.5), a semi-automatic procedure was used to define a VOI encompassing the brain in each anatomical slice. The final WB VOI, which was the composite of all the slices, was transferred to the dynamic [¹⁵O]H₂O-PET images to extract the WB TAC.

4.3.2.2 Regional measurements

For the animal experiments, MPRAGE images were used to define VOIs for the cerebellum (4.6 ± 1.1 cm³), diencephalon (4.1 ± 1.0 cm³), and the frontal (4.3 ± 1.0 cm³), occipital (9.4 ± 2.3 cm³), parietal (7.6 ± 2.4 cm³), and temporal (6.0 ± 0.7 cm³) lobes. These VOIs were transferred to the corresponding CBF images to extract regional CBF estimates. All images were registered to the anatomical image of a single animal to generate group-wise maps using SPM12 (<https://www.fil.ion.ucl.ac.uk/spm/>). Relative CBF (rCBF) was calculated by normalizing the absolute CBF maps by their respective voxel-wise mean. This was performed to compare regional CBF measurements from PMRFlow_{IDIF} and PET-only without the added variability caused by potential differences in WB CBF from PC-MRI and PET.

4.3.3 Human experiments

This study was approved by the Western University Health Sciences Research Ethics Board and was conducted in accordance with the Declaration of Helsinki ethical standards. Participants provided written informed consent in compliance with the Tri-Council Policy Statement of Ethical Conduct for Research Involving Humans. Neurologically healthy participants were recruited through advertisements or the volunteer pool at the Cognitive Neurology and Aging Brain Clinic at Parkwood Hospital (St Joseph's Health Care London). Raw data were collected at Lawson Health Research Institute as part of a broader clinical study.

Scanning was performed on a 3T Siemens Biograph mMR scanner using a 12-channel head coil. Participants abstained from caffeine 8 hours prior to their scanning session. Each session began with acquiring MPRAGE images (TR/TE, 2000/2.98 ms; voxel size, isotropic 1 mm³; FoV, 256×256 mm; 176 slices) and time-of-flight images to identify the feeding

arteries for PC imaging (TR/TE, 22/3.75 ms; FA, 18°; FoV, 200×181 mm²; 120 slices; voxel size, 0.3×0.3×1.5 mm³; 40 mm saturation band). The PET protocol consisted of five minutes of list-mode data acquired immediately after a bolus injection of approximately 700 MBq of [¹⁵O]H₂O through the antecubital vein. During the PET acquisition, non-gated PC-MRI data were acquired by positioning the imaging plane perpendicular to the main magnetic field and encompassing the internal carotid and vertebral arteries (TR/TE/ΔTE, 35/7.025/2.5 ms; FA, 25°; FoV, 208×208 mm²; voxel size, 1.6×1.6×5.0 mm³; velocity encoding, 70 cm/s).^{153,154}

4.3.3.1 PET/MR Imaging and Postprocessing

PET data were reconstructed into 37 time frames (20×3 s, 6×5 s, 6×10 s, 5×30 s) using the iterative algorithm 3D-ordinary Poisson-OSEM (3 iterations, 21 subsets, 3D gaussian filter of 4 mm, and a zoom factor of 2) with corrections for decay, random incidences, dead-time, detector normalization, data rebinning, attenuation, and scatter. Images were reconstructed into a 172×172×127 matrix with voxel size of 2.09×2.09×2.03 mm. MR-based attenuation correction was performed with a vendor-provided two-point Dixon sequence (TR/TE₁/TE₂, 4.14/1.28/2.51 ms; FoV, 240×126×132 mm³; voxel size, 2.09×2.09×2.02 mm³).

As with the animal experiments, PC images were converted into global CBF measurements using in-house MATLAB scripts.¹⁵³ Briefly, regions-of-interest were semi-automatically drawn in the internal carotid and vertebral arteries on the magnitude image and transferred to the phase image. Phase results were converted into velocity¹²¹ and then flow by assuming a density of brain tissue of 1.05 g/mL. Anatomical MPRAGE images were segmented into six tissue classes using SPM12, followed by the creation of a WB mask by combining GM and WM tissue probability maps (80% threshold; cerebrospinal fluid voxels excluded). These masks were used to obtain WB TACs, which were subsequently used in Eq. (4.5) to obtain the IDIFs.

4.3.3.2 Regional measurements

Anatomical MPRAGE images were normalized to the MNI (Montreal Neurological Institute) space using SPM12 and the same deformation field was applied to the dynamic PET data, as well as the resulting CBF and CBV_a images. Average TACs were extracted from GM and WM, and eight VOIs (frontal, occipital and temporal lobes, insula, hippocampus,

precuneus, dorsal striatum, and cerebellum) using the automated anatomical labeling atlas (Wake Forest University Pickatlas, <http://fmri.wfubmc.edu/cms/software>). Masks generated for the frontal, occipital and temporal lobes, as well as the cerebellum, were eroded with a disk-shaped structuring element (2-voxels radius) to extract mainly the central part of the VOIs while avoiding PVE at the boundaries. For $\text{PMRFlow}_{\text{IDIF}}$, Eq. (4.2) was first fit to the high signal-to-noise TACs from individual VOIs to obtain CBF and CBV_a measurements, as described in the subsequent section. Next, voxel-wise maps were generated by fitting Eq. (4.2) to each voxel TAC. Additionally, VOI and voxel-wise $\text{PMRFlow}_{\text{DIM}}$ estimates of CBF were computed using Eq. (4.6) with an integration time of 5 min (the same estimate of WB CBF from PC-MRI was used for both PMRFlow methods).

4.3.4 CBF estimates

CBF and CBV_a maps from both the animal and human experiments were generated using the MATLAB nonlinear optimization routine *fmincon* incorporating a weighted nonlinear least squares (WNLLS) approach. The relative weight for each time frame was computed as the ratio between the frame length and the WB activity concentration. For each voxel or VOI, the fitting parameters were f_i and V_{A_i} . The fitting was performed twice for the animal experiments, once using the measured AIF, $C_a^w(t)$, (i.e., PET alone) and once using the IDIF obtained from Eq. (4.5), $C_a^{\text{IDIF}}(t)$, (i.e., $\text{PMRFlow}_{\text{IDIF}}$). Only the latter was used to analyze the human data since arterial blood samples were not acquired. CBV_a ($V_{A_{wb}}$) used to obtain $C_a^{\text{IDIF}}(t)$ from Eq. (4.5) was estimated by $V_{A_{wb}} = \frac{1}{2} 0.80 (f_{wb})^{0.38, 44}$ where the factor of $\frac{1}{2}$ was included considering the arterial component represents approximately half of the total CBV.²⁰⁹ As the definition of the IDIF provided by Eq. (4.5) includes the derivative of the WB TAC, it was necessary to interpolate each WB TAC to a temporal resolution of 1 ms to avoid discretization errors (see simulation results).

4.3.5 Statistics

In the validation study, correlation analysis between CBF measurements obtained with $\text{PMRFlow}_{\text{IDIF}}$ and PET was performed for each animal separately to address the inter-subject variability. Furthermore, correlation between $\text{PMRFlow}_{\text{IDIF}}$ and $\text{PMRFlow}_{\text{DIM}}$ regional CBF estimates from the human data was assessed for each VOI from which Pearson correlation coefficients (ρ) were obtained. Paired *t*-tests were performed to evaluate differences between

techniques. Potential biases were assessed using a one-sample t -test. The intraclass correlation coefficient (ICC) was used to assess reliability (two-way mixed-effects, single measurement, absolute agreement), and agreement was considered excellent, good, or moderate based on an ICC above 0.90, between 0.75 and 0.89, or between 0.50 and 0.74, respectively. Statistical significance was defined by $\alpha = 0.05$. Measurements are expressed in terms of mean \pm one standard deviation. All datasets were found to be normally distributed, which was tested by a combination of Kolmogorov-Smirnov tests, histograms, and normal Q-Q plots. Statistical tests were performed using SPSS Statistics (v. 26, International Business Machines Corporation, <https://www.ibm.com/analytics/spss-statistics-software>).

4.4 Results

4.4.1 Error analysis

Simulations showed that errors in the input WB CBF (f_{wb}) parameter led to equivalent errors in local CBF (f_i) obtained with PMRFlow_{IDIF} across the range of CBF values investigated (i.e., 10% error in f_{wb} yielded a 10% error in f_i ; Figure 4.1A), while errors in f_{wb} had far less effect on local CBV_a (V_{A_i}) (Figure 4.1B). Similarly, errors in WB CBV_a ($V_{A_{wb}}$) had negligible impact on f_i ($< 0.1\%$ across the CBV_a range; Figure 4.1C) but a one-to-one effect on V_{A_i} . Truncation errors related to numerically solving the derivative term in Eq. (4.5) can be reduced to less than 0.3% for local CBF (Figure 4.1D) and 5% for local CBV_a (Figure 4.1E) by interpolating the WB TAC to a bin size of 1 ms prior to obtaining the IDIF. Lastly, the predicted error in local CBF estimates obtained with PMRFlow_{DIM} (Eq. (4.6)) over a range of CBF and CBV_a values is shown in Figure 4.1F.

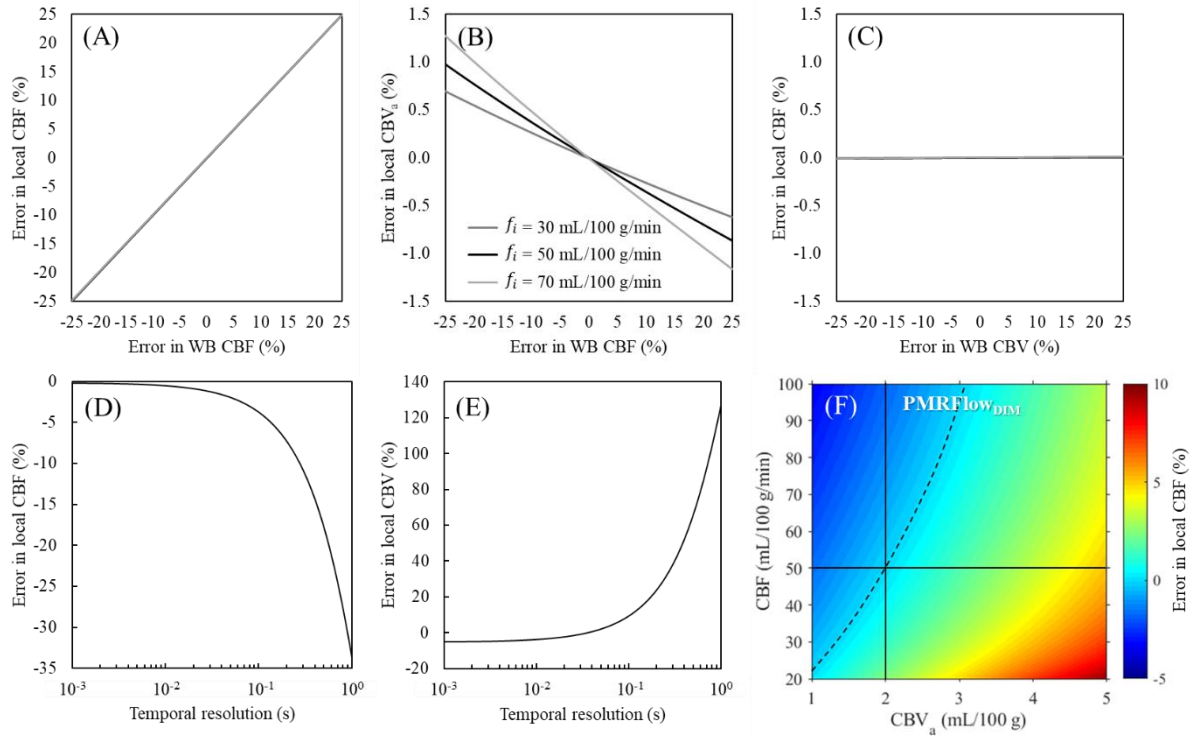


Figure 4.1. Simulation results. Predicted error in (A) local CBF (f_i) and (B) local CBV_a (V_{A_i}) from PMRFlow_{IDIF} as a function of the error in WB CBF (f_{wb}) used to determine the IDIF from Eq. (4.5). (C) Predicted error in local CBF from PMRFlow_{IDIF} as a function of the error in WB CBV ($V_{A_{wb}}$) used to determine the IDIF from Eq. (4.5). Legends for (A) and (C) are shown in (B). Predicted error in (D) local CBF and (E) local CBV_a as a function of the temporal resolution used to determine the IDIF from Eq. (4.5). (F) Predicted error in local CBF obtained from PMRFlow_{DIM} (Eq. (4.6)) over a range of local CBF and CBV_a values. The horizontal and vertical lines represent the chosen f_{wb} and $V_{A_{wb}}$ values, respectively. A prediction of no error is represented by the dashed line.

4.4.2 Validation study

Data were acquired in 12 juvenile Duroc pigs (19.6 ± 2.4 kg, 10 females, age-range 8-10 weeks). The mean dispersion constant for the measured AIFs was 9.5 ± 2.6 s. Figure 4.2A-B presents a comparison between the dispersion-corrected AIFs (Figure 4.2A) and the IDIFs (Figure 4.2B). The average ratio of the area under the curve (AUC) across conditions between the dispersion-corrected and the measured AIFs was 1.02 ± 0.01 . Likewise, average AUC ratio between the IDIFs and the AIFs was 1.13 ± 0.08 . Average voxel-wise CBF estimates from PMRFlow_{IDIF} and PET were 58.0 ± 16.9 and 63.0 ± 18.9 mL/100 g/min, respectively (ns.). Mean voxel-wise CBV_a estimates from PMRFlow_{IDIF} and PET were 1.91 ± 1.46 and 0.76 ± 0.54 mL/100 g, respectively ($p < 0.05$).

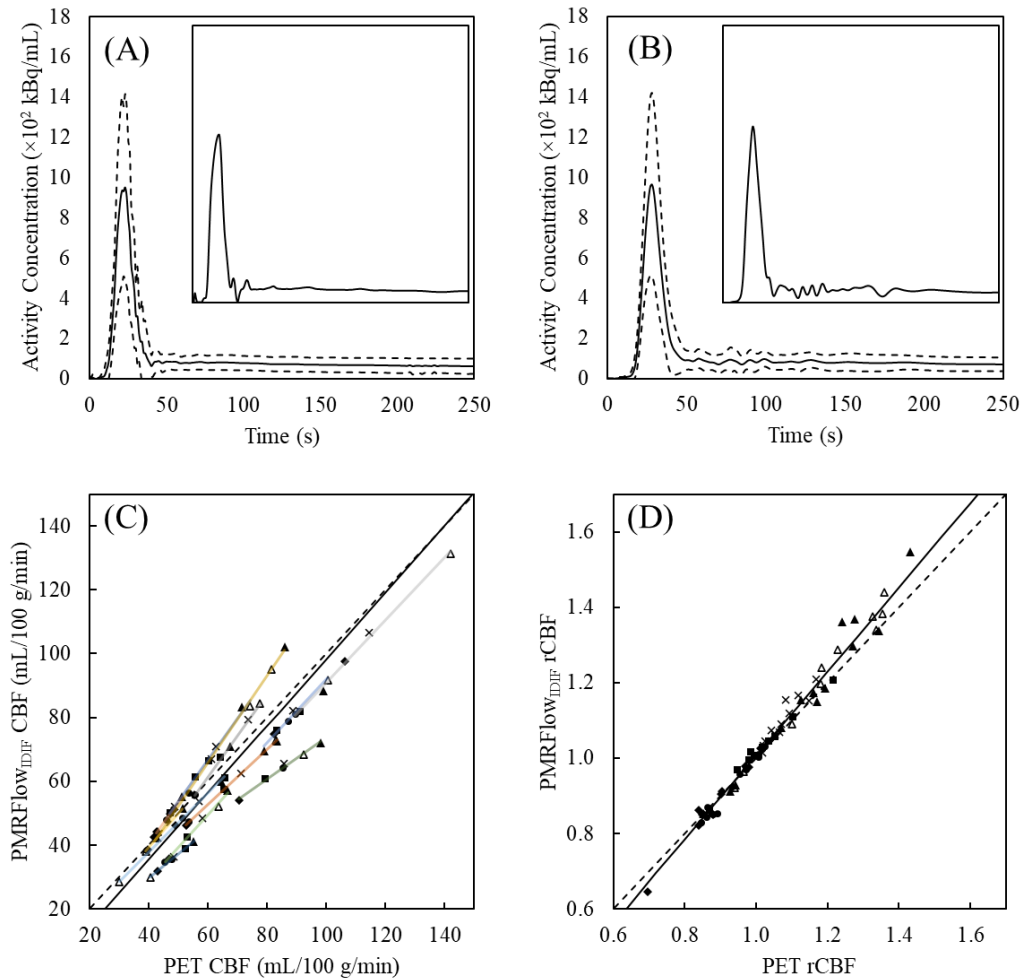


Figure 4.2. Comparison between AIFs and IDIFs and validation results. (A) Dispersion-corrected AIFs and respective (B) IDIFs obtained with Eq. (4.5) ($n = 12$). Average curves are represented by the solid lines (with their respective \pm one standard deviation represented as dashed lines.) The insert in each figure presents corresponding data from one representative animal. Regional (C) CBF and (D) rCBF estimates ($n = 12$) obtained from PMRFlow_{IDIF} plotted as a function of the corresponding PET measurements. Regression analysis between the two techniques was performed for each animal separately. Average regression slopes for CBF and rCBF were 1.04 ± 0.23 and 1.11 ± 0.14 , respectively (solid black line with respective intercepts of -6.2 ± 7.7 mL/100 g/min and -0.11 ± 0.13). Each colored line in (C) represents a regression performed on an individual animal. The dashed line is the identity line.

Regional absolute and relative CBF estimates from PMRFlow_{IDIF} and PET are summarized in Table 4.1. Relative estimates are provided to show the agreement in regional CBF measurements from the two methods after removing differences in WB CBF estimates from PC MRI and PET. Regression results comparing regional CBF values from the two techniques for individual animals are shown in Figure 4.2C. The average regression slope was 1.04 ± 0.23 (intercept = -6.2 ± 7.7 mL/100 g/min, $R^2 = 0.996 \pm 0.005$, $\rho = 0.998 \pm 0.003$, $p < 0.01$). Average regression slope for the rCBF estimates was 1.11 ± 0.14 (intercept = -0.11 ± 0.13 ; Figure 4.2D). Good-to-excellent reliability was observed across VOIs, with mean ICC of

0.86 ± 0.07 and 0.94 ± 0.06 for CBF and rCBF measurements, respectively. Small differences between PMRFlow_{IDIF} and PET estimates of CBF and rCBF were observed for all VOIs, with mean CBF and rCBF differences of -4.4 mL/100 g/min and 1.12%, respectively. Finally, Figure 4.3 shows group-wise CBF and CBV_a images from PET and PMRFlow_{IDIF}.

Table 4.1. Summary results from validation study. Summary results of local CBF (in mL/100 g/min) and rCBF estimated by PET and PMRFlow_{IDIF} at normocapnia ($n = 12$). The ICC for each region and the differences between the respective measurements are also provided.

VOI	CBF (mL/100 g/min)		ICC	CBF Difference (mL/100 g/min)
	PET	PMRFlow _{IDIF}		
Cerebellum	72.7 ± 16.5	68.6 ± 17.0	0.75	-4.1 ± 11.7
Diencephalon	72.2 ± 31.8	68.3 ± 31.0	0.92	-3.9 ± 10.6
Frontal Lobe	56.4 ± 20.2	51.4 ± 18.3^a	0.81	-4.9 ± 6.2^b
Occipital Lobe	63.3 ± 14.8	58.8 ± 13.5	0.86	-4.5 ± 7.9
Temporal Lobe	58.6 ± 17.9	53.3 ± 15.2^a	0.90	-5.3 ± 7.4^b
Parietal Lobe	67.7 ± 20.5	63.9 ± 19.4	0.94	-3.8 ± 8.6
VOI	rCBF		ICC	rCBF Difference (%)
Cerebellum	1.18 ± 0.15	1.21 ± 0.19		
Diencephalon	1.11 ± 0.25	1.14 ± 0.27^a	0.98	2.05 ± 2.49^b
Frontal Lobe	0.89 ± 0.08	0.88 ± 0.10	0.99	-0.74 ± 2.69
Occipital Lobe	1.02 ± 0.09	1.03 ± 0.08^a	0.98	0.86 ± 1.16^b
Temporal Lobe	0.93 ± 0.07	0.92 ± 0.08	0.85	-0.83 ± 1.71
Parietal Lobe	1.07 ± 0.05	1.10 ± 0.06^a	0.90	-2.22 ± 1.94^b

^a Statistically different than the respective PET measurement ($p < 0.05$).

^b Statistically different than zero ($p < 0.05$).

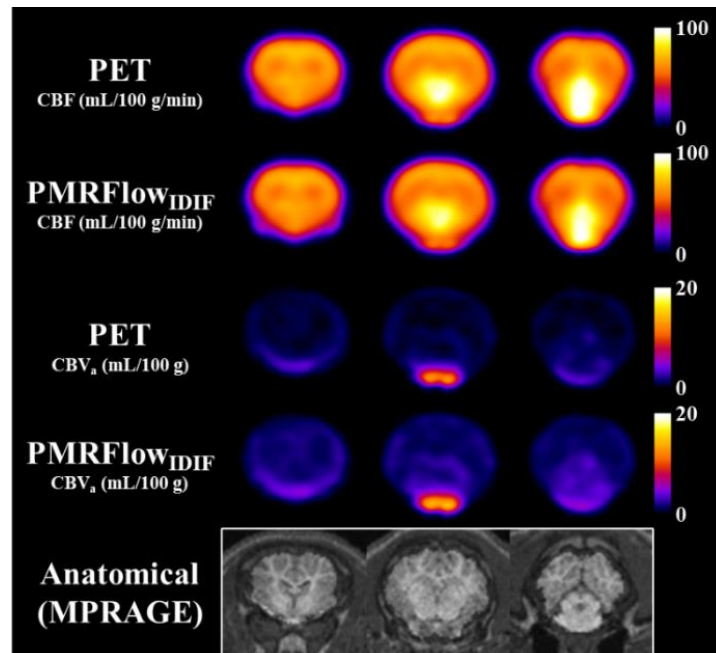


Figure 4.3. Group-wise CBF and CBV_a images from validation study. Group-wise CBF and CBV_a images obtained from PET using the measured AIF and from PMRFlow_{IDIF} ($n = 12$). All images were registered to the anatomical images from one animal. For anatomical reference, the bottom row shows the MPRAGE images from one animal.

4.4.3 Assessment with human data

Complete data sets were acquired from 13 individuals (64 ± 10 years, 80 ± 20 kg, 8M/5F; average injected activity, 730 ± 60 MBq [range 620-790 MBq]; average injected activity per body weight, 9.4 ± 2.4 MBq/kg [range 5.6-14.1 MBq/kg]). Average WB CBF from PC MRI was 41.3 ± 5.7 mL/100 g/min. Figure 4.4A shows the average IDIF obtained with Eq. (4.5). Summary of regional CBF and CBV_a estimates from the VOI-based analysis is provided in Table 4.2 for $PMRFlow_{IDIF}$ and $PMRFlow_{DIM}$.

Table 4.2. Summary results from assessment with human data. Summary of VOI-based CBF and CBV_a estimates from $PMRFlow_{IDIF}$ and $PMRFlow_{DIM}$.

VOI	CBF (mL/100 g/min)		CBV_a (mL/100 g)
	$PMRFlow_{DIM}$	$PMRFlow_{IDIF}$	$PMRFlow_{IDIF}$
GM	45.1 ± 6.6^a	44.6 ± 6.4	1.22 ± 0.06
WM	36.2 ± 5.1^a	36.0 ± 5.0	1.15 ± 0.10
Insula	58.0 ± 9.3^a	51.6 ± 7.0	3.25 ± 0.48
Hippocampus	48.1 ± 9.8^a	44.9 ± 8.0	2.10 ± 0.52
Precuneus	45.2 ± 7.2	45.3 ± 7.0	0.59 ± 0.16
Dorsal Striatum	45.4 ± 9.0^a	44.2 ± 8.0	1.32 ± 0.25
Frontal Lobe	45.0 ± 6.2	44.6 ± 5.8	1.14 ± 0.21
Occipital Lobe	44.0 ± 9.0^a	44.9 ± 9.2	0.59 ± 0.27
Temporal Lobe	44.3 ± 6.6^a	43.5 ± 6.2	1.34 ± 0.16
Cerebellum	61.4 ± 13.2^a	55.4 ± 9.4	0.02 ± 0.06

^a Statistically different than the respective $PMRFlow_{IDIF}$ measurement ($p < 0.05$).

Average voxel-wise CBV_a estimate across the whole brain was 1.28 ± 0.07 mL/100 g. Figure 4.4B-D presents the comparison of local CBF measurements from $PMRFlow_{DIM}$ to $PMRFlow_{IDIF}$. Average regression line between $PMRFlow_{DIM}$ and $PMRFlow_{IDIF}$ CBF estimates had a slope of 1.15 ± 0.15 and an intercept of -5.16 ± 5.28 mL/100 g/min ($R^2 = 0.99 \pm 0.01$; $\rho = 0.995 \pm 0.005$, $p < 0.01$; Figure 4.4B). Excellent reliability was observed for all VOIs (ICC = 0.93 ± 0.10) except the insula (ICC = 0.73). Figure 4.4C shows the corresponding Bland-Altman plots. Small differences between $PMRFlow_{DIM}$ and $PMRFlow_{IDIF}$ estimates of CBF were observed for all VOIs, with a mean CBF difference of 2.1 mL/100 g/min (non-significant for the precuneus and frontal lobe, $p < 0.01$ otherwise; Figure 4.4C). Lastly, Figure 4.4D presents differences in CBF estimates plotted as a function of mean regional CBV_a determined by $PMRFlow_{IDIF}$. Group-wise images from the two methods are presented in Figure 4.5, alongside with anatomical images and the VOIs included in the analysis.

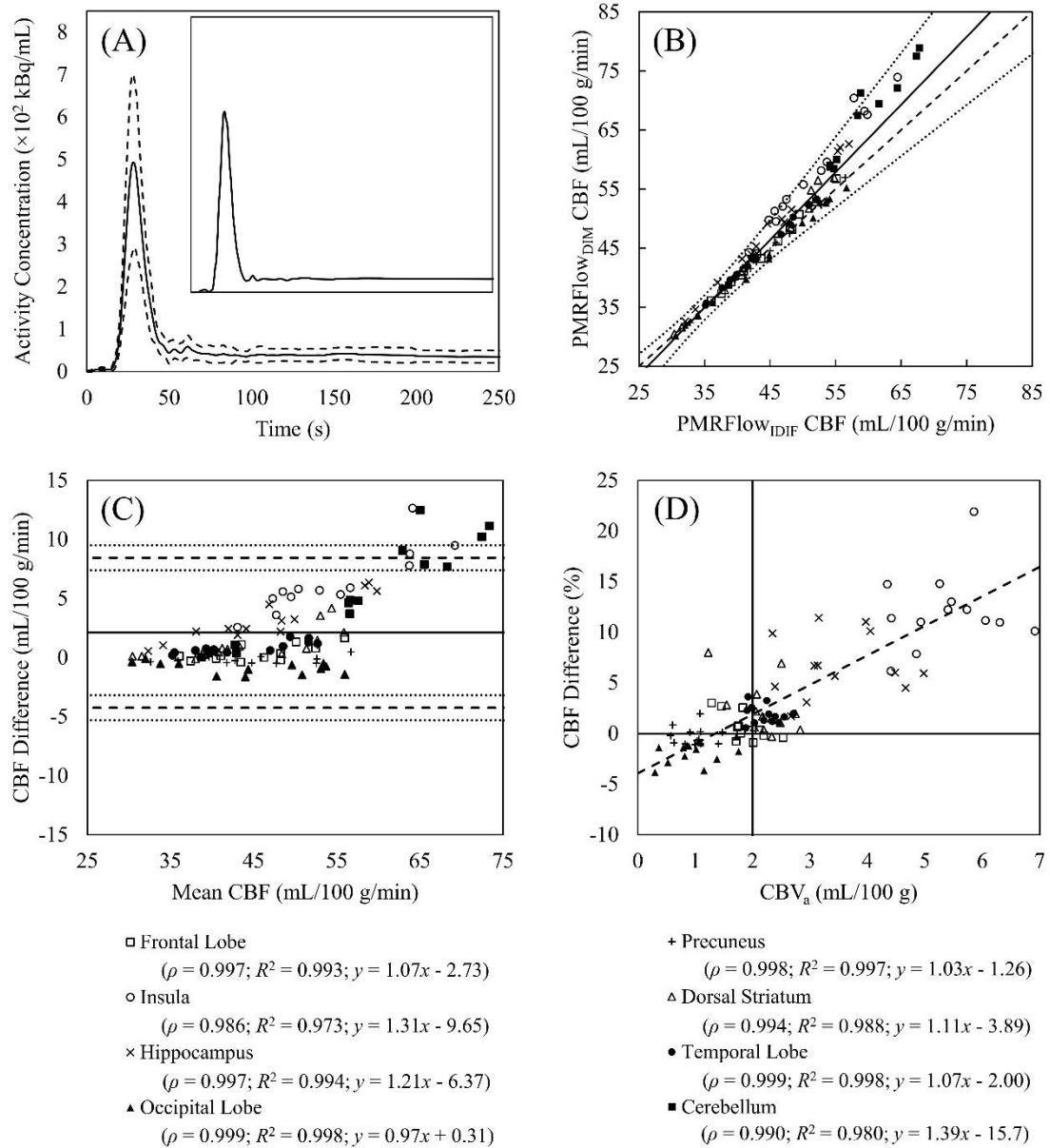


Figure 4.4. Results from the assessment with human data. (A) Average [^{15}O]H $_2$ O IDIF from human data (solid line). The dashed lines represent \pm one standard deviation. One individual [^{15}O]H $_2$ O IDIF is presented in the insert for visual reference. (B) Regional CBF estimates ($n = 13$) comparing PMRFlow_{DIM} to PMRFlow_{IDIF} (average regression (solid line) had a slope of 1.15 ± 0.15 and an intercept of -5.16 ± 5.28 mL/100 g/min, $R^2 = 0.99 \pm 0.01$; dotted lines represent the 95% confidence interval) Dashed line is the identity line. Correlation and regression results from (B) are shown on the bottom. Corresponding Bland-Altman plot is presented in (C), where the mean is represented by the solid line. The dashed lines represent the limits of agreement (± 2 standard deviations), each with its own 95% confidence intervals (dotted lines). Mean CBF difference across VOIs was 2.14 mL/100 g/min (significance was observed for all VOIs except for the precuneus and frontal lobe, $p < 0.01$). (D) Difference between PMRFlow_{DIM} and PMRFlow_{IDIF} CBF measurements plotted as a function of arterial CBV. For each subject, regional CBV_a values were normalized to WB CBV_a and scaled to 2.0 mL/100 g (solid vertical line). Results from the cerebellum were removed due to the unrealistically low CBV_a estimates obtained with PMRFlow_{IDIF}. Dashed line represents average regression line ($y = -3.9x + 16.5$; $R^2 = 0.85 \pm 0.15$; regression was performed per individual).

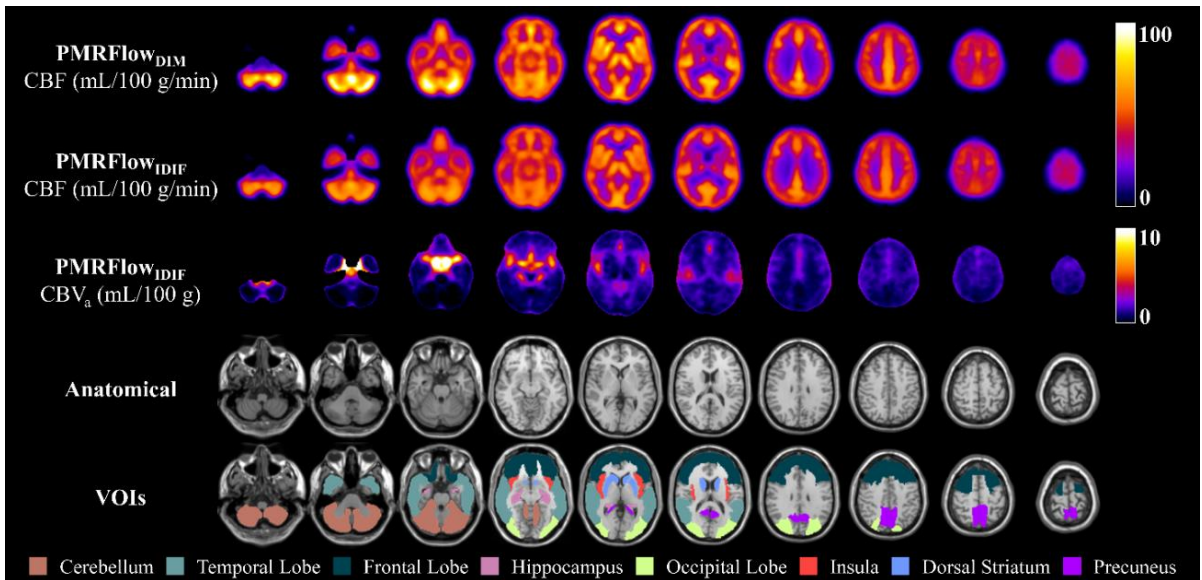


Figure 4.5. Group-wise CBF and CBV_a images from human data. Group-wise CBF and CBV_a images ($n = 13$) obtained with $PMRFlow_{IDIF}$ (second and third rows), alongside with CBF images from $PMRFlow_{DIM}$ (first row). All images were normalized to the MNI space. Anatomical images and VOIs are presented for visual reference.

4.5 Discussion

The gold standard for imaging CBF in humans is $[^{15}O]H_2O$ PET; however, the need to sample arterial blood is not only invasive, but technically complex due to the challenges of collecting serial blood samples reliably. The pursuit of a non-invasive alternative led to the development of $PMRFlow_{DIM}$, which takes advantage of hybrid PET/MRI by using WB CBF estimates from MRI to calibrate $[^{15}O]H_2O$ -PET data.⁸⁸ This fast, reliable, and simple technique has been validated⁸⁸ and implemented to evaluate hypoperfusion in dementia patients.²³⁰ A potential limitation with $PMRFlow_{DIM}$ is that it neglects blood-borne activity, which can cause errors in CBF due to regional variations in arterial CBV, particularly in highly vascularized regions (Figure 4.1F). As demonstrated by Eq. (4.7), correcting for CBV_a signal contributions requires knowing $C_a^w(t)$. Thus, this study investigated an alternative PET/MR method, $PMRFlow_{IDIF}$, that uses WB CBF from PC MRI to extract the IDIF, which is subsequently incorporated into a standard WNLLS fitting approach to map CBF and CBV_a .

Simulations demonstrated that there is a one-to-one relationship between errors in regional CBF obtained by $PMRFlow_{IDIF}$ and WB CBF estimates from PC MRI, in agreement with the original $PMRFlow_{DIM}$ method.⁸⁸ This relationship explains the deviations in the regression results plotted in Figure 4.2C. While the goodness of fit across brain regions for each

animal individually was extremely high, as indicated by the R^2 values, the deviation observed between animals reflects discrepancies in WB CBF estimates from PC MRI and PET. This was confirmed by comparing regional rCBF estimates from PMRFlow_{IDIF} and PET (Figure 4.2D). These findings highlight the need to ensure the accuracy and precision of the MRI technique chosen to provide the reference CBF estimate. In this study, we selected PC MRI given its ability to generate highly reproducible estimates of WB CBF with short scan durations.^{122,123} Unlike our previous validation studies using a porcine model,^{88,229} other studies reported that PC MRI overestimated global CBF in comparison to [¹⁵O]H₂O PET.^{76,126,129} It is known that [¹⁵O]H₂O PET can underestimate CBF due to the limited diffusion of water across the blood-brain barrier,²³¹ which could explain this overestimation. Alternatively, the accuracy of PC MRI can be degraded by partial volume errors from insufficient spatial resolution, phase aliasing, variations in flow during the cardiac cycle, and inappropriate positioning of the imaging plane.^{127,128} It should be noted that the average WB CBF from the human experiments obtained with PC MRI (41.3 ± 5.7 mL/100 g/min) is within the expected range.¹¹¹

The mean ratio of the AUC between the IDIF and dispersion-corrected AIF in the validation study was 1.15 ± 0.24 . Since AUC and CBF are inversely proportional,⁸³ this results indicates that CBF estimates from PMRFlow_{IDIF} should be slightly underestimated compared to values obtained using the AIF. This prediction is evident in Table 4.1, in which the PMRFlow_{IDIF} values of CBF were consistently lower than the corresponding values from PET, although significance was only observed for the frontal and temporal lobes. The difference in AUC is likely due to errors in the masks used to obtain the WB TACs, which were generated semi-automatically. Given the relatively small size of the pig brain, the masks typically included small regions outside of the brain as well as cerebrospinal fluid. This should be less of an issue in human studies considering multiple packages are available for brain extraction and segmentation have been extensively validated.

The CBF estimates from PMRFlow_{IDIF} in the porcine study were in good agreement with the corresponding PET-only estimates (Table 4.1) and similar to previous studies.^{88,226,229} In contrast, the CBV_a estimates from PMRFlow_{IDIF} were significantly different from the PET values. This discrepancy indicates that setting WB CBV based on the Grubb relationship was likely not accurate. Another consideration is truncation errors caused by determining the IDIF from Eq. (4.5), which includes a derivative term. In the current study, resampling the TAC in

milliseconds was sufficient to minimize errors in regional CBF estimates (Figure 4.1D), but corresponding CBV_a values were underestimated by roughly 5% (Figure 4.1E).

The IDIFs obtained with $PMRFlow_{IDIF}$ from the human study (Figure 4.4A) showed good quality, with similar shapes and noise levels expected for typical IDIFs and AIFs for $[^{15}O]H_2O$.⁷⁶ Furthermore, the CBF estimates from both $PMRFlow$ techniques (Table 4.2) are within the expected range¹¹¹ across the selected brain regions. Good visual agreement between CBF maps from the two techniques was also observed (Figure 4.5), except in the cerebellum and deep GM structures. This disagreement is most likely a consequence of $PMRFlow_{DIM}$ not accounting for blood-borne activity contribution, as indicated in Figure 4.4D. This figure indicates that flow discrepancies between the two methods were greater in brain regions that had larger local-to-WB CBV_a differences (i.e., the insula and hippocampus). This source of error with $PMRFlow_{DIM}$ will likely be greater for pathologies such as cerebrovascular disease that are characterized by larger variations in regional CBV_a . The CBV_a maps generated by $PMRFlow_{IDIF}$ (Figure 4.5) exhibited the expected pattern based on the distribution of cerebral arteries, and the values were in agreement with previous studies,^{209,232} except in the cerebellum. However, the absolute CBV_a values should be interpreted with caution, as discussed above, and it is important to note that errors in CBV_a had negligible effect on regional CBF estimates ($< 0.1\%$; Figure 4.1C).

The majority of approaches for extracting the IDIF rely on vessel segmentation to isolate the time-varying activity in the feeding vessels. By providing simultaneous image acquisition, PET/MRI helps minimize misalignment errors between the MR angiogram used for vessel segmentation and the dynamic PET images.⁷⁸ Recently, strong correlation between CBF estimates generated using the AIF and the corresponding IDIF was reported.⁷⁶ However, this approach still requires correcting for PVEs; specifically, the loss of activity from the artery due to the inherently poor spatial resolution of PET and spill-in activity from surrounding tissues. Regarding the latter, careful positioning of the arterial region of interest is typically performed to avoid regions with high activity such as the jugular veins. Given the balancing between these sources of error, Zanotti-Fregonara *et al.* recommended scaling the IDIF by blood samples to improve reliability,¹⁹⁸ however, this can be challenging with $[^{15}O]H_2O$.⁷⁶ By using WB CBF measured by MRI as a scaler, $PMRFlow_{IDIF}$ offers an alternative approach for extracting the IDIF that avoids these sources of error. It is similar to the approach proposed by Kudomi *et al.*,

except it requires only a single TAC to obtain the IDIF, whereas their PET method requires approximately 500 TACs to estimate the common IDIF.⁷⁹

4.6 Conclusion

This study presented a robust, non-invasive, PVE-free hybrid PET/MR technique for obtaining IDIF of $[^{15}\text{O}]\text{H}_2\text{O}$. The approach was validated against PET-only measurements of CBF in a porcine model in which the AIF was directly measured. A comparison of absolute and relative CBF estimates indicated that the primary source of error was discrepancies between WB CBF measured by PC MRI and PET, in agreement with simulations. $\text{PMRFlow}_{\text{IDIF}}$ along with the original reference-based PET/MR technique $\text{PMRFlow}_{\text{DIM}}$ were applied to $[^{15}\text{O}]\text{H}_2\text{O}$ data from healthy volunteers. The two methods produced similar CBF maps with the greatest differences found in regions in which CBV_a contributions deviated from the WB value—again in agreement with model predictions. Future work is needed to confirm the $\text{PMRFlow}_{\text{IDIF}}$ accuracy in cases that likely have significant regional vascular alterations, such as resulting from cerebrovascular diseases.

Chapter 5

5 Conclusions and future work

5.1 Summary of findings

This thesis explored the feasibility of using hybrid PET/MRI to non-invasively measure parameters of cerebral metabolism. First, PET/MR imaging of oxidative metabolism (PMRO_x), in which MRI estimates of WB CMRO₂ are used as reference for analyzing [¹⁵O]O₂-PET data, was evaluated and validated in an animal model. Then, an alternative to the previously proposed PET/MR technique to image local CBF was presented, in which WB CBF from MRI was used to calibrate the [¹⁵O]H₂O IDIF (PMRFlow_{IDIF}) extracted from the WB TAC—chosen due to its high signal-to-noise ratio. In this final chapter, the major findings are summarized, together with the relevance of findings and the exploration of possible future work.

5.1.1 A non-invasive reference-based method for imaging the cerebral metabolic rate of oxygen by PET/MR: theory and error analysis

Driven by the need to avoid invasive arterial sampling while maintaining the ability to quantify CMRO₂ with PET, a reference-based approach was developed to take advantage of hybrid PET/MR scanners. Chapter 2 contains a comprehensive theoretical description of PMRO_x, alongside the evaluation of its sensitivity to errors in the input parameters and to statistical noise. Lastly, an initial assessment of the approach was conducted using human PET-only data. It is important to note that while this assessment cannot address potential issues with the MR techniques, it provided the opportunity to evaluate the influences of RW and CBV in local estimates of the OEF and CMRO₂.

The derivation of the residual functions allows for a detailed understanding of the reference-based technique, with the aim of evaluating conditions in which it might fail. The predicted error associated with neglecting RW and CBV was less than $\pm 10\%$ for most scenarios; however, these contributions are predicted to be significant when the local OEF differs by more than $\pm 25\%$ of the respective WB OEF. For instance, the technique may not be suitable for ischemic stroke, as compensatory increases in OEF as large as 50% have been observed.²¹⁷ However, the reference-based technique is less sensitive to noisy data, which is known to negatively affect voxel-wise fitting routines, indicating that a higher precision can be achieved

with PMROx compared to PET methods. Other advantages include its simplicity and potential ability to detect changes in CMRO₂ due to activation. Lastly, when the method was applied to [¹⁵O]H₂O and [¹⁵O]O₂ PET data from healthy individuals, PMROx resulted in robust OEF and CMRO₂ estimates as demonstrated by the strong agreement between techniques ($R^2 > 0.98$ for all regional measurements).

5.1.2 A non-invasive method for quantifying cerebral metabolic rate of oxygen by hybrid PET/MRI: validation in a porcine model

Chapter 3 presents validation of PMROx in an animal model against a PET-only technique referred to as DBFM,¹¹⁴ in which arterial sampling was performed to measure the AIF. Good agreement between techniques was observed when PMROx used [¹⁵O]H₂O to map CBF (average Pearson correlation coefficient, ρ , = 0.95 for OEF and 0.67 for CMRO₂) and when ASL was used to map CBF (ρ = 0.87 for OEF and ρ = 0.53 for CMRO₂), reducing the PET procedure to [¹⁵O]O₂ inhalation only. PMROx was also shown to be sensitive to anesthetic-induced changes in metabolism (36% reduction in CMRO₂). These experiments highlighted the complexity of the PET-only approach. In particular, measuring the AIF was not possible in three experiments due to issues with the sampling line and population-based AIFs were used instead. The alternative would have been to discard the dataset or repeat the experiment. In contrast, simpler and non-invasive PMROx technique worked in all experiments.

5.1.3 Quantifying cerebral blood flow by a non-invasive PET/MR method of extracting the [¹⁵O]H₂O image-derived input function free of partial volume errors

Chapter 4 presented a PMRFlow method, referred to as PMRFlow_{IDIF}, in which the [¹⁵O]H₂O IDIF was derived from WB TAC that was calibrated by MRI measurements of WB CBF. This approach avoids partial volumes errors that are the primary limitation with conventional methods that attempt to extract the IDIF from carotid arteries. Simulations demonstrated that truncation errors originated by numerically solving the derivative in the IDIF equation can be minimized by resampling the WB TAC to a temporal resolution of 1 ms. In addition, the main source of error was inaccuracies in the WB CBF measurements from MRI. Good agreement was found compared to PET-only CBF images, both visually and quantitatively (average intraclass correlation coefficient of 0.86 and 0.94 for absolute and relative CBF, respectively). The original double integration PMRFlow method (PMRFlow_{DIM}) and PMRFlow_{IDIF} were

applied to [^{15}O]H $_2$ O data from healthy volunteers and produced similar CBF maps ($\rho = 0.995$ and $R^2 = 0.99$). Regional CBF differences were found to be proportional to local-to-WB arterial CBV deviations as predicted by the simulations. Considering these differences were typically less than 10%, the original PMRFlow approach could be implemented in most cases given the technique is fast and does not require fitting. Alternatively, PMRFlow_{IDIF} could be implemented in cases that likely have significant regional vascular alterations, such as resulting from cerebrovascular diseases; however, further studies are needed to confirm these predictions.

5.2 Relevance of findings

Hybrid PET/MR systems allow for complimentary anatomical and functional information from MRI to be acquired during PET imaging. The most obvious advantage is that it avoids alignment errors in image registration since PET and MR images are acquired in the imaging session. PET/MRI also enables functional MR imaging methods to be acquired simultaneously to the PET data, which ensures that imaging data are acquired under the same physiologic condition. In chapters 2 and 3, I exploited this unique ability by proposing a reference-based approach that utilizes complimentary WB CMRO $_2$ MRI measurements acquired simultaneously to [^{15}O]O $_2$ -PET acquisition. This allows PMRO $_x$ to provide fast local OEF and CMRO $_2$ measurements (approx. 5 minutes) by replacing [^{15}O]H $_2$ O-PET acquisition with ASL, which is, again, acquired simultaneously to the [^{15}O]O $_2$ -PET data. Not only PMRO $_x$ is less complex than the gold standard, but it does not require arterial sampling, making it a promising non-invasive technique that could be easily implemented in studies aiming at evaluating cerebral metabolism.

Given the need for an on-site cyclotron and a hybrid PET/MR scanner, it is unlikely that PMRO $_x$ and PMRFlow will be implemented in clinical practice; however, both techniques show a variety of promising applications in research. For instance, these hybrid techniques can be used to better understand the role of cerebral hemodynamics and metabolism in pathologies, which, in turn, could help lead to better treatment options. Another obvious application would be to validate alternative non-invasive MRI methods that would have considerably clinical impact given the ubiquity of MRI.^{107,230} Furthermore, as suggested by the strong agreement to the gold standard in Chapter 2, and confirmed by the validation experiments in Chapter 3, the precision of PMRO $_x$ also allows for longitudinal studies, as well as measuring absolute

changes in $CMRO_2$ with functional activation. This ability makes PMROx a powerful technique to validate blood-oxygen level-dependent MRI-based approaches aimed at tracking functional activation, as well as using baseline $CMRO_2$ from PMROx as a starting point to reduce the experiment complexity. The combination of PMROx and functional MRI for tracking absolute changes in $CMRO_2$ during neuronal activation is discussed in section 5.3.2.

The evaluation of PMROx in Chapters 2 and 3 helped identify the main sources of error, namely neglecting metabolically generated $[^{15}O]H_2O$ and blood-borne activity. Thus, I have started to modify PMROx for future applications involving clinical populations (e.g., cerebrovascular disease) in which these errors may be more significant (section 5.3.1). This approach is similar to the work presented in Chapter 4 showing how PMRFlow could be modified to account for blood-borne signal contributions.

5.3 Future work

The work contained in this thesis provides the basis for a range of further investigations, as described in the next sections.

5.3.1 PMROx_{IDIF}

Although the PMROx technique described in chapters 2 and 3 provided reliable estimates of OEF and $CMRO_2$ in the healthy brain, our error analysis indicates that errors associated with CBV and RW could be greater when the local-to-WB OEF difference exceeds 25%. Large regional differences in OEF and CBV could arise under certain pathologies such as cerebrovascular diseases. Such situations may require an alternative modelling approach to improve the accuracy of PMROx. Analogous to PMRFlow_{IDIF} (Chapter 4), I have previously proposed a PMROx method (PMROx_{IDIF}) that uses MRI estimates of WB CBF and OEF to scale the IDIF derived from WB $[^{15}O]O_2$ -TAC.¹⁹⁹ For this approach, the IDIF for $[^{15}O]O_2$ ($A_o^{IDIF}(t)$, Eq. (5.1)) is obtained from the one-tissue compartment model applied to WB PET data, $C_{wb}^o(t)$.

$$A_o^{IDIF}(t) = \frac{1}{r_1 - r_2} \frac{f_{wb}}{V_{0wb}} \left[\left(\frac{1}{f_{wb}} \frac{dC_{wb}^o(t)}{dt} + \frac{1}{\lambda} C_{wb}^o(t) \right) * (r_1 \cdot e^{r_1 t} - r_2 \cdot e^{r_2 t}) \right] \quad (5.1)$$

$$r_{1,2} = -\frac{f_{wb}}{2V_{0wb}} b_{wb} \pm \sqrt{\left(\frac{f_{wb}}{2V_{0wb}} b_{wb}\right)^2 - \frac{f_{wb}}{V_{0wb}} k} \quad (5.2)$$

where $b_{wb} = (1 - V_{B_{wb}}) E_{wb} - k\Delta t + V_{0wb}/\lambda$ and $V_{0wb} = R_{Hct}(1 - E_{wb}F_v) V_{B_{wb}}$; f_{wb} , E_{wb} and $V_{B_{wb}}$ are the WB CBF, OEF, and CBV, respectively. R_{Hct} is the small-to-large hematocrit ratio ($R_{Hct} = 0.85$)⁹⁴ and F_v the venous-to-total blood volume ratio ($F_v = 0.835$).⁹² The RW component of the input function was assumed to follow a physiologic model described previously:⁹⁶ $A_w^{IDIF}(t) = k \int_0^t A_o(u - \Delta t) du$, where k is the RW generation rate and Δt its appearance delay. The previous equations are similar to the ones derived by Kudomi *et al.*;⁹⁵ however, PMRO_{XIDIF} has less simplifications and one term was added to the Taylor series expansion to account for the RW parameters ($k\Delta t$).

Preliminary analysis was performed on retrospective data collected from an animal model (juvenile pigs, $n = 8$).²²⁹ Briefly, [¹⁵O]H₂O and [¹⁵O]O₂ PET data were acquired on a hybrid PET/MR scanner (3 T Siemens Biograph mMR), together with simultaneous MRI oximetry (OxFlow). Animals were anesthetized with 3% isoflurane and a continuous infusion of propofol (6 mL/kg/h). RW was modeled by species-specific parameters.^{96,98} Measured AIFs were delay- and dispersion-corrected, and the dispersion constant for the [¹⁵O]O₂ AIFs was estimated as 21.3 ± 6.0 s.⁷³ Figure 5.1 shows a comparison between the dispersion-corrected AIFs and the IDIFs, for which the average AUC ratio was 1.04 ± 0.16 (calculated between the IDIFs and the measured AIFs). Preliminary results of WB CMRO₂ estimates obtained with PET-only and PMRO_{XIDIF} were 1.87 ± 0.20 and 1.74 ± 0.27 mL O₂/100g/min, respectively (ns.). Similarly, WB OEF measurements were 0.318 ± 0.119 (PET) and 0.316 ± 0.102 (PMRO_{XIDIF}; ns.). Figure 5.2 presents a comparison between images generated by PET and PMRO_{XIDIF}.

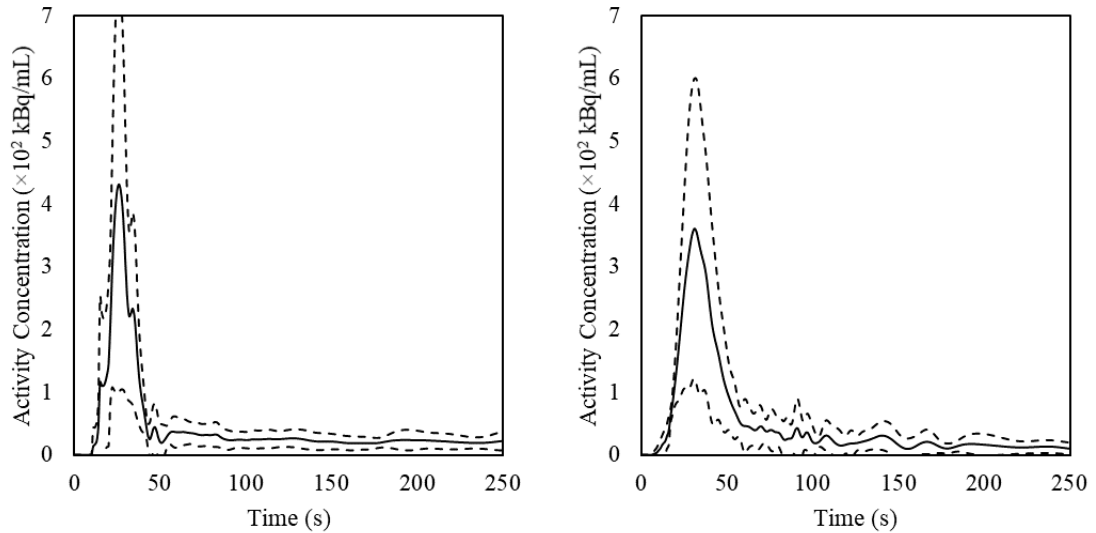


Figure 5.1. $[^{15}\text{O}]\text{O}_2$ AIF and IDIF comparison. Average (solid line) dispersion-corrected AIF (left) and IDIF (right) for $[^{15}\text{O}]\text{O}_2$ ($n = 8$). The dashed lines represent \pm one standard deviation

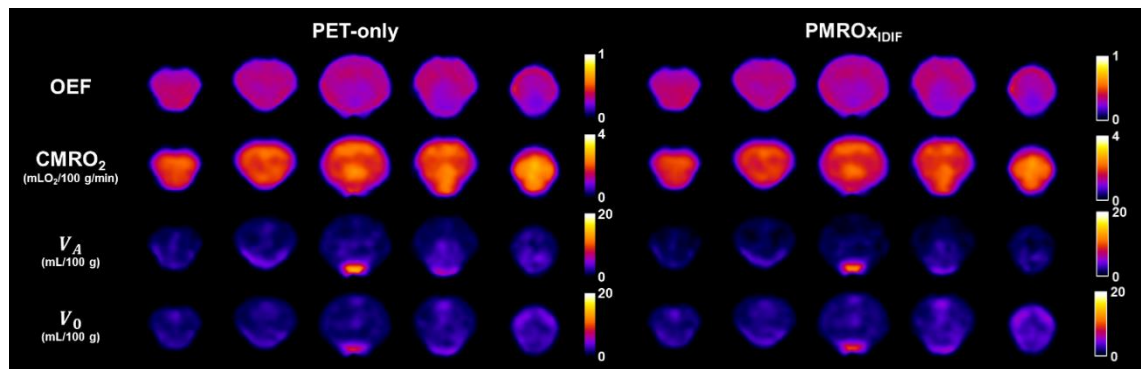


Figure 5.2. Preliminary $\text{PMRO}_{\text{XIDIF}}$ to PET-only comparison. Groupwise ($n = 8$) PET-only images obtained with the measured AIF (left) and corresponding $\text{PMRO}_{\text{XIDIF}}$ maps (right).

The proposed $\text{PMRO}_{\text{XIDIF}}$ approach offers a non-invasive alternative to measure CMRO_2 by incorporating IDIFs obtained by hybrid PET/MRI. The approach is straightforward as it derives the IDIF directly from the high signal-to-noise ratio WB TAC calibrated by the OEF and CBF MRI estimates. Furthermore, it avoids partial volume errors typically encountered when deriving the IDIF from region-of-interest analysis of the feeding arteries. Although the preliminary results in animals are promising, further studies are required to fully validate this approach on a PET/MR scanner in healthy volunteers. Additionally, it would be interesting to investigate the feasibility of implementing both PMRO_x variations on patients with cerebrovascular diseases.

5.3.2 Tracking absolute CMRO₂ changes during neuronal activation

BOLD signal is the basis of functional MRI, in which changes in deoxyhemoglobin concentration in the venous blood affect the transverse relaxation rate. This signal change is characterized by an intricate relationship between CBF, CMRO₂, and the baseline state; consequently, relative changes in CMRO₂ are usually extracted from the fMRI signal by combining changes in CBF measured by ASL. During neuronal activation, CBF increases are typically 2 to 3 times higher than the corresponding increase in CMRO₂.^{142,181} The relationship between the BOLD signal, CMRO₂ and CBF is given by Eq. (5.3).

$$\frac{\Delta\text{BOLD}}{\text{BOLD}_0} = M \left[1 - \left(\frac{\text{CMRO}_2}{\text{CMRO}_{210}} \right)^\beta \left(\frac{\text{CBF}}{\text{CBF}_0} \right)^{\alpha-\beta} \right] \quad (5.3)$$

where the calibration constant M represents the maximum possible BOLD signal increase, α is the constant relating CBV to CBF (i.e., the Grubb relationship), and β is a field-dependent constant that relates deoxyhemoglobin changes to the BOLD signal. The original Grubb relationship ($\alpha = 0.38$)¹⁰⁰ was obtained for total CBV; however, as the increase in CBF during neuronal activation produces an increase in venous CBV, a lower value is usually implemented (e.g., $\alpha = 0.18$).²³³ However, it is not possible to untangle all the physiological parameters involved in the BOLD signal,²³⁴ and the assumption needed for the CBF-CBV coupling have been shown to vary between subjects and brain regions,²³⁵ and may not be valid for pathological conditions or altered physiological states.¹⁸⁰

PET/MRI offers the opportunity to better understand the physiological processes and neurovascular coupling mechanisms that characterize the BOLD signal by using baseline CMRO₂ as reference. Given PMROx is a fast technique (approx. 5 min), CMRO₂ can also be achieved during neuronal activation. These features would also allow for the validation of calibrated fMRI techniques,^{178,179,182–186} as well as to verify key assumptions involved in the BOLD signal. By rearranging Eq. (5.3) and measuring baseline metabolism with PMROx (CMRO₂₁₀), task-induced absolute changes in CMRO₂ can be tracked during neuronal activation as:

$$CMRO_2 = CMRO_{2|0} \left[\left(\frac{CBF}{CBF_0} \right)^{\beta-\alpha} \left(1 - \frac{1}{M} \cdot \frac{\Delta BOLD}{BOLD_0} \right) \right]^{\beta^{-1}} \quad (5.4)$$

where the calibration constant can be obtained with a hypercapnia gas challenge in a calibrated BOLD experiment.¹⁷⁷

5.3.3 Non-invasive quantification of aerobic glycolysis

Despite sufficient oxygen availability to fully metabolize glucose and generate energy, there is additional cerebral glycolysis that is independent of oxygen (i.e., does not undergo phosphorylation).³⁵ If the entirety of energy production is oxidative, the cerebral oxygen-to-glucose consumption ratio is approximately six; thus, non-oxidative glucose metabolism can be estimated by the total-to-oxidative glycolysis difference, defined as aerobic glycolysis (AG, in $\mu mol/100 g/min$; Eq. (5.5)).²³⁶ AG is a hallmark of cancers, often referred to as the Warburg effect,²³⁷ yet it is present in the healthy brain during rest and increases during neuronal activation.^{35,223} In addition, evidence suggests that AG plays an important role in brain development and plasticity.²³⁸ Lastly, studies have reported a non-uniform cerebral distribution of AG and oxygen-to-glucose index (OGI; Eq. (5.6)).^{35,239}

$$AG = CMRGlc - \frac{CMRO_2}{6} \quad (5.5)$$

$$OGI = \frac{CMRO_2}{CMRGlc} \quad (5.6)$$

The gold standard for imaging AG is a lengthy and complex PET method that requires multiple tracers (i.e., [¹⁵O]H₂O for CBF, [¹⁵O]O₂ for OEF and [¹⁵O]CO for CBV, for imaging CMRO₂, and [¹⁸F]FDG, for CMRGlc) and invasive arterial sampling for each tracer. By using hybrid PET/MR, CMRO₂ could be easily obtained with PMROx. This would simplify the original procedure by removing the need for invasive arterial sampling, [¹⁵O]CO PET imaging for measuring CBV, and possibly [¹⁵O]H₂O PET for mapping CBF as well. Moreover, we recently proposed a simultaneous estimation approach to obtain the IDIF from dynamic [¹⁸F]FDG-PET data using later time points from the SSS for scaling (Figure 5.3).²⁴⁰ With the IDIF defined, CMRGlc can be determined by Patlak graphical method,²⁴¹ or by employing a variational

Bayesian method²⁴² (Figure 5.4).²⁴⁰ Thus, AG and OGI can be estimated in a single imaging session by acquiring PET/MR data after a single inhalation of [¹⁵O]O₂ followed by a dynamic [¹⁸F]FDG PET acquisition. These measurements could help elucidate the role of AG in the resting brain, as well as its effect in synaptic plasticity, normal aging, functional activation, and the development of neuro-pathologies.^{35,37}

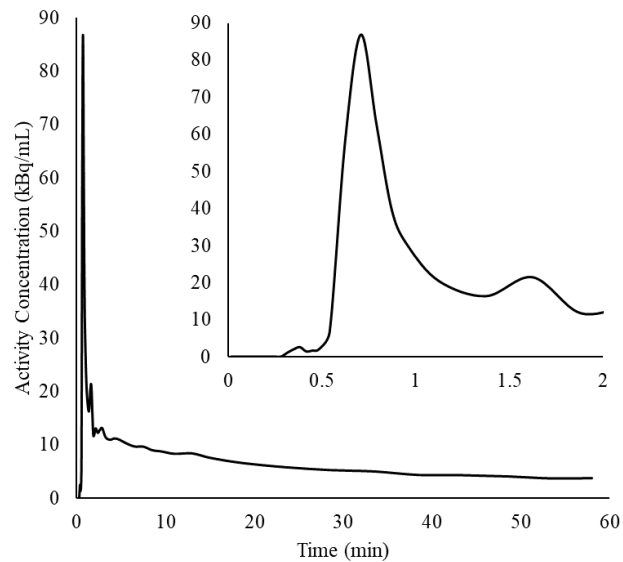


Figure 5.3. A representative IDIF extracted with the simultaneous estimation method. The insert shows the first 2 minutes to better visualize the peak.

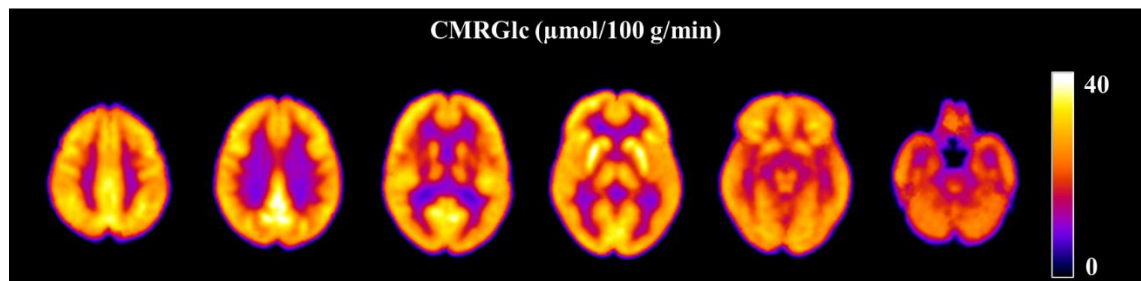


Figure 5.4. CMRGlc maps obtained with the variational Bayesian approach.²⁴⁰ Group-wise CMRGlc maps from healthy individuals ($n = 10$) were obtained using the IDIFs generated with the simultaneous estimation method. PET data were acquired in list-mode for 1 hour after the bolus injection of [¹⁸F]FDG. Images were normalized to the MNI space.

References

1. Gómez-Pinilla F. Brain foods: the effects of nutrients on brain function. *Nat Rev Neurosci* 2008; 9: 568–578.
2. Traystman RJ. Cerebrovascular Anatomy and Hemodynamics. In: Caplan LR, Biller J, Leary MC, et al. (eds) *Primer on Cerebrovascular Diseases*. Elsevier, pp. 5–12.
3. Yang SH, Liu R. Cerebral Autoregulation. In: Caplan LR, Biller J, Leary MC, et al. (eds) *Primer on Cerebrovascular Diseases*. Elsevier, 2017, pp. 57–60.
4. Moerman A, De Hert S. Why and how to assess cerebral autoregulation? *Best Pract Res Clin Anaesthesiol* 2019; 33: 211–220.
5. Willie CK, Tzeng Y-C, Fisher JA, et al. Integrative regulation of human brain blood flow. *J Physiol* 2014; 592: 841–859.
6. Venkat P, Chopp M, Chen J. CBF–Metabolism Coupling. *Prim Cerebrovasc Dis Second Ed* 2017; 67–70.
7. Okazawa H, Kudo T. Clinical impact of hemodynamic parameter measurement for cerebrovascular disease using positron emission tomography and ¹⁵O-labeled tracers. *Ann Nucl Med* 2009; 23: 217–227.
8. Wey H-Y, Desai VR, Duong TQ. A review of current imaging methods used in stroke research. *Neurol Res* 2013; 35: 1092–1102.
9. Lin W, Powers WJ. Oxygen metabolism in acute ischemic stroke. *J Cereb Blood Flow Metab* 2018; 38: 1481–1499.
10. Gupta A, Baradaran H, Schweitzer AD, et al. Oxygen Extraction Fraction and Stroke Risk in Patients with Carotid Stenosis or Occlusion: A Systematic Review and Meta-Analysis. *Am J Neuroradiol* 2014; 35: 250–255.
11. Lee M, Zaharchuk G, Guzman R, et al. Quantitative hemodynamic studies in moyamoya disease. *Neurosurg Focus* 2009; 26: E5.
12. Jansen JFA, van Bussel FCG, van de Haar HJ, et al. Cerebral blood flow, blood supply, and cognition in Type 2 Diabetes Mellitus. *Sci Rep* 2016; 6: 160003.
13. Denier N, Schmidt A, Gerber H, et al. Association of Frontal Gray Matter Volume and Cerebral Perfusion in Heroin Addiction: A Multimodal Neuroimaging Study. *Front Psychiatry*; 4. Epub ahead of print 2013. DOI: 10.3389/fpsy.2013.00135.
14. Christen T, Lemasson B, Pannetier N, et al. Is T2* Enough to Assess Oxygenation? Quantitative Blood Oxygen Level–Dependent Analysis in Brain Tumor. *Radiology* 2012; 262: 495–502.
15. Ahmad A, Patel V, Xiao J, et al. The Role of Neurovascular System in Neurodegenerative Diseases. *Mol Neurobiol* 2020; 57: 4373–4393.
16. Zhang H, Wang Y, Lyu D, et al. Cerebral blood flow in mild cognitive impairment and Alzheimer’s disease: A systematic review and meta-analysis. *Ageing Res Rev* 2021; 71: 101450.
17. Kisler K, Nelson AR, Montagne A, et al. Cerebral blood flow regulation and

- neurovascular dysfunction in Alzheimer disease. *Nat Rev Neurosci* 2017; 18: 419–434.
18. Pelizzari L, Laganà MM, Di Tella S, et al. Combined Assessment of Diffusion Parameters and Cerebral Blood Flow Within Basal Ganglia in Early Parkinson's Disease. *Front Aging Neurosci*; 11. Epub ahead of print 4 June 2019. DOI: 10.3389/fnagi.2019.00134.
 19. Ssali T, Anazodo UC, Narciso L, et al. Sensitivity of Arterial Spin Labeling for Characterization of Longitudinal Perfusion Changes in Frontotemporal Dementia and Related Disorders. *NeuroImage Clin* 2021; 102853.
 20. Binnewijzend MAA, Kuijer JPA, van der Flier WM, et al. Distinct perfusion patterns in Alzheimer's disease, frontotemporal dementia and dementia with Lewy bodies. *Eur Radiol* 2014; 24: 2326–2333.
 21. An H, Liu Q, Chen Y, et al. Evaluation of MR-Derived Cerebral Oxygen Metabolic Index in Experimental Hyperoxic Hypercapnia, Hypoxia, and Ischemia. *Stroke* 2009; 40: 2165–2172.
 22. Touzani O, Young AR, Derlon J-M, et al. Progressive impairment of brain oxidative metabolism reversed by reperfusion following middle cerebral artery occlusion in anaesthetized baboons. *Brain Res* 1997; 767: 17–25.
 23. Lee J-M, Vo KD, An H, et al. Magnetic resonance cerebral metabolic rate of oxygen utilization in hyperacute stroke patients. *Ann Neurol* 2003; 53: 227–232.
 24. Derdeyn CP, Videen TO, Yundt KD, et al. Variability of cerebral blood volume and oxygen extraction: stages of cerebral haemodynamic impairment revisited. *Brain* 2002; 125: 595–607.
 25. An H, Ford AL, Chen Y, et al. Defining the Ischemic Penumbra Using Magnetic Resonance Oxygen Metabolic Index. *Stroke* 2015; 46: 982–988.
 26. Kaku Y, Iihara K, Nakajima N, et al. Cerebral blood flow and metabolism of hyperperfusion after cerebral revascularization in patients with moyamoya disease. *J Cereb Blood Flow Metab* 2012; 32: 2066–2075.
 27. Marchal G, Beaudouin V, Rioux P, et al. Prolonged persistence of substantial volumes of potentially viable brain tissue after stroke: A correlative PET-CT study with voxel-based data analysis. *Stroke*. Epub ahead of print 1996. DOI: 10.1161/01.STR.27.4.599.
 28. Kuroda S, Kashiwazaki D, Houkin K. Abstract W P101: Surgical Revascularization Reverses Decreased Cerebral Oxygen Metabolism in Young Patients with Moyamoya Disease. *Stroke*; 45. Epub ahead of print February 2014. DOI: 10.1161/str.45.suppl_1.wp101.
 29. Kuroda S, Kashiwazaki D, Hirata K, et al. Effects of Surgical Revascularization on Cerebral Oxygen Metabolism in Patients With Moyamoya Disease. *Stroke* 2014; 45: 2717–2721.
 30. Baron JC, Jones T. Oxygen metabolism, oxygen extraction and positron emission tomography: Historical perspective and impact on basic and clinical neuroscience. *Neuroimage* 2012; 61: 492–504.
 31. Hokari M, Kuroda S, Shiga T, et al. Impact of oxygen extraction fraction on long-term

- prognosis in patients with reduced blood flow and vasoreactivity because of occlusive carotid artery disease. *Surg Neurol* 2009; 71: 532–538.
32. Yamauchi H, Fukuyama H, Nagahama Y, et al. Significance of increased oxygen extraction fraction in five-year prognosis of major cerebral arterial occlusive diseases. *J Nucl Med* 1999; 40: 1992–8.
 33. Fox PT, Raichle ME. Focal physiological uncoupling of cerebral blood flow and oxidative metabolism during somatosensory stimulation in human subjects. *Proc Natl Acad Sci* 1986; 83: 1140–1144.
 34. Fox PT, Raichle ME, Mintun MA, et al. Nonoxidative glucose consumption during focal physiologic neural activity. *Science* (80-) 1988; 241: 462–464.
 35. Vaishnavi SN, Vlassenko AG, Rundle MM, et al. Regional aerobic glycolysis in the human brain. *Proc Natl Acad Sci U S A* 2010; 107: 17757–62.
 36. Goyal MS, Vlassenko AG, Blazey TM, et al. Loss of Brain Aerobic Glycolysis in Normal Human Aging. *Cell Metab* 2017; 26: 353-360.e3.
 37. Vlassenko AG, Gordon BA, Goyal MS, et al. Aerobic glycolysis and tau deposition in preclinical Alzheimer's disease. *Neurobiol Aging* 2018; 67: 95–98.
 38. Kety SS, Schmidt CF. The determination of cerebral blood flow in man by the use of nitrous oxide in low concentrations. *Am J Physiol Content* 1945; 143: 53–66.
 39. Kety SS, Schmidt CF. The nitrous oxide method for the quantitative determination of cerebral blood flow in man: theory, procedure and normal values. *J Clin Invest* 1947; 476–483.
 40. Kety SS, Schmidt CF. The effects of altered arterial tensions of carbon dioxide and oxygen on cerebral blood flow and cerebral oxygen consumption of normal young men. *J Clin Invest* 1948; 27: 484–492.
 41. Grubb RL, Raichle ME, Eichling JO, et al. The effects of changes in PaCO₂ cerebral blood volume, blood flow, and vascular mean transit time. *Stroke* 1974; 5: 630–639.
 42. Reivich M. Arterial PCO₂ and cerebral hemodynamics. *Am J Physiol Content* 1964; 206: 25–35.
 43. Smith AL, Neufeld GR, Ominsky AJ, et al. Effect of arterial CO₂ tension on cerebral blood flow, mean transit time, and vascular volume. *J Appl Physiol* 1971; 31: 701–707.
 44. Eichling JO, Raichle ME, Grubb RL, et al. In vivo determination of cerebral blood volume with radioactive oxygen-15 in the monkey. *Circ Res* 1975; 37: 707–14.
 45. Ito H, Kanno I, Shimosegawa E, et al. Hemodynamic changes during neural deactivation in human brain: A positron emission tomography study of crossed cerebellar diaschisis. *Ann Nucl Med* 2002; 16: 249–254.
 46. Welch MJ, Ter-Pogossian MM. Preparation of short half-lived radioactive gases for medical studies. *Radiat Res* 1968; 36: 580.
 47. Ter-Pogossian MM, Eichling JO, Davis DO, et al. The determination of regional cerebral blood flow by means of water labeled with radioactive oxygen-15. *Radiology* 1969; 93: 31–40.

48. Ter-Pogossian MM, Eichling JO, Davis DO, et al. The measure in vivo of regional cerebral oxygen utilization by means of oxyhemoglobin labelled with radioactive oxygen-15. *J Clin Invest* 1970; 49: 381–391.
49. Lenzi GL, Jones T, McKenzie CG, et al. Study of regional cerebral metabolism and blood flow relationships in man using the method of continuously inhaling oxygen-15 and oxygen-15 labelled carbon dioxide. *J Neurol Neurosurg Psychiatry* 1978; 41: 1–10.
50. Jones T, Chesler DA, Ter-Pogossian MM. The continuous inhalation of oxygen-15 for assessing regional oxygen extraction in the brain of man. *Br J Radiol* 1976; 49: 339–343.
51. Subramanyam R, Alpert NM, Hoop B, et al. A model for regional cerebral oxygen distribution during continuous inhalation of $^{15}\text{O}_2$, C^{15}O , and C^{15}O_2 . *J Nucl Med* 1978; 19: 48–53.
52. Iida H, Iguchi S, Teramoto N, et al. Adequacy of a compartment model for CMRO₂ quantitation using ^{15}O -labeled oxygen and PET: a clearance measurement of ^{15}O -radioactivity following intracarotid bolus injection of ^{15}O -labeled oxyhemoglobin on macaca fascicularis. *J Cereb Blood Flow Metab* 2014; 34: 1434–1439.
53. Phelps ME. Emission computed tomography. *Semin Nucl Med* 1977; 7: 337–365.
54. Frackowiak RS, Jones T, Lenzi GL, et al. Regional cerebral oxygen utilization and blood flow in normal man using oxygen-15 and positron emission tomography. *Acta Neurol Scand* 1980; 62: 336–344.
55. Lammertsma AA, Jones T, Frackowiak RSJ, et al. A theoretical study of the steady-state model for measuring regional cerebral blood flow and oxygen utilisation using oxygen-15. *Journal of Computer Assisted Tomography* 1981; 5: 544.
56. Lammertsma AA, Heather JD, Jones T, et al. A statistical study of the steady state technique for measuring regional cerebral blood flow and oxygen utilisation using ^{15}O . *J Comput Assist Tomogr* 1982; 6: 566–573.
57. Altman DI, Lich LL, Powers WJ. Brief inhalation method to measure cerebral oxygen extraction fraction with PET: accuracy determination under pathologic conditions. *J Nucl Med* 1991; 32: 1738–41.
58. Herscovitch P, Raichle ME. Effect of tissue heterogeneity on the measurement of cerebral blood flow with the equilibrium C^{15}O_2 inhalation technique. *J Cereb Blood Flow Metab* 1983; 3: 407–415.
59. Kostakoglu L, Agress H, Goldsmith SJ. Clinical Role of FDG PET in Evaluation of Cancer Patients. *RadioGraphics* 2003; 23: 315–340.
60. Davison CM, O’Brien JT. A comparison of FDG-PET and blood flow SPECT in the diagnosis of neurodegenerative dementias: a systematic review. *Int J Geriatr Psychiatry* 2014; 29: 551–561.
61. Cherry SR, Sorenson JA, Phelps ME. *Physics in Nuclear Medicine*. 4th ed. Philadelphia, PA: Elsevier Science & Technology Books, 2012.
62. Levin CS, Hoffman EJ. Calculation of positron range and its effect on the fundamental limit of positron emission tomography system spatial resolution. *Phys Med Biol* 1999;

- 44: 781–799.
63. Carson RE. Tracer Kinetic Modeling in PET. In: Bailey DL, Townsend DW, Valk PE, et al. (eds) *Positron Emission Tomography*. London: Springer, pp. 127–159.
 64. Schmidt KC, Turkheimer FE. Kinetic modeling in positron emission tomography. *Q J Nucl Med* 2002; 46: 70–85.
 65. Herscovitch P, Markham J, Raichle ME. Brain blood flow measured with intravenous H₂(15)O. I. Theory and error analysis. *J Nucl Med* 1983; 24: 782–9.
 66. Raichle ME, Martin WR, Herscovitch P, et al. Brain blood flow measured with intravenous H₂(15)O. II. Implementation and validation. *J Nucl Med* 1983; 24: 790–8.
 67. Herscovitch P, Raichle ME. What is the correct value for the brain-blood partition coefficient for water? *J Cereb Blood Flow Metab* 1985; 5: 65–69.
 68. Narciso L, Ssali T, Iida H, et al. A non-invasive reference-based method for imaging the cerebral metabolic rate of oxygen by PET/MR: theory and error analysis. *Phys Med Biol* 2021; 66: 065009.
 69. Kudomi N, Hayashi T, Teramoto N, et al. Rapid quantitative measurement of CMRO₂ and CBF by dual administration of 15O-labeled oxygen and water during a single PET scan - A validation study and error analysis in anesthetized monkeys. *J Cereb Blood Flow Metab* 2005; 25: 1209–1224.
 70. Iida H, Kanno I, Miura S, et al. Error analysis of a quantitative cerebral blood flow measurement using H₂15O autoradiography and positron emission tomography, with respect to the dispersion of the input function. *J Cereb Blood Flow Metab* 1986; 6: 536–545.
 71. Kanno I, Iida H, Miura S, et al. A system for cerebral blood flow measurement using an H₂15O autoradiographic method and positron emission tomography. *J Cereb Blood Flow Metab* 1987; 7: 143–153.
 72. Iida H, Higano S, Tomura N, et al. Evaluation of regional differences of tracer appearance time in cerebral tissues using [15O]water and dynamic positron emission tomography. *J Cereb Blood Flow Metab* 1988; 8: 285–288.
 73. Meyer E. Simultaneous correction for tracer arrival delay and dispersion in CBF measurements by the H₂15O autoradiographic method and dynamic PET. *J Nucl Med* 1989; 30: 1069–78.
 74. Iida H, Miura S, Shoji Y, et al. Noninvasive quantitation of cerebral blood flow using oxygen-15-water and a dual-PET system. *J Nucl Med* 1998; 39: 1789–98.
 75. Jochimsen TH, Zeisig V, Schulz J, et al. Fully automated calculation of image-derived input function in simultaneous PET/MRI in a sheep model. *EJNMMI Phys*; 3. Epub ahead of print 2016. DOI: 10.1186/s40658-016-0139-2.
 76. Vestergaard MB, Calvo OP, Hansen AE, et al. Validation of kinetic modeling of [15O]H₂O PET using an image derived input function on hybrid PET/MRI. *Neuroimage* 2021; 233: 117950.
 77. Kuttner S, Wickstrøm KK, Lubberink M, et al. Cerebral blood flow measurements with

- 15O-water PET using a non-invasive machine-learning-derived arterial input function. *J Cereb Blood Flow Metab*. Epub ahead of print 2021. DOI: 10.1177/0271678X21991393.
78. Khalighi MM, Deller TW, Fan AP, et al. Image-derived input function estimation on a TOF-enabled PET/MR for cerebral blood flow mapping. *J Cereb Blood Flow Metab* 2018; 38: 126–135.
 79. Kudomi N, Maeda Y, Yamamoto Y, et al. Reconstruction of an input function from a dynamic PET water image using multiple tissue curves. *Phys Med Biol* 2016; 61: 5755–5767.
 80. Fung EK, Carson RE. Cerebral blood flow with [15O]water PET studies using an image-derived input function and MR-defined carotid centerlines. *Phys Med Biol* 2013; 58: 1903–1923.
 81. Su Y, Arbelaez AM, Benzinger TLS, et al. Noninvasive estimation of the arterial input function in positron emission tomography imaging of cerebral blood flow. *J Cereb Blood Flow Metab* 2013; 33: 115–121.
 82. Su Y, Vlassenko AG, Couture LE, et al. Quantitative hemodynamic PET imaging using image-derived arterial input function and a PET/MR hybrid scanner. *J Cereb Blood Flow Metab* 2017; 37: 1435–1446.
 83. Islam MM, Tsujikawa T, Mori T, et al. Estimation of arterial input by a noninvasive image derived method in brain H215O PET study: Confirmation of arterial location using MR angiography. *Phys Med Biol* 2017; 62: 4514–4524.
 84. Treyer V, Jobin M, Burger C, et al. Quantitative cerebral H2 15O perfusion PET without arterial blood sampling, a method based on washout rate. *Eur J Nucl Med Mol Imaging* 2003; 30: 572–580.
 85. Iguchi S, Hori Y, Moriguchi T, et al. Verification of a semi-automated MRI-guided technique for non-invasive determination of the arterial input function in 15O-labeled gaseous PET. *Nucl Instruments Methods Phys Res Sect A Accel Spectrometers, Detect Assoc Equip* 2013; 702: 111–113.
 86. Mejia MA, Itoh M, Watabe H, et al. Simplified nonlinearity correction of oxygen-15-water regional cerebral blood flow images without blood sampling. *J Nucl Med* 1994; 35: 1870–7.
 87. Watabe H, Itoh M, Cunningham V, et al. Noninvasive quantification of rCBF using positron emission tomography. *J Cereb Blood Flow Metab* 1996; 16: 311–319.
 88. Ssali T, Anazodo UC, Thiessen JD, et al. A Noninvasive Method for Quantifying Cerebral Blood Flow by Hybrid PET/MRI. *J Nucl Med* 2018; 59: 1329–1334.
 89. Koopman T, Yaqub M, Heijtel DFR, et al. Semi-quantitative cerebral blood flow parameters derived from non-invasive [15 O]H 2 O PET studies. *J Cereb Blood Flow Metab* 2019; 39: 163–172.
 90. Ishii Y, Thamm T, Guo J, et al. Simultaneous phase-contrast MRI and PET for noninvasive quantification of cerebral blood flow and reactivity in healthy subjects and patients with cerebrovascular disease. *J Magn Reson Imaging* 2019; 1–12.

91. Ohta S, Meyer E, Thompson CJ, et al. Oxygen consumption of the living human brain measured after a single inhalation of positron emitting oxygen. *J Cereb Blood Flow Metab* 1992; 12: 179–192.
92. Mintun MA, Raichle ME, Martin WR, et al. Brain oxygen utilization measured with O-15 radiotracers and positron emission tomography. *J Nucl Med* 1984; 25: 177–87.
93. Lammertsma AA, Jones T. Correction for the presence of intravascular oxygen-15 in the steady-state technique for measuring regional oxygen extraction ratio in the brain: 1. Description of the method. *J Cereb Blood Flow Metab* 1983; 3: 416–424.
94. Phelps ME, Huang SC, Hoffman EJ, et al. Validation of tomographic measurement of cerebral blood volume with C-11-labeled carboxyhemoglobin. *J Nucl Med* 1979; 20: 328–34.
95. Kudomi N, Maeda Y, Yamamoto H, et al. Reconstruction of input functions from a dynamic PET image with sequential administration of $^{15}\text{O}_2$ and H_2^{15}O for noninvasive and ultra-rapid measurement of CBF, OEF, and CMRO₂. *J Cereb Blood Flow Metab* 2018; 38: 780–792.
96. Iida H, Jones T, Miura S. Modeling approach to eliminate the need to separate arterial plasma in oxygen-15 inhalation positron emission tomography. *J Nucl Med* 1993; 34: 1333–40.
97. Huang SC, Barrio JR, Yu D, et al. Modelling approach for separating blood time activity curves in positron emission tomographic studies. *Phys Med Biol* 1991; 36: 749–761.
98. Kudomi N, Hayashi T, Watabe H, et al. A physiologic model for recirculation water correction in CMRO₂ assessment with $^{15}\text{O}_2$ inhalation PET. *J Cereb Blood Flow Metab* 2009; 29: 355–364.
99. Shidahara M, Watabe H, Kim KM, et al. Evaluation of a commercial PET tomograph-based system for the quantitative assessment of rCBF, rOEF and rCMRO₂ by using sequential administration of ^{15}O -labeled compounds. *Ann Nucl Med* 2002; 16: 317–327.
100. Grubb Jr. RL, Raichle ME, Higgins CS, et al. Measurement of regional cerebral blood volume by emission tomography. *Ann Neurol* 1978; 4: 322–328.
101. Ladurner G, Zilkha E, Iliff D, et al. Measurement of regional cerebral blood volume by computerized axial tomography. *J Neurol Neurosurg Psychiatry* 1976; 39: 152–158.
102. Penn R, Walser R, Ackerman L. Cerebral blood volume in man: computer analysis of a computerized brain scan. *JAMA* 1975; 234: 1154.
103. Mathew NT, Meyer JS, Bell RL, et al. Regional cerebral blood flow and blood volume measured with the gamma camera. *Neuroradiology* 1972; 4: 133–140.
104. Kuhl DE, Reivich M, Alavi A, et al. Local cerebral blood volume determined by three dimensional reconstruction of radionuclide scan data. *Circ Res* 1975; 36: 610–619.
105. Hatazawa J, Fujita H, Kanno I, et al. Regional cerebral blood flow, blood volume, oxygen extraction fraction, and oxygen utilization rate in normal volunteers measured by the autoradiographic technique and the single breath inhalation method. *Ann Nucl Med* 1995; 9: 15–21.

106. Mintun M a, Lundstrom BN, Snyder a Z, et al. Blood flow and oxygen delivery to human brain during functional activity: theoretical modeling and experimental data. *Proc Natl Acad Sci U S A* 2001; 98: 6859–6864.
107. Fan AP, Jahanian H, Holdsworth SJ, et al. Comparison of cerebral blood flow measurement with [15 O]-water positron emission tomography and arterial spin labeling magnetic resonance imaging: A systematic review. *J Cereb Blood Flow Metab* 2016; 36: 842–861.
108. Fan AP, An H, Moradi F, et al. Quantification of brain oxygen extraction and metabolism with [15O]-gas PET: A technical review in the era of PET/MRI. *Neuroimage* 2020; 220: 117136.
109. Coles JP, Fryer TD, Bradley PG, et al. Intersubject Variability and Reproducibility of 15 O PET Studies. *J Cereb Blood Flow Metab* 2006; 26: 48–57.
110. Carroll TJ, Teneggi V, Jobin M, et al. Absolute Quantification of Cerebral Blood Flow with Magnetic Resonance, Reproducibility of the Method, and Comparison with H 2 15 O Positron Emission Tomography. *J Cereb Blood Flow Metab* 2002; 22: 1149–1156.
111. Bremner JP, Van Berckel BNM, Persoon S, et al. Day-to-day test-retest variability of CBF, CMRO₂, and OEF measurements using dynamic 15O PET studies. *Mol Imaging Biol* 2011; 13: 759–768.
112. Ito H, Kanno I, Kato C, et al. Database of normal human cerebral blood flow, cerebral blood volume, cerebral oxygen extraction fraction and cerebral metabolic rate of oxygen measured by positron emission tomography with 15 O-labelled carbon dioxide or water, carbon monoxide and oxygen: *Eur J Nucl Med Mol Imaging* 2004; 31: 635–643.
113. Kudomi N, Watabe H, Hayashi T, et al. Separation of input function for rapid measurement of quantitative CMRO₂ and CBF in a single PET scan with a dual tracer administration method. *Phys Med Biol* 2007; 52: 1893–1908.
114. Kudomi N, Hirano Y, Koshino K, et al. Rapid quantitative CBF and CMRO₂ measurements from a single PET scan with sequential administration of dual 15O-labeled tracers. *J Cereb Blood Flow Metab* 2013; 33: 440–448.
115. Detre JA, Leigh JS, Williams DS, et al. Perfusion imaging. *Magn Reson Med* 1992; 23: 37–45.
116. Alsop DC, Detre JA, Golay X, et al. Recommended implementation of arterial spin-labeled perfusion MRI for clinical applications: A consensus of the ISMRM perfusion study group and the European consortium for ASL in dementia. *Magn Reson Med* 2015; 73: 102–116.
117. Lanzman B, Heit JJ. Advanced MRI Measures of Cerebral Perfusion and Their Clinical Applications. *Top Magn Reson Imaging* 2017; 26: 83–90.
118. Quarles CC, Bell LC, Stokes AM. Imaging vascular and hemodynamic features of the brain using dynamic susceptibility contrast and dynamic contrast enhanced MRI. *Neuroimage* 2019; 187: 32–55.
119. Wahsner J, Gale EM, Rodríguez-Rodríguez A, et al. Chemistry of MRI Contrast Agents: Current Challenges and New Frontiers. *Chem Rev* 2019; 119: 957–1057.

120. Tang J, Sheng Y, Hu H, et al. Macromolecular MRI contrast agents: Structures, properties and applications. *Prog Polym Sci* 2013; 38: 462–502.
121. Nayak KS, Nielsen J-F, Bernstein MA, et al. Cardiovascular magnetic resonance phase contrast imaging. *J Cardiovasc Magn Reson* 2015; 17: 71.
122. Henriksen OM, Larsson HBW, Hansen AE, et al. Estimation of intersubject variability of cerebral blood flow measurements using MRI and positron emission tomography. *J Magn Reson Imaging* 2012; 35: 1290–1299.
123. Sakhare AR, Barisano G, Pa J. Assessing test–retest reliability of phase contrast MRI for measuring cerebrospinal fluid and cerebral blood flow dynamics. *Magn Reson Med* 2019; 82: 658–670.
124. Liu P, Qi Y, Lin Z, et al. Assessment of cerebral blood flow in neonates and infants: A phase-contrast MRI study. *Neuroimage* 2019; 185: 926–933.
125. Leijenaar JF, Maurik IS, Kuijter JPA, et al. Lower cerebral blood flow in subjects with Alzheimer’s dementia, mild cognitive impairment, and subjective cognitive decline using two-dimensional phase-contrast magnetic resonance imaging. *Alzheimer’s Dement Diagnosis, Assess Dis Monit* 2017; 9: 76–83.
126. Puig O, Vestergaard MB, Lindberg U, et al. Phase contrast mapping MRI measurements of global cerebral blood flow across different perfusion states – A direct comparison with ¹⁵O-H₂O positron emission tomography using a hybrid PET/MR system. *J Cereb Blood Flow Metab* 2019; 39: 2368–2378.
127. Peng SL, Su P, Wang FN, et al. Optimization of phase-contrast MRI for the quantification of whole-brain cerebral blood flow. *J Magn Reson Imaging* 2015; 42: 1126–1133.
128. Nederveen AJ, Avril S, Speelman L. MRI strain imaging of the carotid artery: Present limitations and future challenges. *J Biomech* 2014; 47: 824–833.
129. Vestergaard MB, Lindberg U, Aachmann-Andersen NJ, et al. Comparison of global cerebral blood flow measured by phase-contrast mapping MRI with ¹⁵O-H₂O positron emission tomography. *J Magn Reson Imaging* 2017; 45: 692–699.
130. Lu H, Clingman C, Golay X, et al. Determining the longitudinal relaxation time (T₁) of blood at 3.0 Tesla. *Magn Reson Med* 2004; 52: 679–682.
131. Bokkers RPH, Bremmer JP, Berckel BNM Van, et al. Arterial Spin Labeling Perfusion MRI at Multiple Delay Times: A Correlative Study with H₂¹⁵O Positron Emission Tomography in Patients with Symptomatic Carotid Artery Occlusion. *J Cereb Blood Flow Metab* 2010; 30: 222–229.
132. Heijtel DFR, Mutsaerts HJMM, Bakker E, et al. Accuracy and precision of pseudo-continuous arterial spin labeling perfusion during baseline and hypercapnia: A head-to-head comparison with ¹⁵O H₂O positron emission tomography. *Neuroimage* 2014; 92: 182–192.
133. Zhang K, Herzog H, Mauler J, et al. Comparison of cerebral blood flow acquired by simultaneous [¹⁵O]water positron emission tomography and arterial spin labeling magnetic resonance imaging. *J Cereb Blood Flow Metab* 2014; 34: 1373–1380.

134. Fan AP, Guo J, Khalighi MM, et al. Long-Delay Arterial Spin Labeling Provides More Accurate Cerebral Blood Flow Measurements in Moyamoya Patients: A Simultaneous Positron Emission Tomography/MRI Study. *Stroke* 2017; 48: 2441–2449.
135. van Golen LW, Kuijer JPA, Huisman MC, et al. Quantification of Cerebral Blood Flow in Healthy Volunteers and Type 1 Diabetic Patients : Comparison of MRI Arterial Spin Labeling and [15O]H₂O Positron Emission Tomography (PET). 2014; 1309: 1300–1309.
136. Puig O, Henriksen OM, Vestergaard MB, et al. Comparison of simultaneous arterial spin labeling MRI and 15O-H₂O PET measurements of regional cerebral blood flow in rest and altered perfusion states. *J Cereb Blood Flow Metab* 2020; 40: 1621–1633.
137. Fahlström M, Appel L, Kumlien E, et al. Evaluation of arterial spin labeling mri—comparison with 15 o-water pet on an integrated pet/mr scanner. *Diagnostics*; 11. Epub ahead of print 2021. DOI: 10.3390/diagnostics11050821.
138. Chappell MA, McConnell FAK, Golay X, et al. Partial volume correction in arterial spin labeling perfusion MRI: A method to disentangle anatomy from physiology or an analysis step too far? *Neuroimage*; 238. Epub ahead of print 2021. DOI: 10.1016/j.neuroimage.2021.118236.
139. Zhao MY, Fan AP, Chen DYT, et al. Cerebrovascular reactivity measurements using simultaneous 15O-water PET and ASL MRI: Impacts of arterial transit time, labeling efficiency, and hematocrit. *Neuroimage* 2021; 233: 117955.
140. Wu WC, St Lawrence KS, Licht DJ, et al. Quantification issues in arterial spin labeling perfusion magnetic resonance imaging. *Top Magn Reson Imaging* 2010; 21: 65–73.
141. Chen Y, Wang DJJ, Detre JA. Test-retest reliability of arterial spin labeling with common labeling strategies. *J Magn Reson Imaging* 2011; 33: 940–949.
142. Rodgers ZB, Detre JA, Wehrli FW. MRI-based methods for quantification of the cerebral metabolic rate of oxygen. *J Cereb Blood Flow Metab* 2016; 36: 1165–1185.
143. Wright GA, Hu BS, Macovski A. Estimating oxygen saturation of blood in vivo with MR imaging at 1.5 T. *J Magn Reson Imaging* 1991; 1: 275–283.
144. Jiang D, Deng S, Franklin CG, et al. Validation of T₂-based oxygen extraction fraction measurement with 15O positron emission tomography. *Magn Reson Med* 2020; 85: 290–297.
145. Lu H, Ge Y. Quantitative evaluation of oxygenation in venous vessels using T₂-relaxation-under-spin-tagging MRI. *Magn Reson Med* 2008; 60: 357–363.
146. Miao X, Nayak KS, Wood JC. In vivo validation of T₂- and susceptibility-based SvO₂ measurements with jugular vein catheterization under hypoxia and hypercapnia. *Magn Reson Med* 2019; 82: 2188–2198.
147. Lu H, Xu F, Grgac K, et al. Calibration and validation of TRUST MRI for the estimation of cerebral blood oxygenation. *Magn Reson Med* 2012; 67: 42–49.
148. Haacke EM, Lai S, Reichenbach JR, et al. In vivo measurement of blood oxygen saturation using magnetic resonance imaging: a direct validation of the blood oxygen level-dependent concept in functional brain imaging. *Hum Brain Mapp* 1997; 5: 341–

- 346.
149. Fernández-Seara MA, Techawiboonwong A, Detre JA, et al. MR susceptometry for measuring global brain oxygen extraction. *Magn Reson Med* 2006; 55: 967–973.
 150. Severinghaus JW. Simple, accurate equations for human blood O₂ dissociation computations. *J Appl Physiol* 1979; 46: 599–602.
 151. Rodgers ZB, Englund EK, Langham MC, et al. Rapid T₂- and susceptometry-based CMRO₂ quantification with interleaved TRUST (iTRUST). *Neuroimage* 2015; 106: 441–450.
 152. Barhoum S, Langham MC, Magland JF, et al. Method for rapid MRI quantification of global cerebral metabolic rate of oxygen. *J Cereb Blood Flow Metab* 2015; 35: 1616–1622.
 153. Jain V, Langham MC, Wehrli FW. MRI Estimation of Global Brain Oxygen Consumption Rate. *J Cereb Blood Flow Metab* 2010; 30: 1598–1607.
 154. Wehrli FW, Rodgers ZB, Jain V, et al. Time-resolved MRI oximetry for quantifying CMRO₂ and vascular reactivity. *Acad Radiol* 2014; 21: 207–214.
 155. Liu C, Wei H, Gong N-J, et al. Quantitative Susceptibility Mapping: Contrast Mechanisms and Clinical Applications. *Tomography* 2015; 1: 3–17.
 156. Wang Y, Liu T. Quantitative susceptibility mapping (QSM): Decoding MRI data for a tissue magnetic biomarker. *Magn Reson Med* 2015; 73: 82–101.
 157. Zhang J, Zhou D, Nguyen TD, et al. Cerebral metabolic rate of oxygen (CMRO₂) mapping with hyperventilation challenge using quantitative susceptibility mapping (QSM). *Magn Reson Med* 2017; 77: 1762–1773.
 158. Fan AP, Evans KC, Stout JN, et al. Regional quantification of cerebral venous oxygenation from MRI susceptibility during hypercapnia. *Neuroimage* 2015; 104: 146–155.
 159. Kudo K, Liu T, Murakami T, et al. Oxygen extraction fraction measurement using quantitative susceptibility mapping: Comparison with positron emission tomography. *J Cereb Blood Flow Metab* 2016; 36: 1424–1433.
 160. Uwano I, Kudo K, Sato R, et al. Noninvasive Assessment of Oxygen Extraction Fraction in Chronic Ischemia Using Quantitative Susceptibility Mapping at 7 Tesla. *Stroke* 2017; 48: 2136–2141.
 161. Robinson SD, Bredies K, Khabipova D, et al. An illustrated comparison of processing methods for MR phase imaging and QSM: combining array coil signals and phase unwrapping. *NMR Biomed* 2017; 30: e3601.
 162. Kee Y, Liu Z, Zhou L, et al. Quantitative Susceptibility Mapping (QSM) Algorithms: Mathematical Rationale and Computational Implementations. *IEEE Trans Biomed Eng* 2017; 64: 2531–2545.
 163. Schweser F, Robinson SD, de Rochefort L, et al. An illustrated comparison of processing methods for phase MRI and QSM: removal of background field contributions from sources outside the region of interest. *NMR Biomed* 2017; 30: e3604.

164. Thulborn KR, Waterton JC, Matthews PM, et al. Oxygenation dependence of the transverse relaxation time of water protons in whole blood at high field. *Biochim Biophys Acta - Gen Subj* 1982; 714: 265–270.
165. Davis TL, Kwong KK, Weisskoff RM, et al. Calibrated functional MRI: Mapping the dynamics of oxidative metabolism. *Proc Natl Acad Sci* 1998; 95: 1834–1839.
166. Narciso L, Ssali T, Liu L, et al. Validation of OxFlow Measurements of Whole-Brain CBF, OEF and CMRO₂ by Simultaneous PET/MRI. In: *Proc. Intl. Soc. Mag. Reson. Med.* 29. 2021.
167. Hillman EMC. Coupling mechanism and significance of the BOLD signal: A status report. *Annu Rev Neurosci* 2014; 37: 161–181.
168. Hoge RD, Atkinson J, Gill B, et al. Investigation of BOLD signal dependence on cerebral blood flow and oxygen consumption: The deoxyhemoglobin dilution model. *Magn Reson Med* 1999; 42: 849–863.
169. Yablonskiy DA, Haacke EM. Theory of NMR signal behavior in magnetically inhomogeneous tissues: The static dephasing regime. *Magn Reson Med* 1994; 32: 749–763.
170. He X, Yablonskiy DA. Quantitative BOLD: Mapping of human cerebral deoxygenated blood volume and oxygen extraction fraction: Default state. *Magn Reson Med* 2007; 57: 115–126.
171. Christen T, Lemasson B, Pannetier N, et al. Evaluation of a quantitative blood oxygenation level-dependent (qBOLD) approach to map local blood oxygen saturation. *NMR Biomed* 2010; n/a-n/a.
172. An H, Lin W. Quantitative Measurements of Cerebral Blood Oxygen Saturation Using Magnetic Resonance Imaging. *J Cereb Blood Flow Metab* 2000; 20: 1225–1236.
173. Stone AJ, Blockley NP. A streamlined acquisition for mapping baseline brain oxygenation using quantitative BOLD. *Neuroimage* 2017; 147: 79–88.
174. Cho J, Lee J, An H, et al. Cerebral oxygen extraction fraction (OEF): Comparison of challenge-free gradient echo QSM+qBOLD (QQ) with ¹⁵O PET in healthy adults. *J Cereb Blood Flow Metab*. Epub ahead of print 2020. DOI: 10.1177/0271678X20973951.
175. Lee H, Englund EK, Wehrli FW. Interleaved quantitative BOLD: Combining extravascular R₂' - and intravascular R₂-measurements for estimation of deoxygenated blood volume and hemoglobin oxygen saturation. *Neuroimage* 2018; 174: 420–431.
176. Cho J, Zhang S, Kee Y, et al. Cluster analysis of time evolution (CAT) for quantitative susceptibility mapping (QSM) and quantitative blood oxygen level-dependent magnitude (qBOLD)-based oxygen extraction fraction (OEF) and cerebral metabolic rate of oxygen (CMRO₂) mapping. *Magn Reson Med* 2020; 83: 844–857.
177. Hoge RD. Calibrated fMRI. *Neuroimage* 2012; 62: 930–937.
178. Kastrup A, Krüger G, Neumann-Haefelin T, et al. Changes of cerebral blood flow, oxygenation, and oxidative metabolism during graded motor activation. *Neuroimage* 2002; 15: 74–82.

179. Chiarelli PA, Bulte DP, Wise R, et al. A calibration method for quantitative BOLD fMRI based on hyperoxia. *Neuroimage* 2007; 37: 808–820.
180. Germuska M, Wise RG. Calibrated fMRI for mapping absolute CMRO₂: Practicalities and prospects. *Neuroimage* 2019; 187: 145–153.
181. Blockley NP, Griffeth VEM, Simon AB, et al. A review of calibrated blood oxygenation level-dependent (BOLD) methods for the measurement of task-induced changes in brain oxygen metabolism. *NMR Biomed* 2013; 26: 987–1003.
182. Wise RG, Harris AD, Stone AJ, et al. Measurement of OEF and absolute CMRO₂: MRI-based methods using interleaved and combined hypercapnia and hyperoxia. *Neuroimage* 2013; 83: 135–147.
183. Germuska M, Bulte DP. MRI measurement of oxygen extraction fraction, mean vessel size and cerebral blood volume using serial hyperoxia and hypercapnia. *Neuroimage* 2014; 92: 132–142.
184. Gauthier CJ, Hoge RD. Magnetic resonance imaging of resting OEF and CMRO₂ using a generalized calibration model for hypercapnia and hyperoxia. *Neuroimage* 2012; 60: 1212–1225.
185. Bulte DP, Kelly M, Germuska M, et al. Quantitative measurement of cerebral physiology using respiratory-calibrated MRI. *Neuroimage* 2012; 60: 582–591.
186. Englund EK, Fernández-Seara MA, Rodríguez-Soto AE, et al. Calibrated fMRI for dynamic mapping of CMRO₂ responses using MR-based measurements of whole-brain venous oxygen saturation. *J Cereb Blood Flow Metab* 2020; 40: 1501–1516.
187. Vandenberghe S, Marsden PK. PET-MRI: a review of challenges and solutions in the development of integrated multimodality imaging. *Phys Med Biol* 2015; 60: R115–R154.
188. Werner MK, Schmidt H, Schwenzer NF. MR/PET: A new challenge in hybrid imaging. *Am J Roentgenol* 2012; 199: 272–277.
189. Jadvar H, Colletti PM. Competitive advantage of PET/MRI. *Eur J Radiol* 2014; 83: 84–94.
190. Lorking N, Murray AD, O’Brien JT. The use of positron emission tomography/magnetic resonance imaging in dementia: A literature review. *Int J Geriatr Psychiatry* 2021; 36: 1501–1513.
191. Chen Z, Jamadar SD, Li S, et al. From simultaneous to synergistic MR-PET brain imaging: A review of hybrid MR-PET imaging methodologies. *Hum Brain Mapp* 2018; 39: 5126–5144.
192. Catana C, Drzezga A, Heiss W-D, et al. PET/MRI for Neurologic Applications. *J Nucl Med* 2012; 53: 1916–1925.
193. Ruitenbergh A, den Heijer T, Bakker SLM, et al. Cerebral hypoperfusion and clinical onset of dementia: The Rotterdam study. *Ann Neurol* 2005; 57: 789–794.
194. Daulatzai MA. Cerebral hypoperfusion and glucose hypometabolism: Key pathophysiological modulators promote neurodegeneration, cognitive impairment, and Alzheimer’s disease. *J Neurosci Res* 2017; 95: 943–972.

195. Vercllytte S, Lopes R, Lenfant P, et al. Cerebral Hypoperfusion and Hypometabolism Detected by Arterial Spin Labeling MRI and FDG-PET in Early-Onset Alzheimer's Disease. *J Neuroimaging* 2016; 26: 207–212.
196. Hua J, Liu P, Kim T, et al. MRI techniques to measure arterial and venous cerebral blood volume. *Neuroimage* 2019; 187: 17–31.
197. Iguchi S, Hori Y, Moriguchi T, et al. Verification of a semi-automated MRI-guided technique for non-invasive determination of the arterial input function in ^{15}O -labeled gaseous PET. *Nucl Instruments Methods Phys Res Sect A Accel Spectrometers, Detect Assoc Equip* 2013; 702: 111–113.
198. Zanotti-Fregonara P, Chen K, Liow JS, et al. Image-derived input function for brain PET studies: Many challenges and few opportunities. *J Cereb Blood Flow Metab* 2011; 31: 1986–1998.
199. Narciso L, Ssali T, Wehrli F, et al. Theory and initial validation of a non-invasive hybrid [^{15}O]O₂-PET/MRI approach to obtain image-derived input functions. *J Nucl Med* 2021; 62: 1602 LP – 1602.
200. Subramanyam R, Alpert NM, Hoop B, et al. A model for regional cerebral oxygen distribution during continuous inhalation of $^{15}\text{O}_2$, C ^{15}O , and C $^{15}\text{O}_2$. *J Nucl Med* 1978; 19: 48–53.
201. Frackowiak RS, Lenzi GL, Jones T, et al. Quantitative measurement of regional cerebral blood flow and oxygen metabolism in man using ^{15}O and positron emission tomography: theory, procedure, and normal values. *J Comput Assist Tomogr* 1980; 4: 727–36.
202. Hattori N, Bergsneider M, Wu H, et al. Accuracy of a method using short inhalation of (^{15}O)-O₂ for measuring cerebral oxygen extraction fraction with PET in healthy humans. *J Nucl Med* 2004; 45: 765–70.
203. Yablonskiy DA, Sukstanskii AL, He X. Blood oxygenation level-dependent (BOLD)-based techniques for the quantification of brain hemodynamic and metabolic properties - theoretical models and experimental approaches. *NMR Biomed* 2013; 26: 963–986.
204. An H, Lin W, Celik A, et al. Quantitative measurements of cerebral metabolic rate of oxygen utilization using MRI: a volunteer study. *NMR Biomed* 2001; 14: 441–447.
205. Gauthier CJ, Hoge RD. A generalized procedure for calibrated MRI incorporating hyperoxia and hypercapnia. *Hum Brain Mapp* 2013; 34: 1053–1069.
206. Merola A, Germuska MA, Murphy K, et al. Assessing the repeatability of absolute CMRO₂, OEF and haemodynamic measurements from calibrated fMRI. *Neuroimage* 2018; 173: 113–126.
207. Ibaraki M, Shimosegawa E, Miura S, et al. PET measurements of CBF, OEF, and CMRO₂ without arterial sampling in hyperacute ischemic stroke: Method and error analysis. *Ann Nucl Med* 2004; 18: 35–44.
208. Jiang TT, Videen TO, Grubb RL, et al. Cerebellum as the Normal Reference for the Detection of Increased Cerebral Oxygen Extraction. *J Cereb Blood Flow Metab* 2010; 30: 1767–1776.

209. Ito H, Ibaraki M, Kanno I, et al. Changes in the arterial fraction of human cerebral blood volume during hypercapnia and hypocapnia measured by positron emission tomography. *J Cereb Blood Flow Metab* 2005; 25: 852–857.
210. Buxton RB, Uludağ K, Dubowitz DJ, et al. Modeling the hemodynamic response to brain activation. *Neuroimage* 2004; 23: S220–S233.
211. Cooper JA, Tichauer KM, Boulton M, et al. Continuous monitoring of absolute cerebral blood flow by near-infrared spectroscopy during global and focal temporary vessel occlusion. *J Appl Physiol* 2011; 110: 1691–1698.
212. Sakoh M, Østergaard L, Røhl L, et al. Relationship between residual cerebral blood flow and oxygen metabolism as predictive of ischemic tissue viability: sequential multitracer positron emission tomography scanning of middle cerebral artery occlusion during the critical first 6 hours after st. *J Neurosurg* 2000; 93: 647–657.
213. Logan J, Fowler JS, Volkow ND, et al. A strategy for removing the bias in the graphical analysis method. *J Cereb Blood Flow Metab* 2001; 21: 307–320.
214. Varga J, Szabo Z. Modified regression model for the Logan plot. *J Cereb Blood Flow Metab* 2002; 22: 240–244.
215. Kudomi N, Eunjoo Choi, Yamamoto S, et al. Development of a GSO detector assembly for a continuous blood sampling system. *IEEE Trans Nucl Sci* 2003; 50: 70–73.
216. Aanerud J, Borghammer P, Mallar Chakravarty M, et al. Brain energy metabolism and blood flow differences in healthy aging. *J Cereb Blood Flow Metab* 2012; 32: 1177–1187.
217. Pappata S, Fiorelli M, Rommel T, et al. PET study of changes in local brain hemodynamics and oxygen metabolism after unilateral middle cerebral artery occlusion in baboons. *J Cereb Blood Flow Metab* 1993; 13: 416–424.
218. Martin WRW, Powers WJ, Raichle ME. Cerebral Blood Volume Measured with Inhaled C 15 O and Positron Emission Tomography. *J Cereb Blood Flow Metab* 1987; 7: 421–426.
219. Cockburn N, Corsaut J, Kovacs MS, et al. Validation protocol for current good manufacturing practices production of [15O]water for hybrid PET/MR studies. *Nucl Med Commun* 2020; 41: 1100–1105.
220. Iguchi S, Moriguchi T, Yamazaki M, et al. System evaluation of automated production and inhalation of 15O-labeled gaseous radiopharmaceuticals for the rapid 15O-oxygen PET examinations. *EJNMMI Phys* 2018; 5: 1–21.
221. Hori Y, Hirano Y, Koshino K, et al. Validity of using a 3-dimensional PET scanner during inhalation of 15 O-labeled oxygen for quantitative assessment of regional metabolic rate of oxygen in man. *Phys Med Biol* 2014; 59: 5593–5609.
222. Günther M, Oshio K, Feinberg DA. Single-shot 3D imaging techniques improve arterial spin labeling perfusion measurements. *Magn Reson Med* 2005; 54: 491–498.
223. Vafae MS, Vang K, Bergersen LH, et al. Oxygen consumption and blood flow coupling in human motor cortex during intense finger tapping: Implication for a role of lactate. *J Cereb Blood Flow Metab* 2012; 32: 1859–1868.

224. Oshima T, Karasawa F, Satoh T. Effects of propofol on cerebral blood flow and the metabolic rate of oxygen in humans. *Acta Anaesthesiol Scand* 2002; 46: 831–835.
225. Andersen JB, Henning WS, Lindberg U, et al. Positron emission tomography/magnetic resonance hybrid scanner imaging of cerebral blood flow using ¹⁵O-water positron emission tomography and arterial spin labeling magnetic resonance imaging in newborn piglets. *J Cereb Blood Flow Metab* 2015; 35: 1703–1710.
226. Olsen AK, Keiding S, Munk OL. Effect of hypercapnia on cerebral blood flow and blood volume in pigs studied by positron emission tomography. *Comp Med* 2006; 56: 416–420.
227. Heurling K, Leuzy A, Jonasson M, et al. Quantitative positron emission tomography in brain research. *Brain Res* 2017; 1670: 220–234.
228. Grubb RL, Phelps ME, Ter-Pogossian MM. Regional cerebral blood volume in humans. *Arch Neurol* 1973; 28: 38.
229. Narciso L, Ssali T, Liu L, et al. A Noninvasive Method for Quantifying Cerebral Metabolic Rate of Oxygen by Hybrid PET/MRI: Validation in a Porcine Model. *J Nucl Med* 2021; jnumed.120.260521.
230. Ssali T, Narciso L, Hicks J, et al. Concordance of Regional Hypoperfusion by ASL MRI and ¹⁵O-water PET in Frontotemporal Dementia: Is ASL an Efficacious Alternative? In: *Proc. Intl. Soc. Mag. Reson. Med.* 29. 2021.
231. Herscovitch P, Raichle ME, Kilbourn MR, et al. Positron emission tomographic measurement of cerebral blood flow and permeability-surface area product of water using [¹⁵O]water and [¹¹C]butanol. *J Cereb Blood Flow Metab* 1987; 7: 527–542.
232. Yan L, Li C, Kilroy E, et al. Quantification of arterial cerebral blood volume using multiphase-balanced SSFP-based ASL. *Magn Reson Med* 2012; 68: 130–139.
233. Chen JJ, Pike GB. MRI measurement of the BOLD-specific flow–volume relationship during hypercapnia and hypocapnia in humans. *Neuroimage* 2010; 53: 383–391.
234. Simon AB, Buxton RB. Understanding the dynamic relationship between cerebral blood flow and the BOLD signal: Implications for quantitative functional MRI. *Neuroimage* 2015; 116: 158–167.
235. Ciris PA, Qiu M, Constable RT. Noninvasive MRI measurement of the absolute cerebral blood volume–cerebral blood flow relationship during visual stimulation in healthy humans. *Magn Reson Med* 2014; 72: 864–875.
236. Blazey T, Snyder AZ, Goyal MS, et al. A systematic meta-analysis of oxygen-to-glucose and oxygen-to-carbohydrate ratios in the resting human brain. *PLoS One* 2018; 13: e0204242.
237. Warburg O, Wind F, Negelein E. The metabolism of tumors in the body. *J Gen Physiol* 1927; 8: 519–530.
238. Shannon BJ, Vaishnavi SN, Vlassenko AG, et al. Brain aerobic glycolysis and motor adaptation learning. *Proc Natl Acad Sci* 2016; 113: E3782–E3791.
239. Blazey T, Snyder AZ, Su Y, et al. Quantitative positron emission tomography reveals

- regional differences in aerobic glycolysis within the human brain. *J Cereb Blood Flow Metab* 2019; 39: 2096–2102.
240. Narciso L, Taha A, Dassanayake P, et al. Development of a non-invasive PET/MRI method for quantifying cerebral glucose kinetics. In: *XIII International Symposium of Functional Neuroreceptor Mapping of the Living Brain*. 2021.
241. Patlak CS, Blasberg RG, Fenstermacher JD. Graphical Evaluation of Blood-to-Brain Transfer Constants from Multiple-Time Uptake Data. *J Cereb Blood Flow Metab* 1983; 3: 1–7.
242. Castellaro M, Rizzo G, Tonietto M, et al. A Variational Bayesian inference method for parametric imaging of PET data. *Neuroimage* 2017; 150: 136–149.

Appendices

Appendix A: Copyright Agreement Information

Assignment of Copyright

The Journal of Nuclear Medicine (JNM) is pleased to publish your article:

Manuscript Title: Validation of a non-invasive hybrid PET/MR method for imaging the cerebral metabolic rate of oxygen

MS Number: JNUMED/2020/260521 Date: 2020-11-17

Section A—to be completed by non-U.S. government employees. (If the article has multiple authors, each author must individually transfer his or her copyright in the work by signing this section. If the article is not published in *JNM*, the following copyright transfer agreement will not take effect.)

Upon acceptance of the article named above by *JNM*, all copyright ownership is transferred to the Society of Nuclear Medicine and Molecular Imaging. We, the undersigned coauthors of this article, have contributed to (1) data design, analysis, or interpretation; (2) writing or critiquing drafts of the manuscript; and (3) approval of the final manuscript before publication. We share in the responsibility for the release of any part or all of the material contained within the manuscript. We also affirm that the manuscript has been seen and approved by all authors. The undersigned warrant that the manuscript (or its essential substance) is **new and original**; has not been published other than as an abstract in any language or format; and has not been submitted elsewhere for print or electronic publication consideration.

We warrant that the manuscript does not contain any material the publication of which would violate any copyright or other personal or proprietary right of any person or entity. We will obtain and include with the manuscript written permission from any respective copyright owners for the use of any textual, illustrative, or tabular materials that have been previously published or are otherwise copyrighted and owned by third parties. We agree that it is our responsibility to pay any fees charged for permissions.

We also warrant that **any** human and/or animal studies undertaken as part of the research from which this manuscript was derived are in compliance with regulations of our institution(s) and with generally accepted guidelines governing such work.

We further warrant that we have herein disclosed any and all financial or other relationships that could be construed as a conflict of interest and that all sources of financial support for the study have indicated in the disclosure.

1. Copyright transfer: The authors hereby transfer all copyrights in and to the manuscript titled above in all forms and media, now or hereafter known, to the Society of Nuclear Medicine and Molecular Imaging effective if and when the article is accepted for publication in *JNM*.

2. Permission to reprint: The authors retain the following nonexclusive copyrights, to be exercised only after the article has been published in final format in the print version of *JNM*.

- (a) Reprint the article in print collections of the author's own writing.
- (b) Present the article orally in its entirety.
- (c) Use the article in theses and/or dissertations.
- (d) Reproduce the article for use in courses the author is teaching. (If the author is employed by an academic institution, that institution may also reproduce the article for course teaching.)
- (e) Distribute photocopies of the article to colleagues, but only for noncommercial purposes.
- (f) Reuse original figures and tables in future works created by the author.
- (g) Post a copy of the article on the author's personal website, departmental website, and/or the university's intranet, provided a hyperlink to the article on the *JNM* website is included.
- (h) In all the instances under clauses 2a through 2g above, the author will give proper credit to the original publication in *JNM* as follows:

This research was originally published in *JNM*. Author(s). Title. *JNM*. Year;vol:pp–pp. © by the Society of Nuclear Medicine and Molecular Imaging, Inc.

3. Publish Ahead of Print policy: The authors understand that if and when the manuscript is accepted for publication in *JNM*, it will be prepublished online as a Publish Ahead of Print paper. The authors acknowledge that *JNM*'s Publish Ahead of Print papers undergo full peer review.

Curriculum vitae

Lucas D. L. Narciso

POST-SECONDARY EDUCATION

Western University

Schulich School of Medicine & Dentistry	<u>Doctorate Degree</u>
Department of Medical Biophysics	Supervised by Keith St Lawrence, PhD
London, ON, Canada	2018/01 (current)

PUCRS

Electrical Engineering Graduate Program	<u>Master's Degree</u>
Porto Alegre, RS, Brazil	Supervised by Ana M. Marques da Silva, PhD
	2014/08 to 2016/08

PUCRS

Department of Physics	<u>Bachelor's Degree in Medical Physics</u>
Porto Alegre, RS, Brazil	<u>Teaching Degree in Physics</u>
	2008/03 to 2014/08

University of Guelph

Department of Biological and Medical Physics	Exchange, Science without Borders program
Guelph, ON, Canada	2013/01 to 2013/12

RECOGNITIONS

Doctorate Abroad Scholarship

Ministry of Education, Brazil	CAD \$117,000.00 (Declined)
	2018/09 to 2022/08

Master's Degree Scholarship

Ministry of Education, Brazil	BRL R\$45,400.00
	2014/08 to 2016/07

Academic distinction

PUCRS, Brazil	2014/08
---------------	---------

Science without Borders Exchange Scholarship

Ministry of Education, Brazil	CAD \$33,000.00
	2013/01 to 2013/12

Undergraduate Tuition Scholarship (ProUni)

Ministry of Education, Brazil	BRL R\$87,000.00
	2008/03 to 2014/07

Undergraduate Research Scholarships

PUCRS and FAPERGS	BRL R\$5,100.00
BPA	2010/04 to 2010/12
PROBIC	2014/02 to 2014/07

RELEVANT WORK EXPERIENCE

Martini Science

Nuclear Medicine Department	Medical Physicist 2014/10 to 2017/12
-----------------------------	---

Department of Physics

PUCRS	Medical Images Processing Fall 2015 – Full GTA
-------	---

Western University

Department of Applied Mathematics	Applied Mathematics for Engineers I Fall 2018 - Half GTA Winter 2019 – Full GTA
-----------------------------------	---

Western University

Department of Applied Mathematics	Calculus 1000 Fall 2020 – Half GTA
-----------------------------------	---------------------------------------

Western University

Department of Applied Mathematics	Calculus 1301 Winter 2020 – Full GTA
-----------------------------------	---

Western University

Department of Medical Biophysics	Mathematical Transform Applications in Medical Biophysics Fall 2019, Fall 2020, and Fall 2021 Quarter GTA
----------------------------------	---

RELEVANT PUBLICATIONS

Journal Articles

- Lucas Narciso, Tracy Ssali, Linshan Liu, Heather Biernaski, John Butler, Laura Morrison, Jennifer Hadway, Jeffrey Corsaut, Justin W Hicks, Michael C Langham, Felix W Wehrli, Hidehiro Iida and Keith St. Lawrence. **A Noninvasive Method for Quantifying Cerebral Metabolic Rate of Oxygen by Hybrid PET/MRI: Validation in a Porcine Model.** *J Nucl Med* 2021; jnumed.120.260521.
- Lucas Narciso, Tracy Ssali, Hidehiro Iida and Keith St Lawrence. **A non-invasive reference-based method for imaging the cerebral metabolic rate of oxygen by PET/MR: theory and error analysis.** *Phys Med Biol* 2021; 66: 065009.

- Tracy Ssali, Udunna C Anazodo, Lucas Narciso, Linshan Liu, Sarah Jesso, Lauryn Richardson, Matthias Günther, Simon Konstandin, Klaus Eickel, Frank Prato, Elizabeth Finger, Keith St Lawrence. **Sensitivity of Arterial Spin Labeling for Characterization of Longitudinal Perfusion Changes in Frontotemporal Dementia and Related Disorders.** *NeuroImage Clin.* 2021; 102853.
- Samara O Pinto, Paulo R R V Caribe, Lucas Narciso, Ana Maria Marques da Silva. **Optimization of reconstruction parameters in [¹⁸F]FDG PET brain images aiming scan time reduction.** *Revista Brasileira de Física Médica* 2021; 15: 611.
- Lucas Narciso, Phelipi Schuck, Caroline Dartora, Cristina Matushita, Jefferson Becker, Ana Maria Marques da Silva. **Semiquantification study of [¹¹C]-(R)-PK11195 PET brain images in multiple sclerosis.** *Revista Brasileira de Física Médica* 2016; 10: 39-43.

Conference Publications

- Lucas Narciso, Tracy Ssali, Linshan Liu, Sarah Jesso, Justin W Hicks, Udunna Anazodo, Elizabeth Finger, Keith St Lawrence. **Quantification of cerebral blood flow by a non-invasive hybrid PET/MR method for extracting the ¹⁵O-water image-derived input function free of partial volume errors.** In: *Neuroreceptor Mapping.* 2021.
- Lucas Narciso, Alaa Taha, Praveen Dassanayake, Tommaso Volpi, Linshan Liu, Andrea Soddu, Udunna Anazodo, Alessandra Bertoldo, Keith St Lawrence. **Development of a non-invasive PET/MRI method for quantifying cerebral glucose kinetics.** In: *Neuroreceptor Mapping.* 2021.
- Samara Pinto, Paulo R R V Caribe, Cristina S Matushita, Diego B Pianta, Lucas Narciso, Ana Maria Marques da Silva. **Initial validation of reconstruction parameters in [¹⁸F]FDG PET brain images aiming scan time reduction.** In: *Neuroreceptor Mapping.* 2021.
- Lucas Narciso, Tracy Ssali, Felix Wehrli, Keith St Lawrence. **Theory and initial validation of a noninvasive hybrid [¹⁵O]O₂-PET/MRI approach to obtain image-derived input functions.** In: *2021 SNMMI Annual Meeting.* 2021.
- Lucas Narciso, Tracy Ssali, Linshan Liu, Heather Biernaski, John Butler, Laura Morrison, Jennifer Hadway, Jeffrey Corsaut, Justin W. Hicks, Michael C. Langham, Felix W. Wehrli, Hidehiro Iida, Keith St Lawrence. **A non-invasive hybrid PET/MR method for imaging the cerebral metabolic rate of oxygen.** In: *2021 SNMMI Annual Meeting.* 2021.
- Lucas Narciso, Tracy Ssali, Linshan Liu, Heather Biernaski, John Butler, Laura Morrison, Jennifer Hadway, Jeffrey Corsaut, Justin W. Hicks, Michael C. Langham, Felix W. Wehrli, Hidehiro Iida, Keith St Lawrence. **Validation of OxFlow**

Measurements of Whole-Brain CBF, OEF and CMRO₂ by Simultaneous PET/MRI. In: *2021 ISMRM & SMRT Annual Meeting & Exhibition*, 2021.

- Tracy Ssali, Lucas Narciso, Justin W Hicks, Matthais Günther, Frank Prato, Udunna Anazodo, Elizabeth Finger, Keith St Lawrence. **Concordance of Regional Hypoperfusion by ASL MRI and 15O-water PET in Frontotemporal Dementia: Is ASL an Efficacious Alternative?** In: *2021 ISMRM & SMRT Annual Meeting & Exhibition*. 2021.
- Tracy Ssali, Lucas Narciso, Matthais Günther, Frank Prato, Udunna Anazodo, Elizabeth Finger, Keith St Lawrence. **Feasibility of Arterial Spin Labeling for Detection of Longitudinal Changes in Perfusion in Elderly and Frontotemporal Dementia Patients.** In: *2021 ISMRM & SMRT Annual Meeting & Exhibition*, 2021.
- Lucas Narciso, Tracy Ssali, Linshan Liu, Heather Biernaski, John Butler, Laura Morrison, Jennifer Hadway, Jeffrey Corsaut, Justin W. Hicks, Michael C. Langham, Felix W. Wehrli, Hidehiro Iida, Keith St Lawrence. **PMROx: non-invasive PET/MR imaging of the cerebral oxidative metabolism.** In: *London Health Research Day*. 2021.
- Lucas Narciso, Tracy Ssali, Linshan Liu, Heather Biernaski, John Butler, Laura Morrison, Jennifer Hadway, Jeffrey Corsaut, Justin W. Hicks, Michael C. Langham, Felix W. Wehrli, Hidehiro Iida, Keith St Lawrence. **Validation of OxFlow Measurements of Whole-Brain CBF, OEF and CMRO₂ by Simultaneous PET/MRI.** In: *2021 ISMRM & SMRT Annual Meeting & Exhibition*, 2021.
- Lucas Narciso, Tracy Ssali, Linshan Liu, Heather Biernaski, John Butler, Laura Morrison, Justin W. Hicks, Michael C. Langham, Felix W. Wehrli, Hidehiro Iida, Keith St Lawrence. **Validation of a non-invasive hybrid PET/MRI method to image the cerebral metabolic rate of oxygen.** In: *Neuroreceptor Mapping*. 2020 (cancelled due to COVID-19).
- Lucas Narciso, Tracy Ssali, Linshan Liu, Laura Morrison, Heather Biernaski, John Butler, Udunna Anazodo, Justin W. Hicks, Felix W. Wehrli, Hidehiro Iida, Keith St Lawrence. **A non-invasive hybrid PET/MRI method for imaging CMRO₂.** In: *SNMMI/ISMRM PET/MRI Meeting*. 2019.
- Tracy Ssali, Lucas Narciso, Justin W. Hicks, Udunna Anazodo, Elizabeth Finger, Michael Kovacs, Matthias Günther, Frank Prato, Keith St Lawrence. **A non-invasive hybrid PET/MR approach to quantify CBF: translating to clinical studies.** In: *JCBFM: Brain PET*. 2019.
- Lucas Narciso, Tracy Ssali, Udunna Anazodo, Hidehiro Iida, Keith St Lawrence. **Initial assessment of a reference-based noninvasive hybrid PET/MRI method for imaging CMRO₂.** In: *JCBFM: Brain PET*. 2019.

- Lucas Narciso, Tracy Ssali, Udunna Anazodo, Keith St Lawrence. **Reference-based non-invasive hybrid PET/MRI method for CMRO₂ imaging: error analysis and initial assessment**. In: *London Health Research Day*. 2019.
- Lucas Narciso, Tracy Ssali, Udunna Anazodo, Hidehiro Iida, Keith St Lawrence. **Error analysis of a non-invasive hybrid PET/MRI method for imaging CMRO₂**. In: *Proceedings of the 17th Annual Imaging Network Ontario Symposium*. 2019.
- Tracy Ssali, Lucas Narciso, Justin W. Hicks, Udunna Anazodo, Elizabeth Finger, Frank Prato, Keith St Lawrence. **Optimization of phase contrast for CBF quantification by the non-invasive hybrid PET/MR approach**. In: *Proceedings of the 17th Annual Imaging Network Ontario Symposium*. 2019.
- Tracy Ssali, Lucas Narciso, Justin W. Hicks, Udunna Anazodo, Elizabeth Finger, Michael Kovacs, Matthias Günther, Frank Prato, Keith St Lawrence. **A non-invasive hybrid PET/MR approach for validation of ASL in clinical studies**. In: *University of Michigan International Workshop on Arterial Spin Labeling MRI: Technical Updates and Clinical Experience*. 2019.